Design and Test of a Low Noise Amplifier for the Auger Radio Detector

von

Eugène Antoine Maurice Stephan

Diplomarbeit in Physik

vorgelegt der

Fakultät für Mathematik, Informatik und Naturwissenschaften
der
Rheinisch Westfälischen Technischen Hochschule Aachen

im Juli 2009

angefertigt am

III. Physikalischen Institut A

Erstgutachter und Betreuer

Prof. Dr. Thomas Hebbeker
III. Physikalisches Institut A
RWTH Aachen

Zweitgutachter

Prof. Dr. Martin Erdmann
III. Physikalisches Institut A
RWTH Aachen

Contents

List of Figures

1. Introduction

The sky has always been a subject of mankind's interest and studies. Nothing else seems to evoke more fundamental questions just by observing it - philosophical questions as well as those of natural sciences. With technical evolution new scientific methods of observing the space around us always led to deeper understanding of the universe and our place within it.

The cosmos donates us permanently with information about its nature. For a long time we were only able to detect this information in the region of visible light. With time new windows to the cosmos were opened, broadening the spectrum of electromagnetic radiation which we were able to examine.

Combining aspects of high energy particle physics, astrophysics and cosmology a relatively new field of research has unlocked a new window: astroparticle physics goes for the information contained within particles reaching the Earth from far distant and also relatively close astronomical objects. Interest in astroparticle physics has grown during the last decades and the trend seems to continue.

One of the main topics of astroparticle physics are cosmic rays of the highest energies: a single particle carrying the energy of a well-slammed tennis ball. With energies from 10^{18} eV to several 10^{20} eV laboratory based accelerator physics seems to be far away to produce such high energy particles. But these ultra high energy cosmic rays are very rare. On average only one with an energy of about $10^{18.5}$ eV reaches an area of a square kilometer per year. Until now only little about ultra high energy cosmic rays is known. Where do they come from? How can they reach such high energies? How do they propagate through space? And what are they?

The Pierre Auger Observatory is the largest experiment to examine these questions. On an area of 3,000 km^2 - Rhode Island for example has a size of 4,000 km^2, the German state Saarland a size of 2,600 km^2 - the observatory successfully operates a hybrid detector consisting of a Surface Detector and a Fluorescence Detector. This southern site is located in the Argentinian province of Mendoza. Additionally the northern site stretching about 20,000 km^2 is currently in the phase of planning and will be built in Colorado, U.S.A. to investigate also the sky of the northern hemisphere.

Besides the two established methods of detecting ultra high energy cosmic rays used at the Pierre Auger Observatory its international collaboration studies the use

of a new Radio Detector system. When the cosmic rays enter Earth's atmosphere they produce a shower of secondary particles which then emit radiation in the radio band. This radiation can be detected by adequate antennas and receivers. Several test setups have been operated during the last years and at the moment the collaboration is busy to set up the Auger Engineering Radio Array (AERA) instrumenting an area of 20 km^2.

Since the radio signals of the air showers are low compared to the background noise, which is caused by our galaxy and man-made transmitters, a reliable low-noise preamplifier is essential for the success of the experimental setup. Without such an amplifier further electronics would have no chance to distinguish between the signal of physical interest and the background noise.
In this work the design and tests of an appropriate low-noise preamplifier will be presented and discussed.

The following section 2 will give a short introduction to the physics of ultra-high-energy cosmic rays. In Section 3 the development of air showers and the methods of detecting these air showers will be discussed. In this context one focus will also be on radio signals emitted by the secondary particles. A brief description of the Pierre Auger Observatory and its different detectors will be given in section 4. The principles of high frequency preamplifier theory will be discussed in section 5. Section 6 will introduce the design of the low-noise preamplifier and in section 7 the test routines and results will be given and discussed. In section 8 the results will be summarized and an outlook towards further investigations will be made.

2. Physics of Ultra High Energy Cosmic Rays

At the end of the 19^{th} century scientists were troubled by the fact that an electrically charged body would lose its charge with time no matter how good it was isolated from the ground. The only possible solution seemed to be that the body gives its charge to the surrounding air but unluckily it was known as an isolator.
After A. H. Becquerel's discovery of radioactivity in 1896 a solution was found: the air gets ionized by radioactive radiation and the emerging ions discharge the charged body. The conductivity of the air became a topic for many experimenters and with the awareness of radioactive isotopes in the upper Earth's crust it was believed that the conductivity should decrease with increasing height.
But in 1912 V. F. Hess measured quite the opposite [1]. During his famous balloon flights he found an increase of conductivity with higher altitude. He concluded correctly that a large amount of ionizing radiation must come from above the atmosphere. This was the discovery of *cosmic rays* for which Hess earned the noble prize some years later.
By *cosmic rays* charged stable particles are meant hitting the Earth's atmosphere. Not meant are those low energy particles up to 1 keV originating from the sun. To make a difference these particles are referred to as *solar wind*. Therefore cosmic rays arrive the Earth per definition from outside our solar system.
The cosmic radiation is composed of about 87 % protons, 12 % α-particles, 1 % havier nuclei and a small amount of electrons. The distribution of elements in cosmic rays is comparable to the one from the sun (see figure 2.1), yet there are some differences which can be explained by spallation which occurs when particles traverse through galactic matter.
Even though cosmic rays have been known for a long time interest in them is still growing rapidly, not least because of the fact that detection techniques become more and more sophisticated with time. But still little is known of cosmic rays at the highest energies. Their origins seem to be one of the key questions of today's astrophysics and scientists hope to find evidence for their acceleration- and their propagation-models soon.

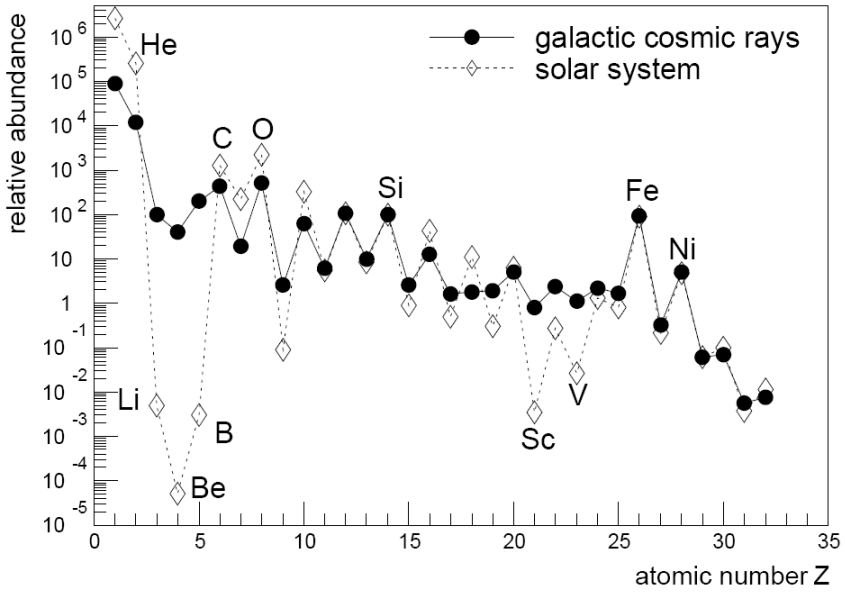

Figure 2.1: The composition of galactic cosmic rays compared the the composition in our solar system. The abundances are normalized to 100 for Si. Taken from [2].

2.1 Energy Spectrum

Figure 2.2 shows the differential flux of the cosmic rays versus their energy. This is called the *energy spectrum*. It covers about 32 orders of magnitude in energy.
For energies below 10 GeV the flux is modulated by solar magnetic fields. For higher energies it follows a power law which is typical for an acceleration spectrum:

$$\frac{d^2\phi(E)}{dEd\Omega} \sim \left(\frac{E}{\mathrm{GeV}}\right)^{-\gamma}, \tag{2.1}$$

wherein $\gamma \approx 2.7$ is the spectral index.
There are two main features in the energy spectrum: the so called *knee* around $10^{15.5}$ eV and the *ankle* around $10^{18.5}$ eV.
At the knee the spectral index changes from 2.7 to 3.1. It is not yet understood by which effect this is caused. Changes in the acceleration mechanism or the composition of the cosmic rays have been discussed ([5], [6]).
At the ankle the spectral index changes back to 2.7 when the origin of cosmic rays change from galactic to extra-galactic. The Larmor-radius R_L of a particle with charge number Z and high Energy E in a magnetic field of strength B is[1]

$$\left(\frac{R_L}{\mathrm{kpc}}\right) \approx 1.1 \frac{1}{Z} \left(\frac{E}{10^9 \mathrm{GeV}}\right) \left(\frac{B}{\mu\mathrm{G}}\right)^{-1}. \tag{2.2}$$

Our galaxy has a magnetic field strength in the order of μG. The Larmor-radius of a proton with an energy of 10^{18} eV allows therefore the particle to escape from

[1]parsec: 1 pc = $3.086 \cdot 10^{16}$ m, Gauss: 1G =10^{-4} T

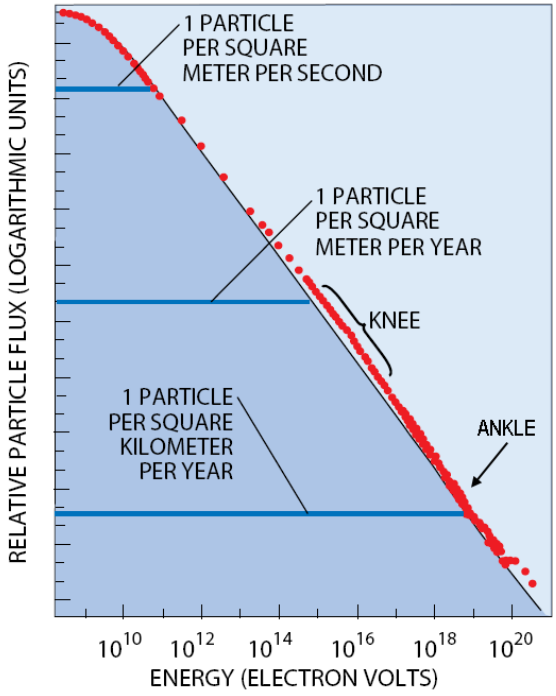

Figure 2.2: Observed energy spectrum of primary cosmic rays. The spectrum follows a power law from 10^{10} eV to 10^{20} eV with slight changes around $10^{15.5}$ eV (knee) and $10^{18.5}$ eV (ankle). The fluxes above the knee and the ankle are approximately 1 per m^2 per year and 1 per km^2 per year. (Modified, original taken from [3]). The absolute flux is shown in figure 2.3.

the galaxy since its size is in the order of kpc. One can conclude that particles with energies below 10^{18} eV arrive us from galactic sources whereas particles with higher energies must be extra-galactic. The change of the flux from a power law with constant spectral index is more obvious if the flux is scaled appropriately. Figure 2.3 shows the energy spectrum with the flux scaled with $E^{2.5}$.
Those cosmic rays with energies higher than 10^{18} eV are called *ultra-high-energy cosmic rays* (UHECRs).
At the knee one measures 1 particle m^{-2} $year^{-1}$. At the ankle the flux is reduced to 1 particle km^{-2} $year^{-1}$. Due to the reduced flux it is quite a challenge to detect a cosmic ray with an energy of 10^{20} eV. No direct measurement could achieve the needed statistics. Instead indirect measurements using large detector areas are needed. They will be discussed in the following chapter 3. The equivalent energy of a LHC proton would be 10^{17} eV (cf. figure 2.3) so that accelerator physics is far away from reaching energies as they appear within cosmic rays. It remains the question how nature accelerates particles to become UHECRs.

2.2 Origin of Cosmic Rays

There are two different approaches to explain how particles can reach ultra-high-energies. The bottom-up approach describes the particles being accelerated in electromagnetic fields, whereas the top-down approach acts on the assumption that

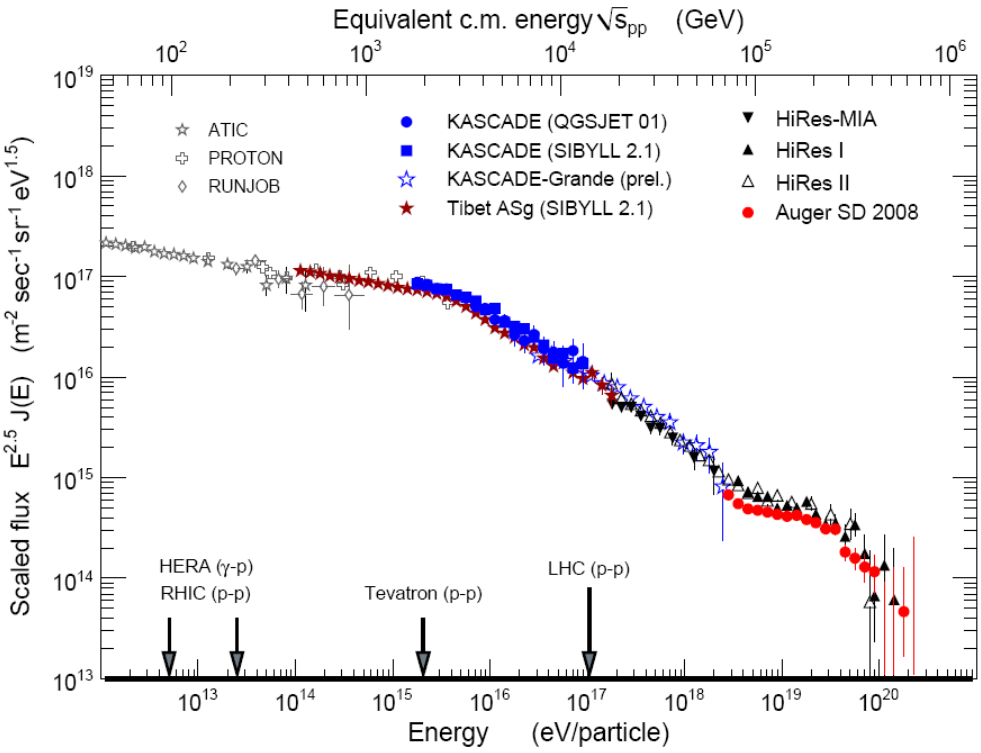

Figure 2.3: Observed energy spectrum of primary cosmic rays measured at different experiments. The integral flux has been scaled with $E^{2.5}$ to make changes of the flux from a power law with constant spectral index more obvious than e.g. in figure 2.2. The data is obtained by direct measurements above the atmosphere (ATIC, PROTON, RUNJOB) as well as from air shower experiments (see chapter 3). Taken from [4]. The upper horizontal axis shows the equivalent center of mass energy to allow comparisons to large collider energies.

UHECRs emerge from the decay of very heavy exotic particles. These particles are believed to be remnants from the big-bang. Since the top-down approach requires new physics beyond the standard model we will focus on the bottom-up scenario.
Huge electric potentials in the universe would be cleared by cosmic plasma, therefore they are excluded as accelerators for UHECRs. Only at the poles of pulsars such electric potentials might occur.
E. Fermi described two acceleration models [7]. One considers turbulent magnetic fields as the place where charged particles gain their ultra-high-energy by statistical acceleration due to multiple scattering with the lines of the magnetic flux. With a certain threshold energy of the particle entering the field, the gain of energy becomes more probable than the loss of energy. Such magnetic fields appear for example in galactic clouds of gas. The other model describes shock waves of plasma expanding into the interstellar medium and the magnetic inhomogenities preceding and following them as accelerators for UHECRs. These shock waves are created by super novae.
To reach a certain energy the particle has to be trapped inside a magnetic field for a certain while. Regarding the Larmor-radius in equation (2.2) we see that the

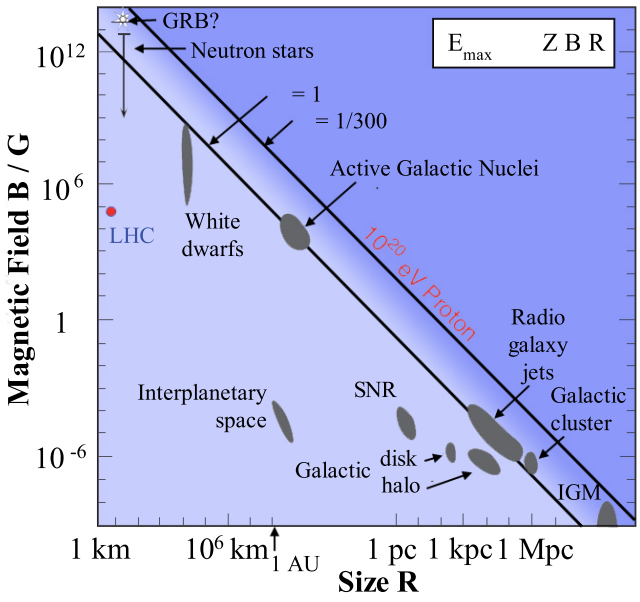

Figure 2.4: The Hillas plot. In the parameter space of magnetic field strength and size various cosmological objects are plotted. A certain value of E_{max} is according to equation (2.3) displayed as a straight line from the upper left to the lower right. Possible sources for particles with E_{max} must lie on or above this line. (Modified, original taken from [4].)

maximal energy is limited and does not grow further if the Larmor-radius reaches the size of the source R_s. We can derive a stronger bound if we take the velocity of the scattering center β into account:

$$\left(\frac{E_{max}}{10^9\text{GeV}}\right) \approx 0.9\beta Z \left(\frac{B}{\mu\text{G}}\right) \left(\frac{R_s}{1\text{kpc}}\right) . \tag{2.3}$$

A. M. Hillas used the relation to plot the magnetic field strength against the size of sources and marked the position of known astronomical objects in the diagram [8]. Figure 2.4 shows the so called Hillas plot. Constant energies appear as lines from the upper left to the lower right. For a certain E_{max} possible sources lie on or above this line. Already for $\beta = 1$ and protons with an energy of 10^{18} eV not many possible sources remain.

2.3 Propagation

While cosmic rays propagate through space they interact with the cosmic microwave background (CMB) and magnetic fields.
The CMB was discovered by A. A. Penzias and R. W. Wilson in 1965 [10]. All

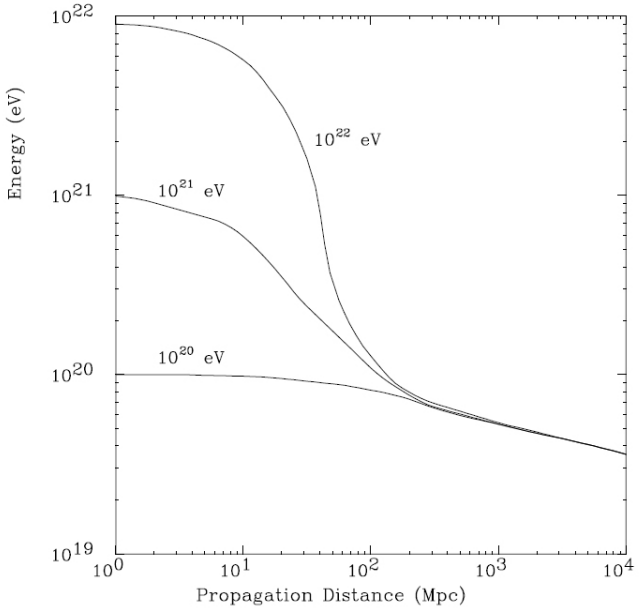

Figure 2.5: Protons of different initial energies lose energy by interacting with the CMB while propagating through space. After about 100 Mpc all protons have the same energy below 10^{20} eV. Taken from [9].

kinds of particles interact with the photons of the 2.7 K microwave background. For protons the decays to nucleons and pions via a Δ^+-resonance are dominant.

$$\begin{aligned} p + \gamma_{CMB} \rightarrow & \Delta^+ \rightarrow n + \pi^+ \\ & \Delta^+ \rightarrow p + \pi^0 \end{aligned} \tag{2.4}$$

If the energy of the proton is sufficient to produce a pion it will partly lose its energy. This means that protons above a certain energy threshold will lose their energy while propagating through the universe until they reach this threshold. An observer therefore has to answer the question with which probability an observed cosmic ray has traveled a certain distance.

Regarding figure 2.5 we see that all protons detected with energies higher than 10^{20} eV must come from sources closer than 100 Mpc. Since the size of the visible universe is about 4.3 Gpc and we are able to detect visible light up to $\sim$ 3.5 Gpc, a source in the distance of 100 Mpc seems relatively close.
The underlying interaction of protons with the CMB was first analyzed by K. Greisen, G. T. Zatsepin and V. A. Kuzmin in 1966 ([11], [12]) and is therefore known as the *GZK-effect*. This should lead to a change in the energy spectrum at the highest energies: the flux should rapidly decrease. This is called the *GZK-cutoff* and predicted for energies of several times 10^{19} eV [13]. It is still a question whether the GZK-cutoff exists or not. Recent results show that the energy spectrum does not follow a power law above an energy of $10^{19.6}$ eV (Yamamoto for the Pierre Auger Collaboration, 2007 [14]).

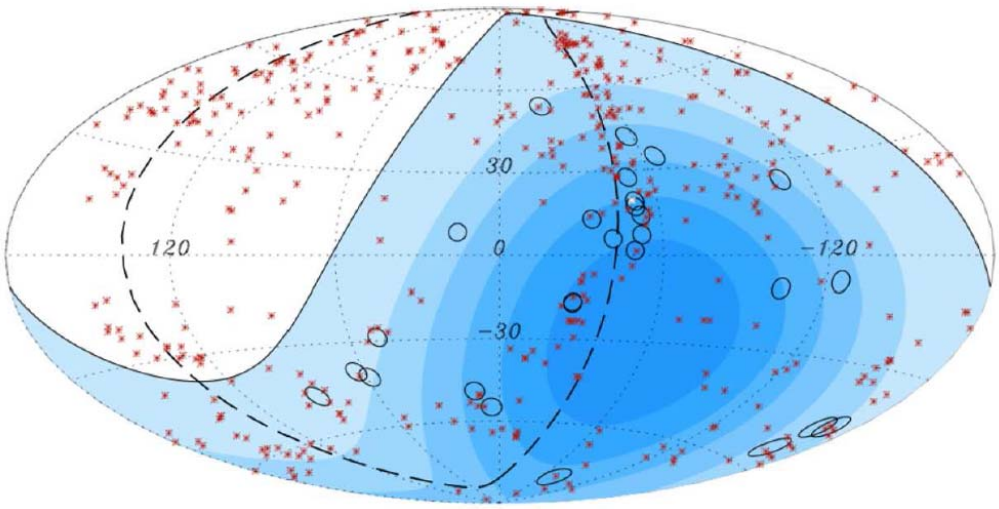

Figure 2.6: Aitoff projection of the celestial sphere in galactic coordinates with circles of 3.1° centered at the arrival directions of 27 cosmic rays detected by the Pierre Auger Observatory with reconstructed energies E > 57 EeV . The positions of the 442 AGN (292 within the field of view of the Observatory) with D < 75 Mpc are indicated by asterisks. The solid line draws the border of the field of view for the southern site of the Observatory (with zenith angles smaller than 60°). The dashed line is, for reference, the super-galactic plane. Darker color indicates larger relative exposure. Each colored band has equal integrated exposure. Centaurus A, one of the closest AGNs, is marked in white. [16]

Another point concerning the propagation of cosmic rays is their interaction with magnetic fields. The particles are deflected and their trajectories become more and more chaotic with decreasing energies. We have already seen in the last section that particles with energies below 10^{18} eV are trapped inside our galaxy. Is seems clear that such particles can not point back directly at their sources (if the propagation distance is adequately large). With intergalactic magnetic fields in the order of nG simulations predict that for protons with energies larger than $4 \cdot 10^{19}$ eV the deflections are not strong enough to prevent UHECRs to point back at their sources in a significant fraction of the sky [15]. Thus these particles can be used to identify the sources of cosmic rays. Together with their loss of energy due to their interaction with the CMB the sources should show an anisotropy in the celestial sphere. This will be discussed in more detail in the following section.

2.4 Anisotropy

In the last section we discussed that the highest energy cosmic rays detected must have their sources closer to Earth than $\sim$ 100 Mpc. Due to the fact that there are not so many possible candidates which may accelerate particles to such energies (cf. figure 2.4) it is a sensible assumption that there should be an anisotropy in the arrival direction of the particles with the highest energies.
Since active galactic nuclei (AGNs) are one of the most promising source candidates the Pierre Auger Collaboration has examined a possible correlation between

the arrival direction of cosmic rays and the position of AGNs. By comparing the experimental results with independently generated data where sources are isotropically distributed over the sky, the collaboration has been able to reveal a correlation between the directions of arrival and positions of AGNs [16].
Three parameters have influence on the correlation: The maximum distance between a considered AGN and Earth D_{max}, the maximum deviation of the arrival direction from the position of an AGN ψ and the energy threshold E_{th}. The latter is motivated by the fact that only the particles of the highest energies point back to their sources. Nevertheless even those particles are slightly deflected by magnetic fields. Furthermore the used detector has a finite angular resolution so that an adequate value for ψ has to be taken into account. Due to the interaction of the UHECRs with the CMB there should be a maximum distance from which UHECRs can reach the earth, i.e. D_{max}.
The Pierre Auger Collaboration has used $D_{max} = 75$ Mpc, $\psi = 3.1°$ and $E_{th} = 57$ EeV[2]. 27 cosmic ray events were found in the experimental data within these restrictions. With those the collaboration has established an anisotropy with more than 99% confidence level. This means that less than 1% of randomly generated isotropic distributions of AGN would lead to the experimental observed data. The most famous plot of the collaboration's work is shown in figure 2.6.

[2] 1 EeV = 10^{18} eV

3. Cosmic Ray Induced Air Showers

In 1939 P. Auger found coincidences in particle detectors which where up to 300 m away from each other. The coincidences decreased when his counters had a larger distance to each other. He concluded that this was because of *air showers* [17].
When a *primary particle* , i. e. a cosmic ray, enters the atmosphere it will collide with a nucleus of the air. From this interaction new so-called *secondary particles* emerge. These particles will interact with the air as well and a cascade of particles will arise. This cascade is the air shower.
The density of the atmosphere decreases exponentially with the altitude and has a slant depth ≈ 1000 g cm^{-2}. Since the electromagnetic radiation length is $X_0 = 36.66$ g cm^{-2} and the hadronic interaction length is $\lambda = 90.0$ g cm^{-2} the atmosphere has a thickness of about 27 electromagnetic radiation lengths and 11 hadronic interaction lengths. Since most of the cosmic rays are nuclei the focus in this work will be on these primary particles. Since for UHECRs the binding energy of heavier nuclei is much smaller than the energy of the primary particle E_p, such a nucleus can be considered as a superposition of A protons with energies E_p/A where A is the mass number of the heavier nuclei.

3.1 Reactions in the Atmosphere

Figure 3.1 shows a schematic overview of the shower development.
The proton has its first interaction at heights about 15 to 20 km. In a reaction with a nucleus of the air it loses about 50% of its energy and produces $\sim 90\%$ pions ($\pi^0, \pi^\pm$) and $\sim 10\%$ kaons ($K^0, K^\pm$). All these particles, except the π^0, interact with the air as well, producing the *hadronic cascade* - or they decay:
The mean life time of the uncharged pion $\tau_{\pi^0} \approx 10^{-16}$ s is too short for further reactions so that the π^0 will decay to 2γ with a branching ratio of 99% or to $e^+e^-\gamma$ with a branching ratio of 1%. The products are part of the *electromagnetic cascade*.
The mean life times of the charged pions and the kaons are about 10^{-8} s. In almost every case the π^+ decays to $\mu^+\nu_\mu$ ($\approx 99.99\%$). For K^0 the decay modes are $\pi^+\pi^-$ (69%) and $\pi^0\pi^0$ (31%). Furthermore there will be $K^+ \longrightarrow \mu^+\nu_\mu$ (64%), $\pi^+\pi^0$ (21%) and many more modes with smaller branching ratios in which predominantly pions are produced. But there will also be a small amount of muons, positrons and the corresponding neutrinos. The decays of π^- and K^- can be obtained by charge conjugation from the ones of their anti-particles.
In the electromagnetic cascade the photons might react with nuclei in the atmosphere

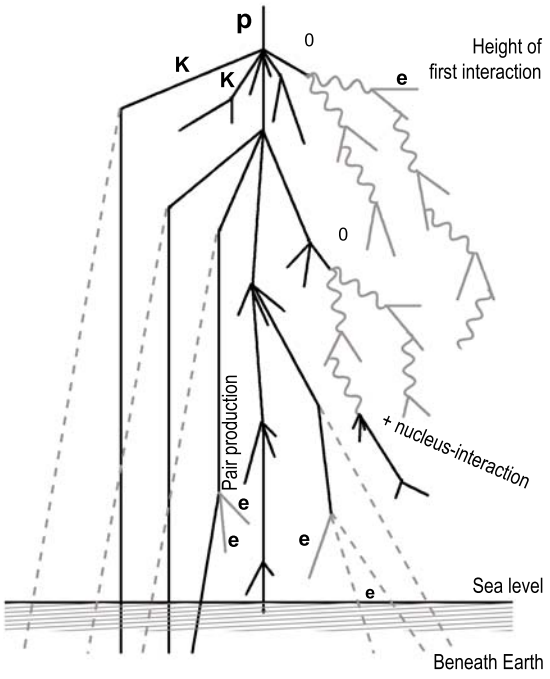

Figure 3.1: Schematic view of the air shower development.

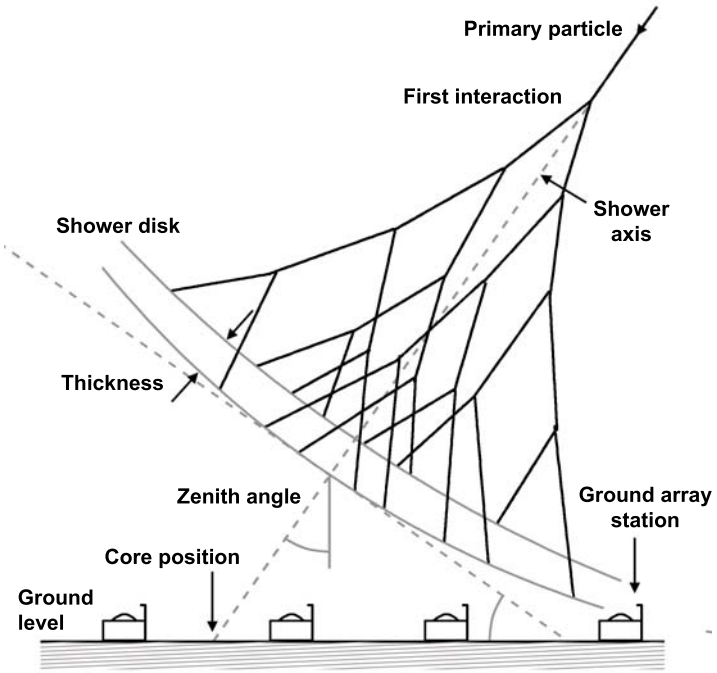

Figure 3.2: Schematic view of an air shower approaching a ground array.

as well creating again pions and kaons. In this case energy inside the electromagnetic cascade is reposited to the hadronic cascade. But most commonly the photons will create electrons and positrons via pair-production and Compton-scattering. The electrons and positrons themselves create photons by Bremsstrahlung and annihilation. In the *muonic cascade* a small amount of the muons might decay to $e^+\nu_e\bar{\nu}_\mu$ but most of them reach the ground since they are little affected by Bremsstrahlung due to their relatively high mass. They obtain energies of typically some GeV and their energy loss evoked by ionization is 2 MeV / (g cm^{-2}). The neutrinos do not interact. Their number is equal to the one of the muons and they carry just a small amount of the total shower energy. Therefore the atmosphere is a calorimeter with good linearity.
The electromagnetic cascade dies out at energies $\sim$ 1 MeV. From that point electrons and positrons only lose energy by ionization until they are stopped. The hadronic cascade comes to an end when all pions and kaons have decayed. The point with the maximum number of particles is called X_{max}. The mean X_{max} lies at about 700 g cm^{-2} to 800 g cm^{-2} for ultra-high-energy primary protons and about 100 g cm^{-2} deeper for iron nuclei as primary particle[1]. Figure 3.3 shows $< X_{max} >$ vs. the primary energy gained from simulations. (For more information about shower simulations see paragraph below.)
The distribution of the cascade components is about 90% electromagnetic, 5% muonic, 5% neutronic and a small amount of hadrons.
The shower propagates with nearly the vacuum speed of light. Its *lateral* stretch varies with the type of particles: hadrons are concentrated in a cylinder of 10 m radius around the shower axis. Due to multiple scattering electrons and positrons reach distances of about 100 m away from the shower axis. Since muons have a high penetration ability they reach the ground from higher altitudes and can therefore also be found up to distances of more than 1 km away from the shower axis. The *longitudinal* spread ranges from a few meters close to the core to some tenths of meters in the outer region. This spread is called the *shower disk*. It is not flat but has a curvature. Figure 3.2 shows a schematic view of an air shower approaching a ground array. The shape does not depend on the energy of the primary particle due to the large number of interactions but the Earth's magnetic field might influence the shape. Nevertheless P. Billoir showed in [18] that this effect is negligible for zenith angles $\theta < 60°$.
On the other hand two showers with the same primary energy and the same zenith angle do not look the same since the point of the first interaction changes within the order of one hadronic interaction length. This evokes fluctuations of X_{max} and the lateral profile and is called *shower-to-shower fluctuations*. Depending on the shower development there exists a distance where the fluctuation of particle density is reduced to 10% - this is at about 1000 m away from the shower axis at sea level for a primary energy of 10^{19} eV.

Simulations of Air Showers

Simulations in physics are a powerful tool since they allow a sophisticated comparison between experimental data and considered theoretical models. Furthermore the

[1]Measured from the top of the atmosphere down towards the Earth.

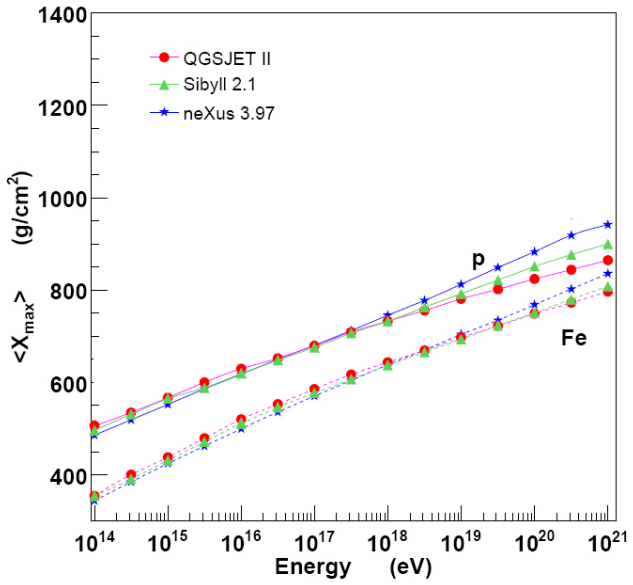

Figure 3.3: Simulation: Mean X_{max} vs. primary energy for the primary particle being a proton (p) or an iron nucleus (Fe). The different colors mark the use of different models for the hadronic interaction (see paragraph below). (Modified, original taken from [4]).

simulations of detectors give the physicists and engineers a deeper understanding of their devices before they are actually assembled.
Any simulation needs a model on which it is based. Because these models always imply approximations to describe nature's real behavior, a comparison between simulated end experimentally gained data is essential.

To simulate air showers the use of CORSIKA (COsmic Ray SImulations for KAscade), a FORTRAN based simulation software, is common. Basically the user chooses the type of the primary particle, its energy and arrival direction and the software calculates all possible particle reactions in a model atmosphere until the particle decays or reaches a defined observation level. To compute the cross sections of the reactions CORSIKA uses external programs. For electromagnetic reactions the models used by these external programs are expected to be correct for all energies. This is not the fact for hadronic interactions at the highest energies. Here one uses models which are extrapolated from high-energy-physics accelerator data such as EPOS, QGSJET or SIBYLL. All of them make different assumptions to describe hadronic interactions at the highest energies. So the simulation results do not only contain statistical uncertainties but also systematical ones. Typically the user runs several of these external programs (see e.g. figure 3.3).
An air shower simulated with CORSIKA can be seen in figure 3.4. For more information about CORSIKA regard [20].

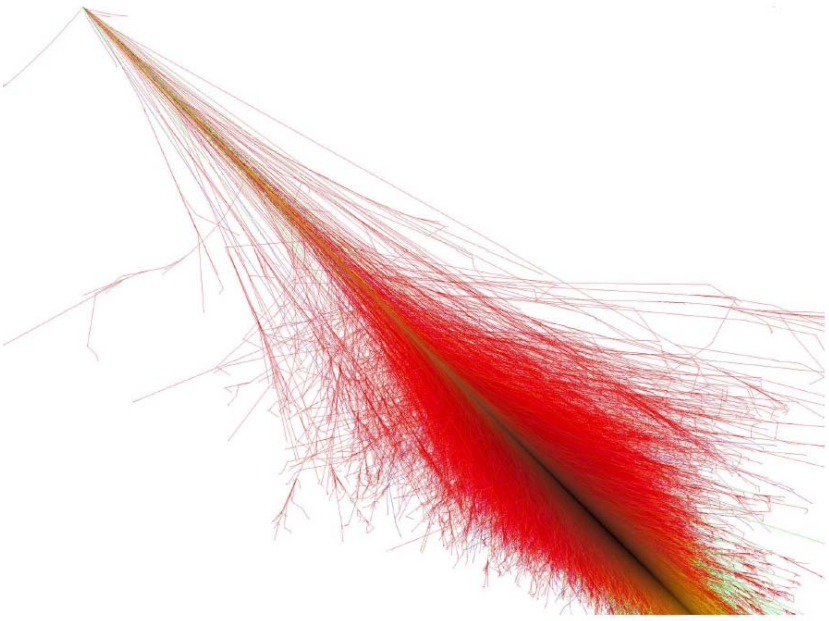

Figure 3.4: An air shower simulated with CORSIKA. The primary particle is a 10^{15} eV proton. The electromagnetic cascade is illustrated in red, the muonic cascade in green and the hadronic cascade in blue. The longitudinal stretch is about 72 km [19].

3.2 Measurement of the Lateral Shower Profile with Ground Arrays

The lateral shower profile is measured with a *ground array*, i.e. several detector stations at certain distances from each other at the ground. (A more detailed view of the Pierre Auger Observatory's ground detector will be given in section 4.1.) The area required relates to the rate of events being studied and for UHECRs must be many square kilometers. The detector stations are often arranged in a grid and for UHECRs the distance from one station to another is typically hundreds of meters, so that the detector samples the shower.
The first step in analyzing the shower is to reconstruct the shower axis. In a first approximation the assumption can be made that the shower disk is flat. It will hit the different stations at different times depending on the direction of arrival of the air shower. With this timing information it is possible to reconstruct the arrival direction and impact point of the core. This works out as well in a more sophisticated way for a shower disk with a curvature. A schematic view of the shower disk approaching to a ground array has been shown in figure 3.2.

In the Heitler Model [21] the total number of particles in an air shower is

$$N_{tot} \propto E_p^{\beta} \,, \tag{3.1}$$

wherein E_p is the energy of the primary particle and the index $\beta \approx 1$. Only $N < N_{tot}$ particles reach the ground since particles get absorbed and decay. N depends on

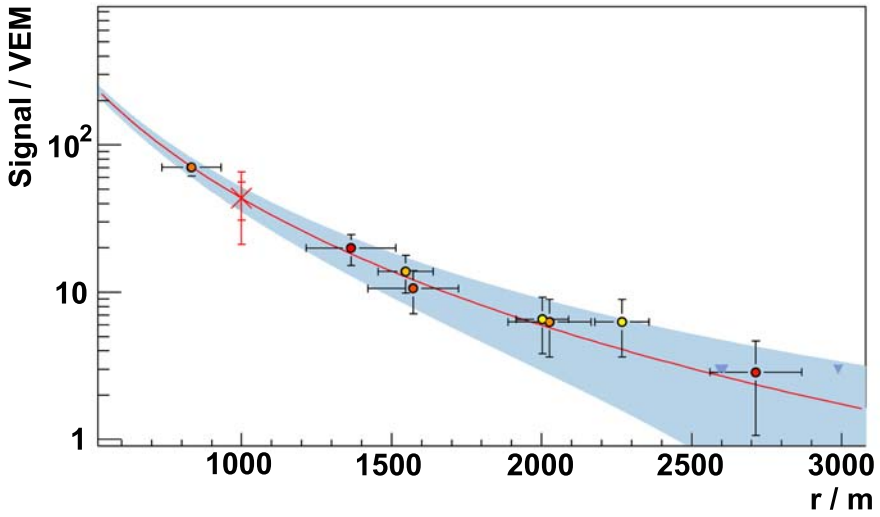

Figure 3.5: Shower signal measured with the ground array of the Pierre Auger Observatory at different distances from the core. The reconstructed energy of the primary particle is 2.2 $\cdot 10^{19}$ eV. The signal is measured in units of a signal caused by a single muon hitting the detector vertically (VEM). Stations which have detected a signal contribute a colored datapoint. Their color code contains the timing information. The blue triangles to the right come from stations without signal. The red line is the fit of the lateral density function to the data with the blue band indicating the uncertainties of the fit. The red cross marks the reconstructed signal in a distance of 1000 m from the core position.

the *age* of the shower, i.e. the time (or distance) a shower traverses through the atmosphere. If the shower approaches the ground array under a higher zenith angle θ its way through the atmosphere is much larger. For example a vertical shower ($\theta = 0°$) is dominated by electrons and positrons, whereas a *horizontal* or *very inclined shower* with $\theta > 60°$ is dominated by muons since most of the positrons and electrons were absorbed due to ionization.
The detector stations detect the particle density

$$n = n(r) \qquad \text{with} \quad N = \int n(r)dr \tag{3.2}$$

with r being the distance to the shower core. Besides this core - which has a diameter of about 100 m - for scintillation detectors the lateral particle density falls off according to the Nishimura-Kamata-Greisen (NKG) formula [13]

$$n(r) = k \left(\frac{r}{r_0}\right)^{-\alpha} \left(1 + \frac{r}{r_0}\right)^{-(\eta-\alpha)} . \tag{3.3}$$

The factor k is proportional to the number of particles in the shower N. r_0 is the Molière-radius (the product of one radiation length and the root mean square deflection of a particle of critical energy traversing one radiation length). 95% of the shower energy is deposited inside a cylinder with the radius r_0 around the shower

axis. The parameters α and η are derived by experimental data and vary with the age of the shower. The NKG formula allows a fit to the lateral particle density measured with the ground array and a determination of the impact point of the core. To do so one takes a trial core position and searches around this location for a position at which the fit between the observed and expected densities is optimum. Usually a chi-squared minimization or maximum-likelihood procedure is adopted, with the core search taking place in a plane projected perpendicular to the shower axis. To estimate the energy of the primary particle one fits to the observed particle density. It has been shown that the differences in particle density far away from the core due to shower-to-shower fluctuations are rather small and hence the density depends only on the primary energy.
Since the ground array only detects the shower at the ground level it observes just a cross section of the whole shower development.

3.3 Measurement of the Longitudinal Shower Profile with Fluorescence Telescopes

While the secondary particles traverse the atmosphere they excite nitrogen molecules. When it de-excites it emits isotropically fluorescence light in the far visible and ultra-violet region. This light is detected as time sequence by an arrangement of mirrors and photomultipliers called *fluorescence telescope*. (A more detailed view about the Pierre Auger Observatory's fluorescence telescopes will be given in section 4.2.) It is able to monitor the whole shower development in its field of view. With the information at which time the shower is at which point in the sky the shower axis can be reconstructed. If furthermore at least two telescopes have traced the shower down no timing information is needed to reconstruct the shower axis. The information a telescope gains is corrected for geometrical effects and scattering and absorption processes the fluorescence light receives during its propagation to the detector.
With the knowledge of the fluorescence yield of nitrogen and the information which amount of fluorescence light has been detected at a certain point the electron/positron content of the shower at this specific point $N_e(X)$ can be determined. After applying corrections for direct and scattered Cerenkov light (which contaminates the signal) $N_e(X)$ is directly proportional to the photoelectrons of the photomultiplier and follows the Gaisser-Hillas formula [22]

$$N_e(X) = N_{max} \left(\frac{X - X_0}{X_{max} - X_0} \right)^{\frac{X_{max} - X_0}{\lambda}} \exp\left(\frac{X_{max} - X}{\lambda} \right) \tag{3.4}$$

Herein, N_{max} is the number of particles at X_{max} and X_0 and λ are parameters of the shape of the shower. X_0 is considered as the point of the first interaction and λ as absorption length.

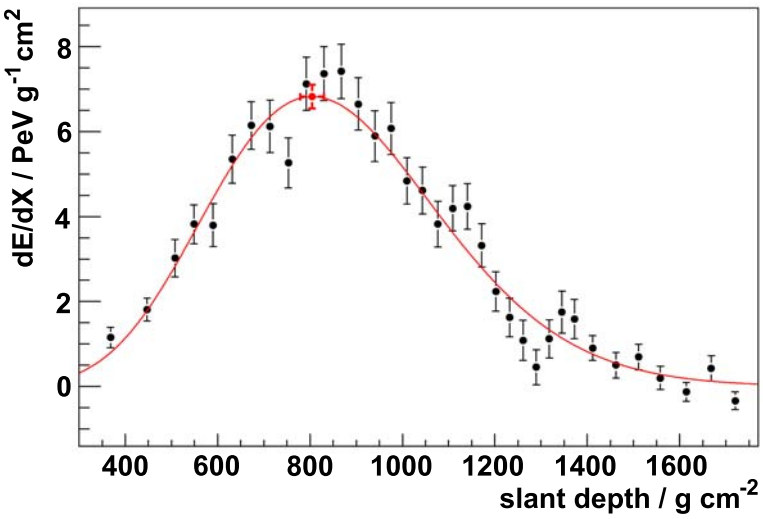

Figure 3.6: Energy deposit of the shower particles versus the atmospheric depth. The black dots are the data taken by the fluorescence telescope. The Red line is the Gaisser-Hillas fit. The reconstructed $X_{\max}$ is marked by the red dot. The reconstructed energy of the primary particle is 3.6 $\cdot 10^{18}$ eV.

According to [13] the energy carried by the electromagnetic components is

$$\begin{aligned} E_{em} &= \frac{\text{(critical energy of electron in air)}}{\text{(radiation length of electron in air)}} \cdot \text{(total track length in g cm}^{-2}\text{)} \\ &= (2.18\text{MeV}) \cdot \text{(total track length in g cm}^{-2}\text{)} \end{aligned} \tag{3.5}$$

Depending on the primary energy and the primary mass the fraction of energy passed to the electromagnetic component for hadronic showers is about 80-90% of the total shower energy. The shower-to-shower fluctuation of the number of electrons at X_{max} fluctuates about 10% for proton primaries. Making an assumption about the shape of the cascade the total track length is determined by the integral $\int_0^\infty N_e(X)dX$ and the primary energy can be estimated as

$$E_p = (2.65\text{MeV}) \cdot \int_0^\infty N_e(X)dX\,. \tag{3.6}$$

Since the intensity of the fluorescence light is relatively low, fluorescence telescopes have to be operated in non-light polluted areas during clear and moonless nights. This leads to a duty cycle of about 10%.

3.4 Radio Pulses Emitted From Extensive Air Showers

If an air shower traverses through the atmosphere it will emit coherent radiation in the radio band. These pulses can be measured with an adequate arrangement of

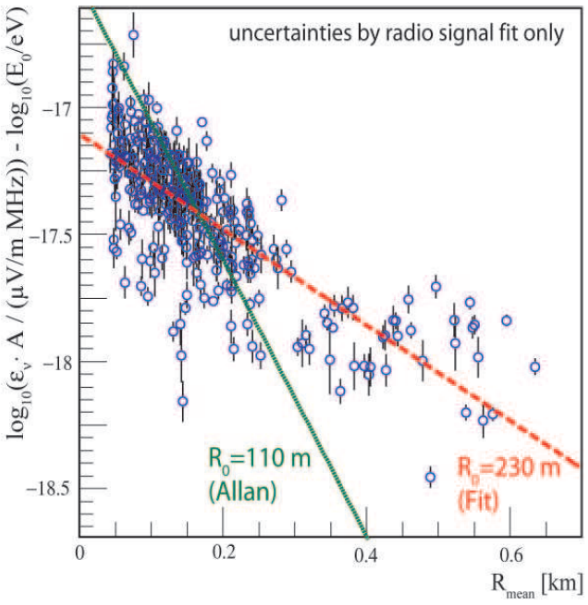

Figure 3.7: Normalized logarithm of radio pulse amplitudes as function of the lateral distance R from the shower axis measured at LOPES. Indicated are the parameters R_0 as given by Allan and as determined directly from the data [23].

antennas and receivers.
J. V. Jelley and co-workers were the first to detect such pulses in coincidence with Geiger counters in 1965 at a frequency of 44 MHz [24]. In the following years various groups claimed detection of radio signals emitted by air showers with frequencies ranging from 2 MHz up to 520 MHz.

G. A. Askaryan suggested in 1962 that the annihilation of positrons in an air shower would lead to a negative charge excess. This would result in Cherenkov radiation as the shower rushes trough the atmosphere. If the size of the emitted wavelength is larger than the size of the emitting region, i.e. the shower disk, the radiation is coherent. In this case the radio flux would grow quadratically with the number of particles and not linear as in the noncoherent case [25].
However, observations showed that the emission is dependent on the geomagnetic field which cannot be described through the Askaryan effect.
In 1966 F. D. Kahn and I. Lerche introduced an explanation of radio emission from extensive air showers which can describe this dependency [26]. In a frame moving along with the shower electrons and positrons would drift into opposite directions due to the Lorentz force. This leads to a transverse current which emits dipole radiation. Lorentz-transformed into the lab system the boost produces strongly forward-beamed radiation compressed in time into an electromagnetic pulse.
In the late 1960s the interest in this experimental field was very strong but deceased almost completely due to difficulties with radio interference, interpretation of experimental data and also the success of other detection techniques like water Cherenkov tanks used in ground arrays.

However, H. Falcke and P. Gorham revived this field of interest in 2003 when they interpreted the radio emission as geo-synchrotron radiation of charged particles gyrating in the geomagnetic field [27][2]. This description has the advantage that the underlying synchrotron theory is well understood. Nevertheless, since this model and the one from Kahn and Lerche use the same effect as starting point both models might describe the same in different formalisms.

In an extensive review H. R. Allan summarized the properties of radio pulses emitted by air showers in 1971 [28]. The main result is the empirically gained approximate formula 3.7 which relates the received time-integrated voltage of air shower radio pulses ϵ_ν to various parameters:

$$\epsilon_\nu = 20 \cdot \left(\frac{E_p}{10^{17}\ \mathrm{eV}}\right) \sin\alpha\ \cos\theta\ \exp\left(-\frac{R}{R_0(\nu,\theta)}\right) \mu\mathrm{V\ m^{-1}\ MHz^{-1}}\,. \tag{3.7}$$

Herein E_p is the primary energy and R is the distance from the shower core. α denotes the angle between the direction of arrival of the shower and the vector of the geomagnetic field. With higher inclination θ the radio signal is attenuated since X_{max} is farer away from the point of observation. This is respected by the term $\cos\theta$. The lateral dependence is described by $\exp(-R/R_0(\nu,\theta))$. The parameter R_0 depends on the inclination and the frequency ν. The Haverah Park experiment found $R_0 = (110 \pm 10)$ m for $\nu = 55$ MHz and $\theta < 35°$. R_0 becomes slightly larger for lower frequencies and higher inclinations, e.g. at $\nu = 32$ MHz the parameter R_0 is about 140 m [29].
However, recent results from the LOPES experiment determined $R_0 = (230 \pm 31)$ m [23] (cf. figure 3.7).
The radiated synchrotron power of a particle with charge q and mass m is (see standard literature on theoretical electro-dynamics, e.g. Jackson [30])

$$P_\mathrm{s} = \frac{2}{3}\,\frac{q^2\,c}{r^2}\,\beta^4\,\gamma^4 \tag{3.8}$$

with r being the gyro-radius, $\beta = v_\perp/c$ the velocity of the particle perpendicular to the axis of rotation given in units of the speed of light c and $\gamma \approx E/m$ the Lorentz-factor. E is the energy of the particle. The gyro-radius caused by a magnetic field $\vec{B}$ is

$$r = \frac{\gamma\,m\,v_\perp\,c}{q\,|\vec{B}|} \tag{3.9}$$

Replacing the gyro-radius in equation 3.8 and $|\vec{B}| = B$ it follows

$$P_\mathrm{s} = \frac{2}{3}\,\frac{q^4}{m^2\,c^5}\,v_\perp^2\,\gamma^2\,B^2\,. \tag{3.10}$$

Using $\gamma \approx E/m$ for the radiated power is found

$$P_\mathrm{s} \propto E^2, \quad P_\mathrm{s} \propto m^{-4} \tag{3.11}$$

[2] Also to mention is modern digital technology which allows more sophisticated antenna receivers than in the 1960s and '70s.

To consider coherent emission the shower particles may be described as a single particle with the mass $N \cdot m$, the charge $N \cdot q$ and the energy $N \cdot E$. Using equation 3.10 it can be seen that the total power emitted by the shower is

$$P = N^2 P_s \tag{3.12}$$

which means that for coherent showers the power scales quadratically with the number of particles of the shower. This power is proportional to ϵ_ν^2.
Since the large number of electrons and positrons within an air shower and their small mass, regarding 3.11 one can conclude within good approximation that the radio pulses are induced by these particles.
Great advantages of a *radio detector* are its 100% duty cycle, the possibility of calorimetric measurements with gaining information about the longtudinal evolution of the shower and a very good angular resolution (cf. section 4.3). However, to exploit these advantages the physics of radio emission have to be understood in great detail. One effort towards better understanding of the experimental data are sophisticated simulations of the radio signals emitted by the air showers.

Simulations of Radio Pulses Induced by Air Showers and Recent Results

One simulation software, based on calculations of the electromagnetic field in the time-domain of each particle in an air shower, is the REAS code presented by T. Huege in 2004 (REAS1 [2]). The current version REAS2 [31] uses air shower parameters generated by CORSIKA (see end of section 3.1) as input. Both take the geo-synchrotron model into account. The simulations allow a much more detailed way of analyzing data than the analytical approach since the latter is based on further approximations. And since statistics of experimental radio emission data is still very low, especially for UHECRs, actual scientific progress in this field without simulations would yet be unthinkable.
Figure 3.8 shows the electric field of a radio pulse induced by a vertical proton shower as a function of the primary energy simulated with REAS1. The set of curves describes different distances of the observer to the shower core into North direction. The electric field is well described as a power law $E_p^{\kappa(r)}$ with $\kappa(r)$ close to one. $\kappa(r)$ is not constant due to changes in the depth of the shower maximum X_{max} [32]. The spectrum of the electric field simulated with REAS2 is given by figure 3.9. This is for a vertical 10^{17} eV proton induced shower and the set of functions is for different distances from the shower core. For higher frequencies the loss of coherence affects the characteristics of the curves since the wavelength gets shorter than the signal emitting region. Furthermore, for higher distances the signal drifts to lower frequencies. This is an interesting feature for designing a radio detector array. Due to achieve low costs in setting up such an array one would like to make the spacing between neighboring antennas as far as possible. This needs antennas which are still sensible at low frequencies. The sensitivity of an antenna to low frequencies is limited by the mechanically realizable size of the antenna and the galactic noise (see section 4.3).
Figure 3.10 shows a comparison of the emitted pulse between simulations run with REAS1 and REAS2. As before the shower was induced by a vertical 10^{17} eV proton.

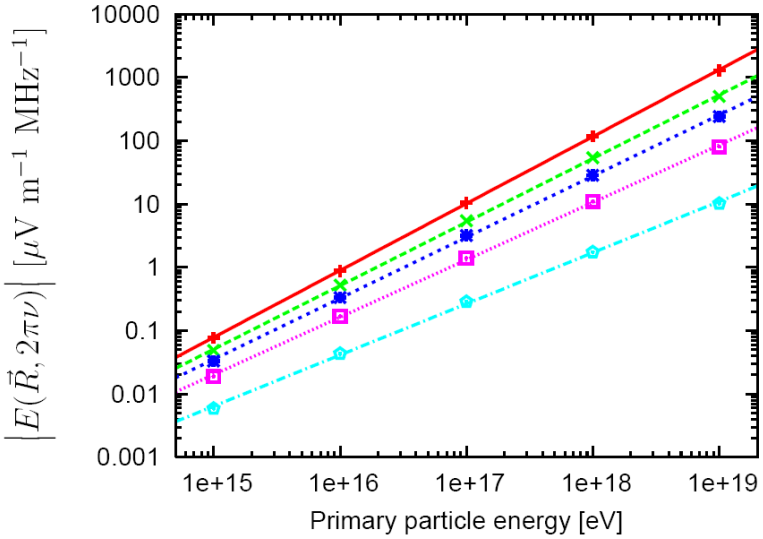

Figure 3.8: Simulated scaling of the field strength emitted at $\nu = 10$ MHz by a vertical air shower as a function of primary particle energy. The magnetic field strength is 0.5 G and its inclination is 70°, which approximately corresponds to the configuration present in central Europe. From top to bottom: $|\vec{R}| = 20$ m, 100 m, 180 m, 300 m and 500 m to the north from the shower center. The field strength scales as a power-law with index close to unity, as expected for coherent emission. The air shower initiating cosmic ray is a 10^{17} eV vertical proton [32].

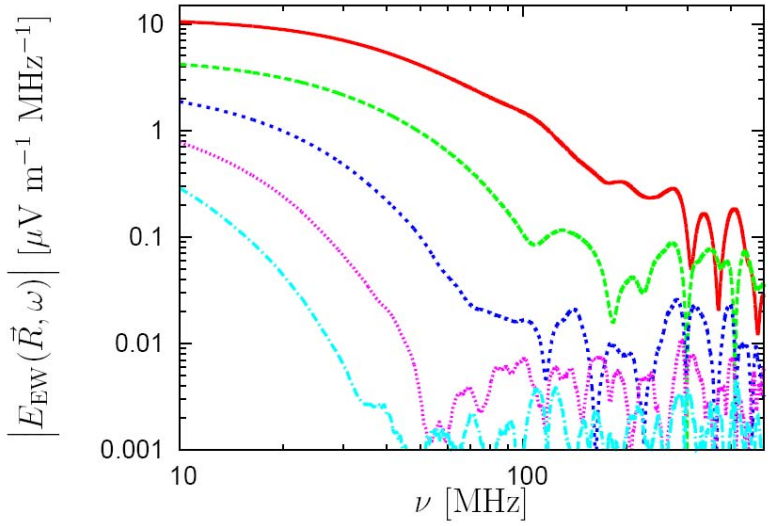

Figure 3.9: Simulated radio pulse spectrum. The strength of the electric field in east-west polarization of a radio pulse as function of the frequency at various distances from the north. The magnetic field strength is 0.5 G and its inclination is 70°, which approximately corresponds to the configuration present in central Europe. From top to bottom: $|\vec{R}| = 20$ m, 140 m, 260 m, 380 m and 500 m. Towards higher frequencies the loss of coherence affects the characteristics of the curves. The air shower initiating cosmic ray is a 10^{17} eV vertical proton [32].

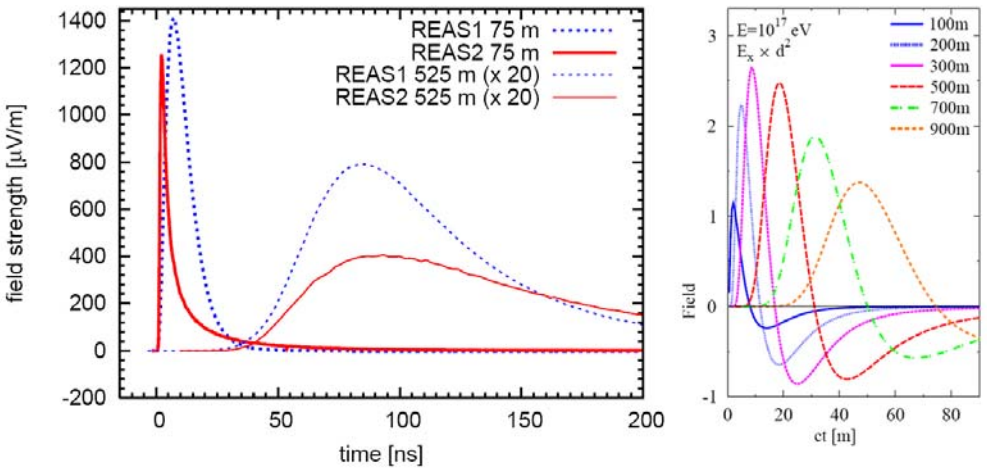

Figure 3.10: Left: Electric field of radio pulse vs. time as derived from simulations. Blue indicates results from REAS1, red from REAS2 (which uses CORSIKA) for observers at 75 m respective 525 m from the shower core. The signals at 525 m have been multiplied by a factor 20. A magnetic field of 0.48 Gauss with an inclination angle of 64.7°, as appropriate for the LOPES-location in Karlsruhe, Germany, is adopted. The shower is induced by a vertical 10^{17} eV proton [31]. Right: Electric field of radio pulse vs. time as derived from the macroscopic model [33]. The shower is induced by a vertical 10^{17} eV proton. The set of functions is for different distances of the observer from the shower core into x-direction in a Cartesian coordinate system with z to the zenith. The signals have been multiplied by these distances. The magnetic field strength is 0.3 G with the field vector pointing into y-direction. The main difference between both models is that REAS leads to unipolar, whereas the macroscopic model leads to bipolar pulses.

The simulations are run for observers at 75 m and 525 m distance from the shower core. In case of the 525 m distance the signal was multiplied by a factor 20. In comparison figure 3.10 shows also the pulse as computed by a macroscopic model by O. Scholten, K. Werner and F. Rusydi [33]. This model basically follows the ideas described by Kahn and Lerche (see above). There is one main difference between the REAS code and the macroscopic model: in the latter bipolar pulses occur, however, not if the REAS code is used. Prospective comparison with experimental data will allow to identify the correct model giving better insight on the physical basical principle.

A suitable radio detector has to determine the three shower parameter of interest: they are the arrival direction, the primary energy and the mass of the primary particle. With knowledge of the shape of the radio wavefront the arrival direction can be identified straight forward through the timing difference of the signals detected at different detector stations. Basically this works out as with a ground array[3]. Measurements and simulations so far see a power law describing the dependence of

[3]A basic difference between a radio detector and a ground array as mentioned in section 3.2 is that the radio detector is able to measure the whole shower development. The ground array detects only a cross section.

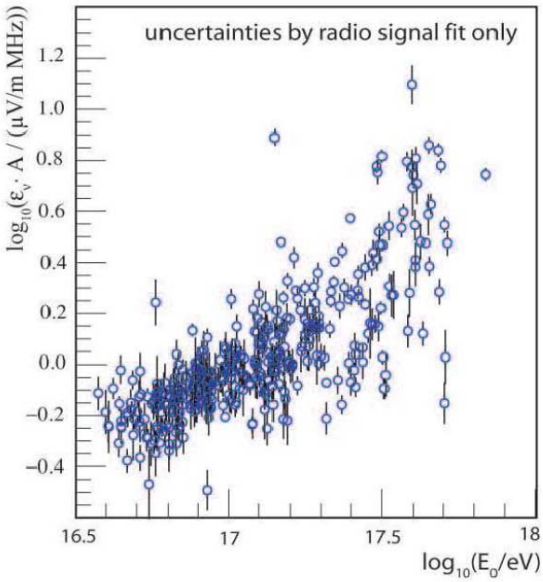

Figure 3.11: Log-log-plot of the normalized radio pulse amplitudes as function of the energy of the primary particle measured at LOPES [23]. Due to uncertainties in the data no fit has been performed, but a correlation is evident.

the radio pulse signal on the primary energy or at least a clear correlation. Recent results from the LOPES experiment are shown in figure 3.11. Here the normalized logarithm of the pulse amplitude is given as a function of the logarithm of the primary energy. Due to uncertainties in the experimental data no fit has been performed but the correlation is evident.
The reconstruction of the mass of the primary particle is rather unexplored. But intrinsic sensitivity is expected by simulations for different radio observables: the lateral pattern of the field strength (see figure 3.12), or by a longitudinal sensitivity which can be hidden in the pulse shape of the receiving signal, or in the wave front form, or in the frequency spectrum [34].

Recent results from the CODALEMA experiment and a radio detector test setup at the Pierre Auger Observatory are shown in figure 3.13. The reconstructed arrival directions of showers are given in local coordinates. For the test setup the statistics is still low. But in both cases there is a preferred arrival direction. This is a further step to the belief that the geo-synchrotron model is the right approach.

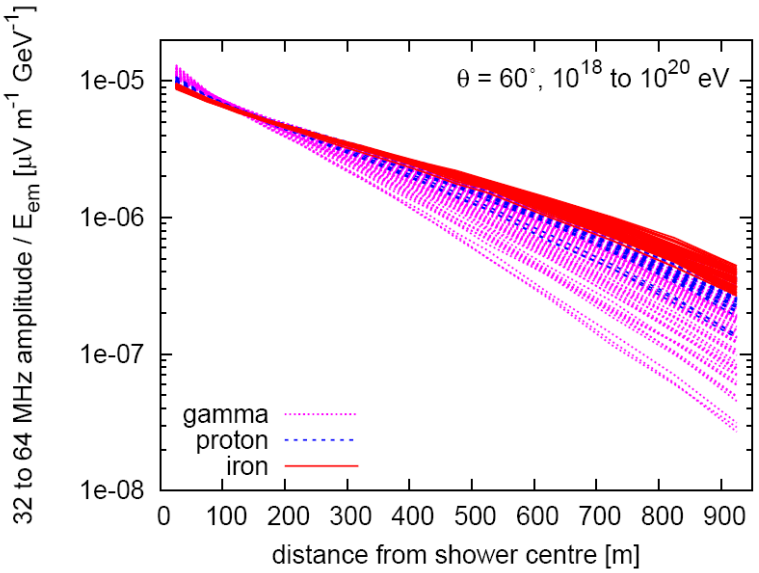

Figure 3.12: The normalized amplitude of the radio signal in the 32 to 64 MHz band as function of the distance from the shower core simulated with REAS2. The signal has been normalized with the energy deposited in the atmosphere by the electromagnetic cascade. The set of functions is for different primaries (proton, iron, gamma) and energies from 10^{18} eV up to 10^{20} eV. The inclination is $\theta = 60°$. The slope is sensitive to the mass of the primary particle [35].

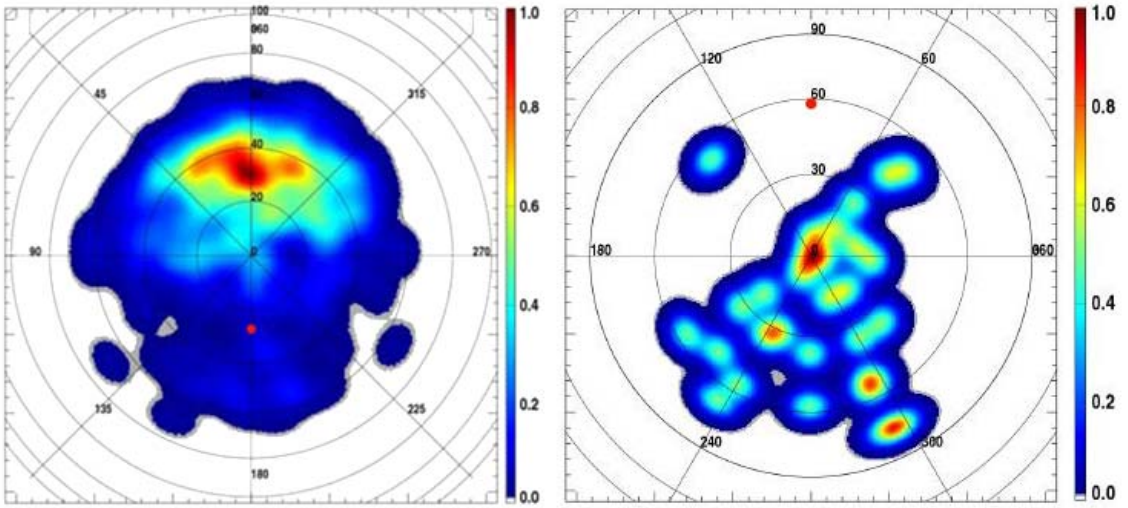

Figure 3.13: 10° Gaussian smoothed sky maps of observed radio events in local coordinates. The zenith is at the center, North is to the top, West to the left, South to the bottom and East to the right. Left: 619 events observed at CODALEMA, Nançay, France (northern hemisphere) [36]. Right: 37 events observed at a test setup at the Pierre Auger Observatory, Malargüe, Argentina (southern hemisphere) [37]. The red dots mark the direction of the geo-magnetic field at the observation sites.

4. The Pierre Auger Observatory

The Pierre Auger Observatory is an international observatory to detect UHECRs. It was proposed in 1992 by J. W. Cronin and A. A. Watson and will consist of the northern and southern site. The construction of the southern site has finished and is taking data since January 1st, 2004. It is located close to Malargüe in the Argentinian province of Mendoza and covers an area of about 3,000 km^2. Figure 4.1 shows the actual layout. The northern site is currently in the state of planning and will be situated near Lamar in the state of Colorado, United States of America. It will provide a detection area of about 20,000 km^2. Such large areas are necessary since the flux of the highest energy cosmic rays is very low (cf. section 2.1).
One unique feature of the Pierre Auger Observatory is the fact that it uses the advantages of a ground array in combination with the advantages of fluorescence telescopes. This combination makes the observatory a so called *hybrid detector* which allows cross-calibration of the two different detection techniques and a better insight to the physics of UHECRs.

In the following section the *Surface Detector* (i.e. the observatory's ground array) and the *Fluorescence Detector* will be explained. A description of the *Radio Detector* and the *Auger Engineering Radio Array* follows, since this work is about electronics for the Radio Detector. At the end of this chapter there will be a section about the further extensions of the southern site of the observatory.

4.1 The Surface Detector

The Surface Detector (SD) measures the lateral density and time distribution of particles in the shower front at ground level (cf. section 3.2). It consists of more than 1600 water Cherenkov tanks spaced by 1.5 km in a triangular matrix and is instrumenting an area of 3,000 km^2 (cf. figure 4.1). Each water tank is cylindrical and opaque with a diameter of 3.6 m made of polyurethane. Ten tons of very pure water are contained inside a sealed liner. Cherenkov light emitted inside the tank by shower particles is detected by three large diameter ($\sim$ 20 cm) hemispherical photomultiplier tubes which are mounted facing down. They look into the water through three sealed windows which are part of the liner. The liner prevents contamination of the water, works as a barrier for any external light and diffusely reflects the Cherenkov light. The tanks get their power from batteries fed by solar panels. With electronics, a GPS antenna and a communication antenna the hardware setup is complete [39] (cf. figure 4.2).

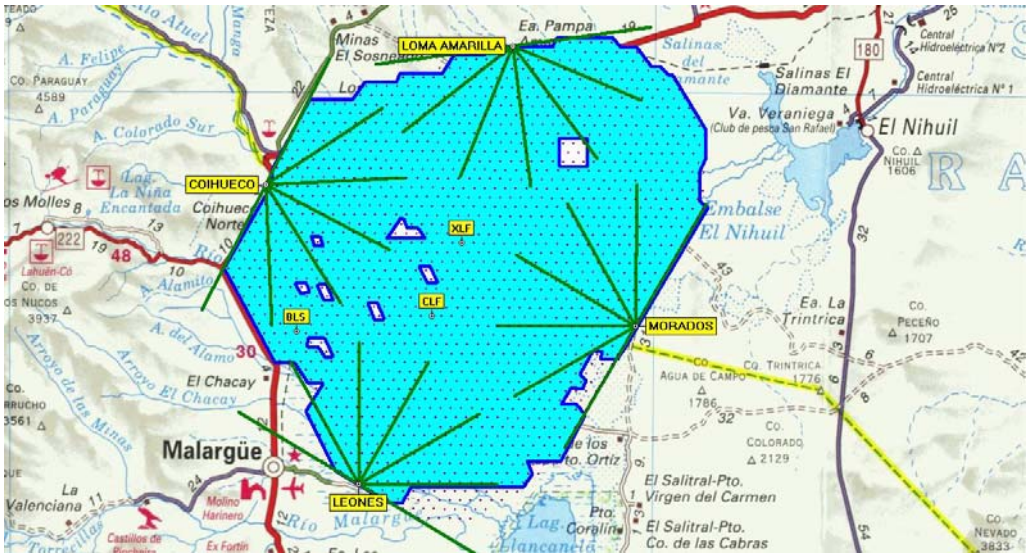

Figure 4.1: The southern site of the Pierre Auger Observatory. Each dot marks a water tank of the Surface Detector. They instrument an area of 3,000 km^2. The colored area indicates the currently operating stations. At the border of the array are the four Fluorescence Telescope buildings with 4 x 6 telescopes overviewing the area. Furthermore, the Balloon Launch Station (BLS), Central Laser Facility (CLF) and eXtreme Laser Facility (XLF) are marked. The picture shows the status of April 27$^{\text{th}}$, 2009. (Taken from [38].)

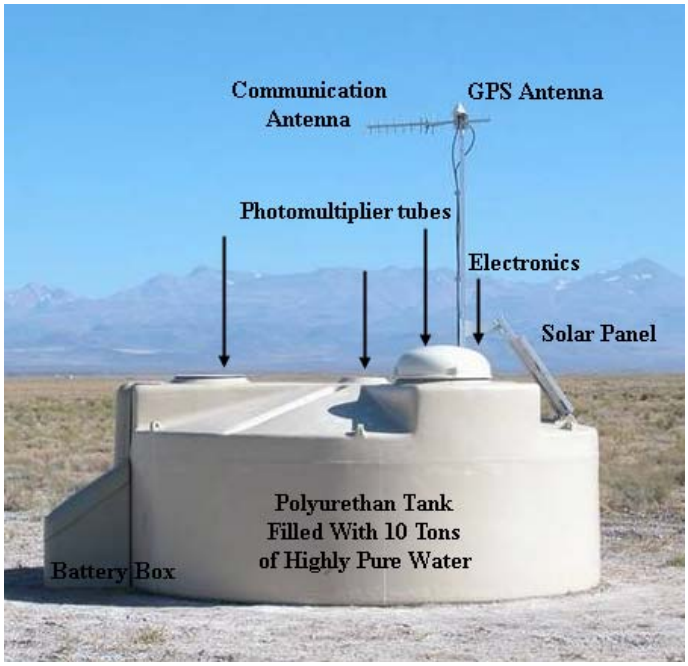

Figure 4.2: A Surface Detector Station. (Modified, original taken from [38]).

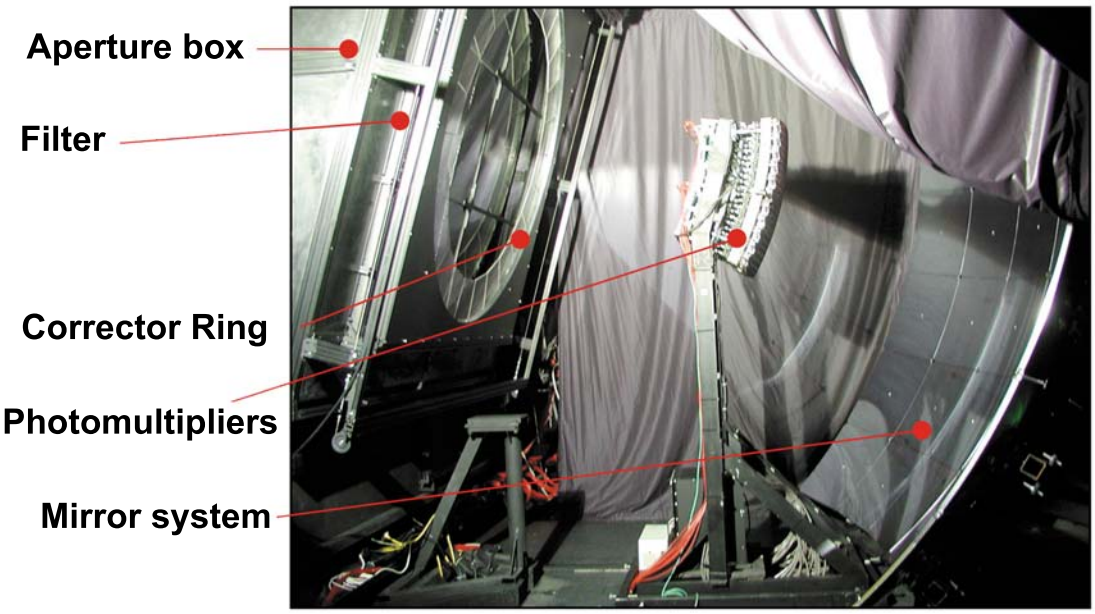

Figure 4.3: Fluorescence telescope. (Modified, original taken from [38].)

The energy threshold of the SD is $3 \cdot 10^{18}$ eV of primary energy. A hierarchical trigger system has been designed to allow the SD to operate at a wide range of primary energies, for both vertical and very inclined showers with full efficiency for cosmic rays above 10^{19} eV [40].
The SD achieves an angular resolution of $\sim 1.0°$ and an energy resolution of $\sim 20\%$ for primary energies above 10^{19} eV [41]. Its duty cycle is 100%.

4.2 The Fluorescence Detector

The primary purpose of the Fluorescence Detector (FD) is to measure the longitudinal profile of showers recorded by the SD whenever it is dark and clear enough to make reliable measurements of atmospheric fluorescence from air showers. The FD consists of 24 fluorescence telescopes. Always six of them are mounted in one of four buildings at the border of the SD area. Each telescope has a field of view of 30.0° x 28.6°, so that those in one building together observe the sky in 180.0° of azimuth and 0° to 28.6° of elevation. The elements of a telescope are a light collecting Schmidt optical system (diaphragm, filter and mirror) and the light detecting array of 440 hexagonal photomultiplier tubes (20 x 22 matrix). The light falls through a 2.2 m wide aperture with filter transmitting the nitrogen fluorescence wavelength range (300 to 400 nm) and corrector lens. The spherical mirror has a radius of curvature $R = 3.4$ m and reflecting area of 3.8 x 3.8 m^2. Shutters prevent light entering the buildings during the days and bright nights.
The FD achieves an angular resolution of $\sim 0.5°$ and an energy resolution of $\sim 10\%$ for primary energies above 10^{19} eV [41]. But its duty cycle is $\sim 10\%$ since it needs clear moonless nights to operate.

Figure 4.4: The fluorescence telescope building at Coihueco.

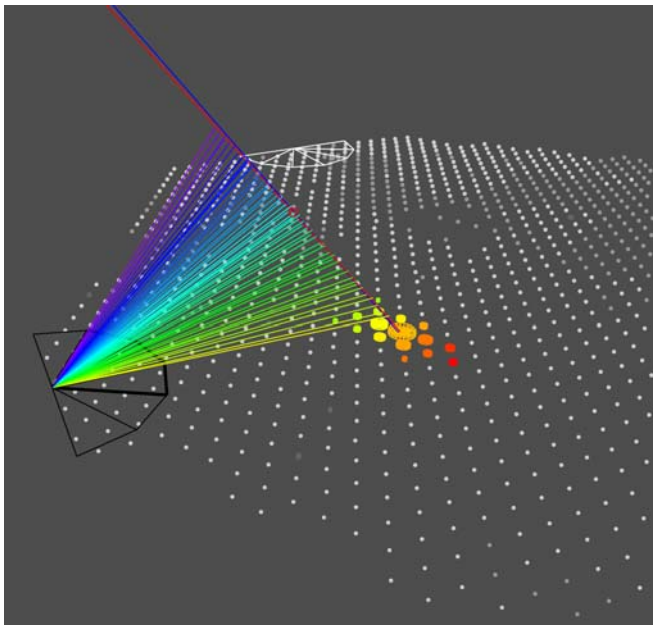

Figure 4.5: Event 2276329. It has been detected by fluorescences telescopes in one FD building and 16 SD stations. The red (for FD) and the blue (for SD) lines are the reconstructed shower axes. The other lines are the points where the shower has been seen by the FD with color-coded timing information. SD stations are marked by dots. Those with signal are colored, again with the color code containing the timing information. The bigger an SD station is the more signal it has received. The reconstructed energy of the primary particle is $1.5 \cdot 10^{19}$ eV.

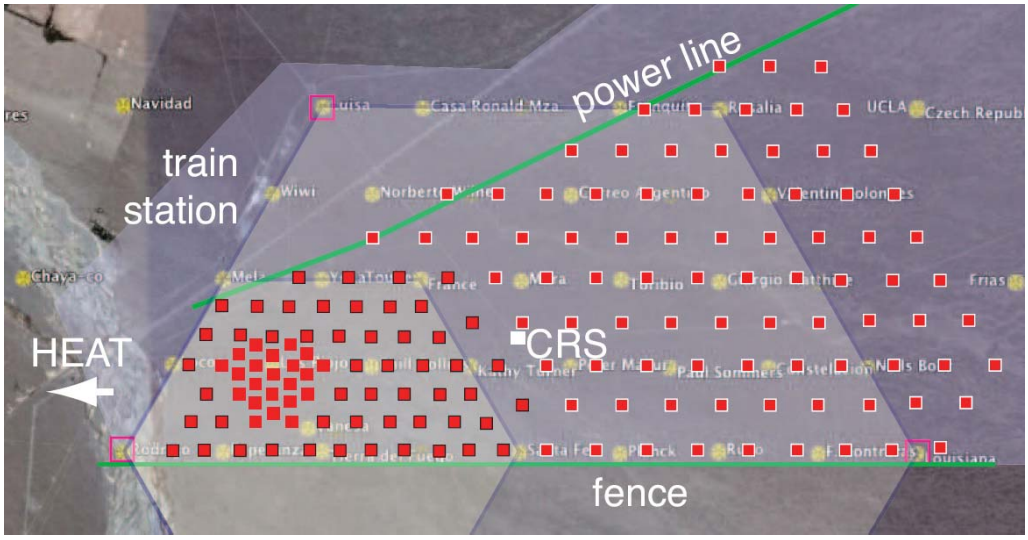

Figure 4.6: AERA site layout. Each red square marks the future position of a Radio Detector Station. In the middle of the array will the *Central Radio Station* (CRS) be located. Here the data acquisition will take place. Yellow dots mark the position of SD stations. The spacing between two neighboring stations inside the AMIGA area (big hexagon) is half the distance as the normal SD spacing. The small hexagon shows the infill-of-the-infill area of AMIGA. (Taken from [42].)

With the SD and FD in combination the Pierre Auger Observatory is operated as a hybrid detector. Figure 4.5 shows a hybrid event which has been seen by telescopes from one telescope building and 16 SD stations.

4.3 The Radio Detector

The radio detection technique has been studied at the Pierre Auger Observatory since 2006. Several relatively small test setups near the Balloon Launch Station (BLS) and the Central Laser Facility (CLF) (cf. figure 4.1) have investigated both, the physics issues as well as the technological ones. The program has been successful so that right at the moment the next step is taken: the collaboration has recently decided to go for the next phase of establishing a 20 km^2 *Auger Engineering Radio Array* (AERA). This will lead to more sophisticated physical results due to higher statistics.
AERA will consist of about 150 detector stations in a triangular grid (see figure 4.6). The sensitive part of each station is the antenna. The analog electronic chain consists of a low-noise-amplifier - which is designed within this work - filters and high-gain-amplifiers. The analog signal gets digitized at 12 bit and 160-200 MHz. The exact layout of the digital chain is not quite fixed but all in all can be described as a smart low power oscilloscope which has to be able to handle a single antenna trigger rate of 200 Hz. This requirement is obtained from measurements near the BLS. Furthermore each station has its own solar panels, batteries, GPS and communication antennas. Figure 4.7 shows a Radio Detector station.

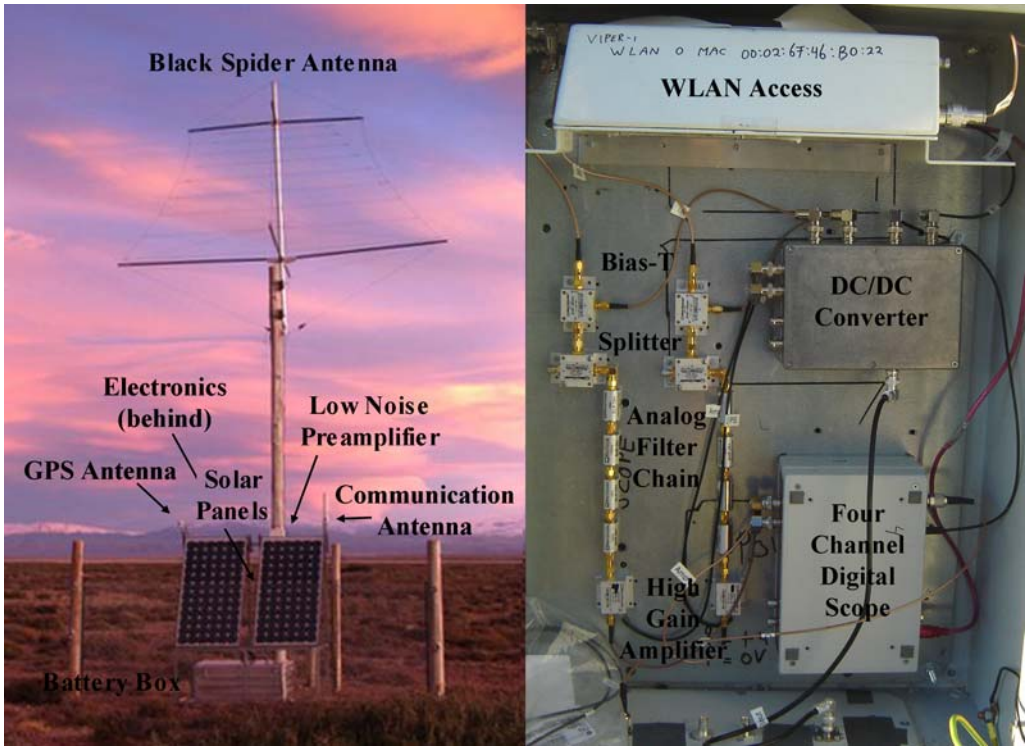

Figure 4.7: A Radio Detector station. (Left: Modified, original photography taken from [43].)

The technical demands on the used antennas are good broadband receiving characteristics from about 30 MHz to about 80 MHz, a high sensitivity towards the sky and a low sensitivity towards the ground, high gain in the sensitive area and good mechanical and UV resistance. They are motivated by the following points: As seen in section 3.4 the frequency of the emitted radio signals drift to lower values for larger distances of the antenna to the shower core. Therefore broadband devices are needed. The band gets limited by man-made-noise and the galactic noise. Above 80 MHz the frequencies are used by local radio broadcasting stations. Below 30 MHz the short wave band starts. Furthermore, the power spectral density of the galactic noise increases with decreasing frequencies. At 32.5 MHz is is already about -78 dBm MHz^{-1} for the antennas used for the radio detector [44].
A low sensitivity towards the ground is needed since the electronics are situated beneath the antenna and might interfere with the signals of interest. High gain in the sensitive area is needed to achieve a good signal-to-noise ratio. Since the weather conditions in the Argentinian pampa can become really rough (storms, snow, intense UV radiation) the antenna should be very resistant against these conditions. One antenna to fulfill these demands is the *Black Spider Antenna* (BS) [44], [45]. Several antenna types have been under testing (and are still) and the collaboration decided to go with the BS. The BS is a Logarithmic Periodic Dipole Antenna (LPDA). LPDAs are an arrangement of $\lambda/2$ dipoles connected to a central waveguide in a way that signals from different dipoles interfere constructively at the *footpoint*, i.e. the point where the antenna is read out.

AERA is the next step towards a new mature UHECR detector technique. The test setups have been very promising. So far 313 radio events triggered by scintillators[1] have been in coincidence with SD. The reconstructions of SD and Radio Detector arrival directions have determined an angular resolution of the Radio Detector of about 6° at this early stage [46].
The energy threshold for AERA is expected to be $2 \cdot 10^{17}$ eV with 15 expected events per day. The array is fully efficient for cosmic rays with energies above 10^{19} eV [42]. It will be mounted at the AMIGA site (see below).

4.4 Further Extensions

The energy threshold of SD is $3 \cdot 10^{18}$ eV. FD encounters difficulties for primary energies beneath 10^{18} eV: The signal strength in fluorescence photons per unit path length is (at air shower maximum) roughly proportional to the primary energy, therefore the effective distance range of air shower detection gets smaller at lower energies. At these small distances the height of observation by the FD telescopes is limited. In addition, lower energy air showers reach their maximum of development at higher altitudes [47].
Since the Pierre Auger Collaboration has decided to go down to observable energies of about 10^{17} eV an adequate fluorescence telescope has to be able to look higher into the sky. Therefore *High Elevation Auger Telescopes* (HEAT) has been established. HEAT consists of three fluorescence telescopes similar to those of FD housed in buildings which themselves can be elevated by 30°. In this position the telescopes have a field of view of 30° to about 60° in elevation and 30° in azimuth. HEAT is located next to the FD building Coihueco to allow for example cross calibration and will start data taking in fall 2009.
The low energy extension for the SD will be *Auger Muons and Infill for the Ground Array* (AMIGA) [48]. It will consist of an *infill array* which means that the distances between two neighboring stations will be reduced by a factor two to 750 m over an area of 23.5 km^2. Inside this infill array will be another *infill-to-the-infill* array (cf. figure 4.6). In addition 30 m^2 of muon scintillator counters will be buried $\sim$ 3 m underground.
The AMIGA site lies beneath the location of Coihueco and HEAT in a distance of about six kilometers.

[1] Recently work on self trigger logics is in progress.

Regarding again the Radio Detector, the signal-to-noise ratio of radio pulses emitted by air showers is relatively low. The background noise in the 30 to 80 MHz band is predominantly given by the galactic noise, but also by transient and permanent man-made radio transmitters. Also interferences form other electronical devices may contribute to the background noise. In order to raise the signal-to-noise ratio, and therefore allow the rest of the Radio Detector's receiver system to distinguish between the radio pulse and the background noise, a reliable preamplifier is essential for the success of the experimental setup. The functional requirements of the amplifier are good and linear gain characteristics, low noise and low power consumption. These and further requirements will be discussed in more detail in section 6.1. In the corresponding chapter 6 the layout of the low-noise-preamplifier will be introduced. Chapter 7 will present and discuss the test of this design. But before the layout of the actual amplifier is going to be presented and discussed, the following chapter will give an introduction to high frequency preamplifier theory.

5. High Frequency Preamplifier Theory

Transistors are active semiconductor devices to amplify electrical signals. The demand on versatile applications led to a large variety of different types of transistors. Even very complex analog and digital integrated circuits (ICs) are built from several transistors with the surrounding networks. There are two types of transistors: *bipolar* and *unipolar*. The latter is also known as *field effect transistor*. Since this work uses only the bipolar type, only this one will be meant in the following using the expression *transistor*.
Most commonly transistors are made from silicon (group IV) or a combination of elements from groups III and V (e.g. GaAs). A npn-transistor is composed of a negatively doped *emitter* (n), a positively doped *base*(p) and a negatively doped *collector* (n). The following discussion will only explain this type since for a pnp-transistor simply the dopings and directions of currents and voltages have to be inverted.
The discussion on transistors is predominantly based upon [49].

5.1 Bipolar Transistor in an Emitter Circuit as Amplifier

A schematic view of a npn-transistor is given in figure 5.1. One might describe it as two diodes with the same layer in the middle, the base. Only with the adequate surrounding circuit a transistor will be able to operate as desired. This circuit determines the *operating* or *bias point* of the transistor. Therefore a small direct current is passed to the base superpositioning with the signal which is meant to be amplified. The base-emitter diode is forward-biased and becomes conductive for base-emitter voltages $U_{\mathrm{BE}} \geq 0.5$ V. The base current I_{B} is dependent on U_{BE} and the junction temperature ϑ_{j}. This current takes charge carriers into the backward operated base-collector diode which thus becomes conductive. This leads to a much larger collector current I_{C} which only depends little on the collector-emitter voltage U_{CE} as can be seen in figure 5.2. I_{C} flows via the base to the emitter. This is the basic principle of all bipolar transistors.

We will consider the transistor as a two port (cf. figure 5.3 a)). The input resistance R_{e} of a transistor in an emitter circuit (i.e. the input and the output circuit

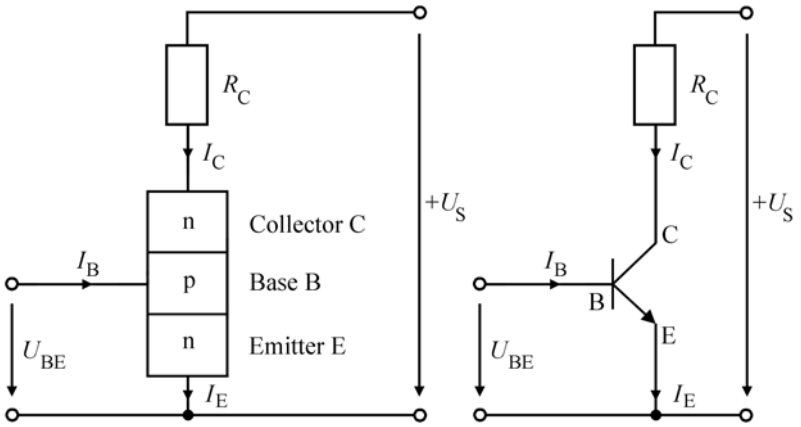

Figure 5.1: Schematic of a transistor in an emitter circuit. Left shown with the two np-junctions, right with the graphical symbol.

are both connected to the emitter) acts as the resistance of the base-emitter junction r_{BE}. The base current I_{B} is given by

$$I_{\mathrm{B}} = I_0 \left(\exp\left(\frac{U_{\mathrm{BE}}}{U_T} - 1 \right) \right) \quad \text{with} \quad I_{\mathrm{B}} \approx I_0 \exp\left(\frac{U_{\mathrm{BE}}}{U_T} \right), \tag{5.1}$$

if the base-emitter diode is forward-biased. Herein I_0 is the transistor type dependent reverse saturation current (e.g. 0.1 nA for a silicon small signal transistor at 25° C) and the *temperature voltage* $U_T = k_{\mathrm{B}} T / e_0$. k_{B} is the Boltzmann constant and e_0 is the elementary charge. At 25° C U_T is about 26 mV. The non-linear dependency of the base current on the base-emitter voltage U_{BE} leads to undesired behavior in most applications. Therefore the strongly non-linear input resistance has to be equaled by an appropriate circuit and the transistor is controlled by I_{B} instead of a voltage. The input conductance $g_{\mathrm{BE}} = 1/r_{\mathrm{BE}}$ is determined by

$$\frac{1}{r_{\mathrm{BE}}} = \frac{\mathrm{d}I_{\mathrm{B}}}{\mathrm{d}U_{\mathrm{BE}}} = \frac{I_0 \cdot \exp\left(U_{\mathrm{BE}}/U_T\right)}{U_T} \tag{5.2}$$

Using equation (5.1) it follows

$$r_{\mathrm{BE}} = \frac{U_T}{I_{\mathrm{B}}}\,. \tag{5.3}$$

Please note that U_T is dependent on the temperature. The equivalent circuit of the transistor in an emitter circuit in figure 5.3 b) shows the input resistance as the base-emitter resistance r_{BE}.

The high collector current and the low base current by which the first one is controlled form together the emitter current I_{C}. The relation between I_{C} and I_{B} is mainly linear (cf. figure 5.4). Therefore in the safe operating area of the transistor (i.e. the parameter space of U_{CE} and I_{C} wherein the transistor can be operated without taking damage, cf. figure 5.1) the *direct current gain* B is constant and expressed by

$$B = \frac{I_{\mathrm{C}}}{I_{\mathrm{B}}}\,. \tag{5.4}$$

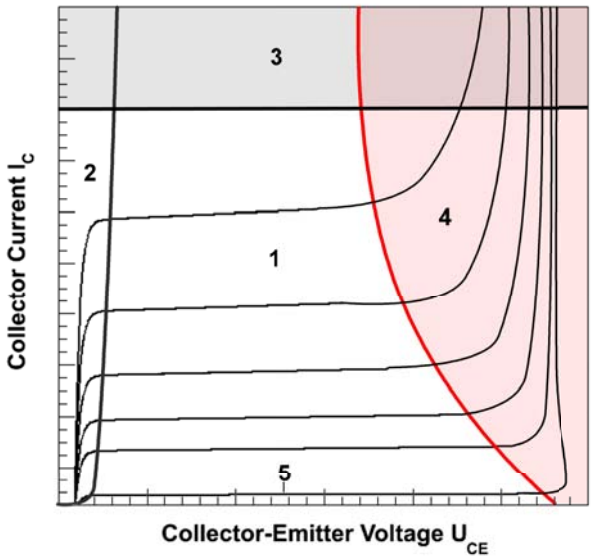

Figure 5.2: The collector current depending on the collector emitter voltage of the transistor shown in figure 5.1 and the resulting operating areas. 1 shows the *safe operating area*, 2 the saturation region. The curve separating 1 from 2 is for a collector-base voltage $U_{\mathrm{CB}} = 0$. The line beneath 3 indicates the maximum rating of the collector current. The red line indicates the maximum power dissipation. In region 4 the collector-base junction breaks down. Operating the transistor in region 3 or 4 will permanently destroy it. If the base current $I_{\mathrm{B}} = 0$, the transistor blocks and only the reverse-blocking current 5 will appear.

For higher differences in I_{C} the *differential current gain* β is used:

$$\beta = \frac{\Delta I_{\mathrm{C}}}{\Delta I_{\mathrm{B}}}\,. \tag{5.5}$$

Furthermore there is a relation between β and the signal frequency f. For direct currents and low frequencies β is constant: $\beta = \beta_0$. For higher frequencies it decreases. The frequency at which the differential gain becomes 1 is called *transit frequency* f_{T}. Figure 5.6 illustrates the dependency of β on the frequency. Here it can be seen that at the *barrier frequency* f_{g} the current gain falls down to $\beta = \beta_0/\sqrt{2}$. On the one hand there are these systematic dependencies of the current gain. On the other hand there is a broad scattering in this parameter due to the manufacturing process. Most manufactures sort the transistors into different current gain groups and modern procedures of manufacturing lead to more and more narrow tolerances. Nevertheless, the circuit designer has to stabilize the operating point of the transistor. This is done by *generative feedback* and will be explained below.

So far the transistor was treated as a current source controlled by the base current. The source's current evokes the desired output voltage at the load resistance R_{C}. Through the collector-base resistance r_{r} flows a small current into the base, depending on the collector-base voltage U_{CB}. This current appears amplified by the

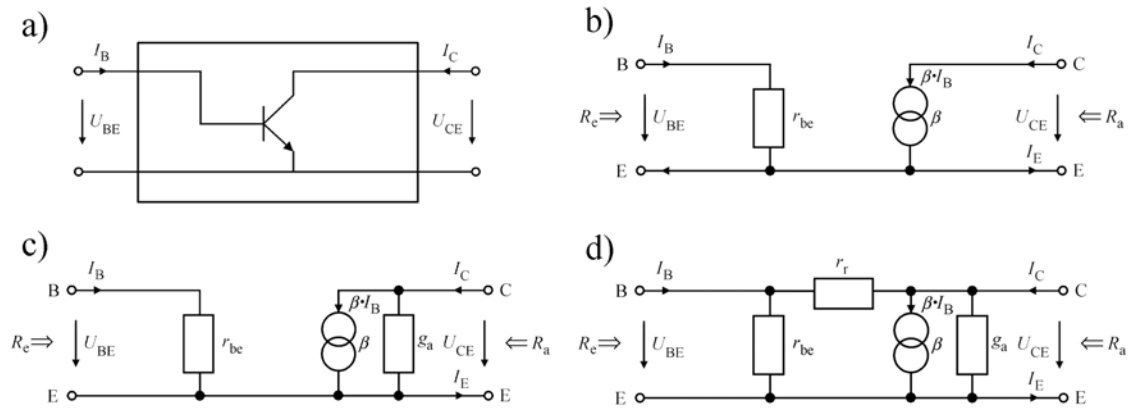

Figure 5.3: a) The transistor as a two-port. b) to d) Equivalent circuits of the transistor regarding it as a current source controlled by the base current. See text for details.

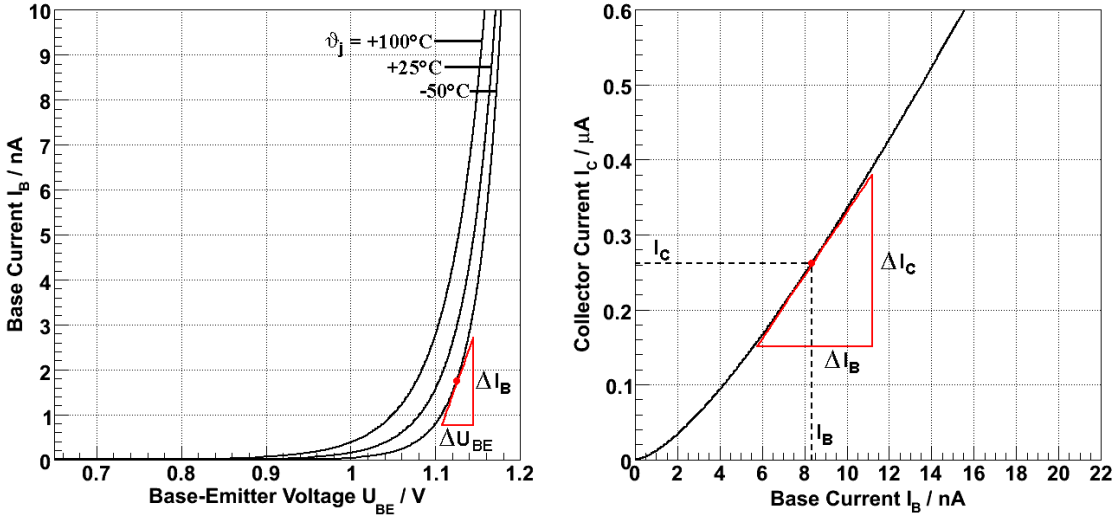

Figure 5.4: Left: Input characteristics of a transistor for different junction temperatures ϑ_j. From the slope triangle the input resistance r_{be} is determined. Right: Current gain characteristic of a transistor. From the slope triangle the differential current gain β is determined.

factor β in the collector-emitter-junction. In the equivalent circuit from figure 5.3 this current is due to the conductance $g_a = 1/r_a$ which is parallel to the collector-emitter-junction. It is given by

$$g_a = \frac{\Delta I_C}{\Delta U_{CE}} \tag{5.6}$$

Exact consideration show that the collector-base voltage U_{CB} has influence on the base-emitter voltage U_{BE} and the base current I_B (cf. figure 5.5). Since the high

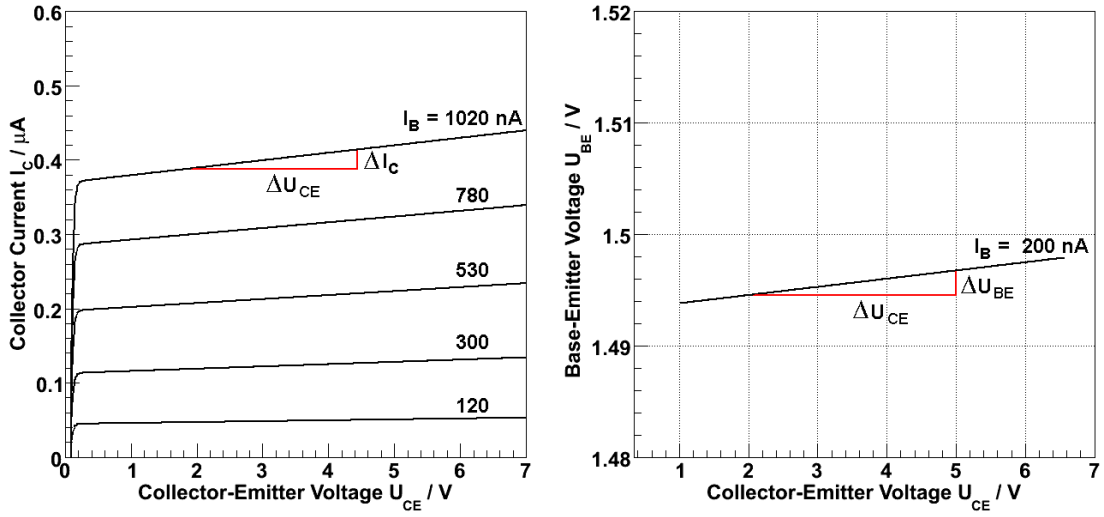

Figure 5.5: Left: Output characteristics of a transistor for different base currents I_B. From the slope triangle the output conductance g_a is determined. Right: The base-emitter voltage of a transistor depending on its collector-emitter voltage. From the slope triangle the internal feedback D is determined.

collector-base resistance r_r and the low base-emitter resistance r_{BE} form a potential divider the collector voltage has only little *feedback*. It is defined as

$$D = \frac{\Delta U_{BE}}{\Delta U_{CE}} . \tag{5.7}$$

For small signal transistors D is in the order of magnitude of 10^{-4} and is generally negligible.
The parameters of the transistor input resistance r_{be}, current gain β, output conductance g_a and voltage feedback D are real for direct currents and low frequencies. With higher frequencies the capacities of the transistor junctions become more and more notable and effect the parameters. In this case the parameters become complex.

Further parameters of a transistor are leaking currents, i.e. currents that appear even if the base current I_B is absent, and its intrinsic noise. In section 5.4 the noise will be discussed in detail. To those parameters a circuit designer has to know to assemble reliable devices, the manufactures give maximum ratings for their transistors. These maximum ratings should be taken serious since operating a transistor beyond their borders might destroy it. They are: maximum reverse voltage for each pair of electrodes, maximum currents, maximum junction temperatures and maximum total power dissipation. From these ratings the *safe operating area* of a transistor can be determined, i.e. the area in which the device can be operated without taking any damage (cf. figure 5.1).

The characteristics of a transistor shown in figures 5.4 and 5.5 can be arranged together to illustrate how an input signal evokes the output signal. This is done in

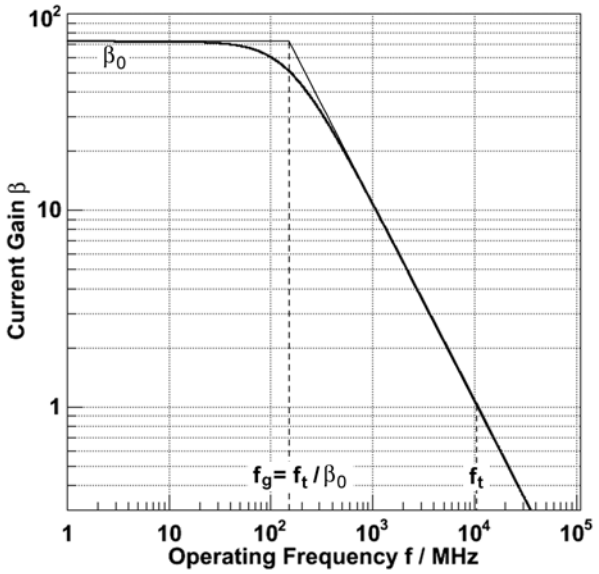

Figure 5.6: The current gain of a transistor as function of the frequency. The frequency at which the current gain is decreased to 1 is called *transit frequency*. f_g is the *barrier frequency*.

figure 5.7. Starting in the third quadrant a time dependent input signal, i.e. the base-emitter voltage $U_{BE}(t)$, leads to the base current $I_B(t)$. The current gets amplified resulting in the collector current $I_C(t)$. The collector current evokes the output voltage $U_{CE}(t)$.
In the first quadrant of figure 5.7 the load resistance R_C appears as a *load line*. It can be determined by finding the two points where it crosses the axes: If the transistor is locking (i.e. $I_C = 0$) the total voltage U_S (in this example 5 V) falls off at the collector-emitter junction. If the transistor is connected trough, the resistance of the collector-emitter junction is zero and thus U_{CE} is zero as well. The total voltage U_S will therefore fall off at the load resistance R_C. The current will be $I_C = U_S/R_C = 5\ \text{V}/10\ \text{M}\Omega = 0.5\mu\text{A}$.

The gain in the emitter circuit is relatively high compared to the other basic circuits of transistors, the collector and base circuit[1]. But the output signal is not just the amplified and inverted input signal but also distorted. This is due to the non-linear input characteristic. In this context section 5.2 will focus on linear and non-linear amplifiers.
For small signal, i.e. the input characteristic in the signal's region can be considered as linear, the *voltage gain* is

$$v_u = \frac{dU_a}{dU_e}\,. \tag{5.8}$$

[1]The transistor circuit is always named by the electrode to which the input and the output circuit are connected.

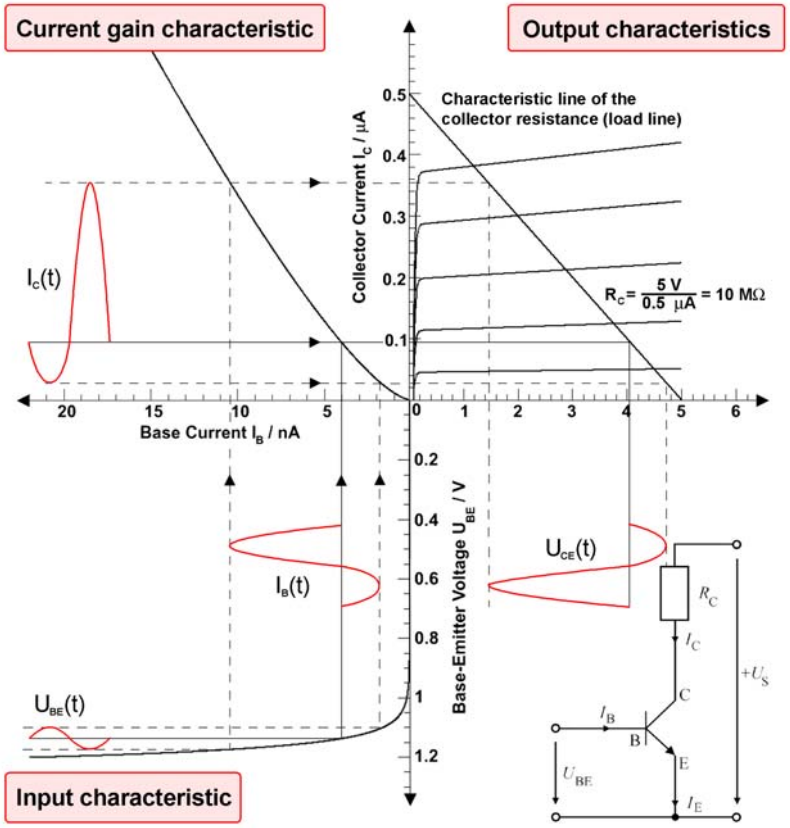

Figure 5.7: Voltages and currents of a transistor in emitter circuit as shown in the lower right corner. See text for details.

$U_e = U_{BE=} + I_B \cdot r_{BE}$ is the input voltage and $U_a = U_S - I_C \cdot R_C = U_S - \beta \cdot I_B \cdot R_C$ is the output voltage. $U_{BE=}$ is the mean base-emitter direct voltage. For the differential follows $dU_e = dI_B \cdot r_{BE}$ and $dU_a = -dI_B \cdot \beta \cdot R_C$. Replacing this in equation (5.8) the voltage gain can be expressed as

$$v_u = \frac{-\beta \cdot R_C}{r_{BE}} . \tag{5.9}$$

Choice and Stabilization of the Bias Point

The transistor will only operate as desired if the surrounding circuit on the one hand delivers the needed voltages and currents and on the other hand allows the signal to evolve as desired. The left side of figure 5.8 shows a transistor in emitter circuit with the different junctions getting their bias voltages from the direct voltage U_S which is then appropriately divided by the potential divider consisting of the resistances R_C and R_D. The bias point is adjusted by the base direct voltage in a way that the transistor always operates in the linear region. This means that the voltage U_{RC} which drops down at the resistance R_C should not be below 1 V and the voltage fall-off at the transistor U_{CE} should not be below 1.5 V. The load line appears at the output characteristics as a straight line from the upper left to the lower right as

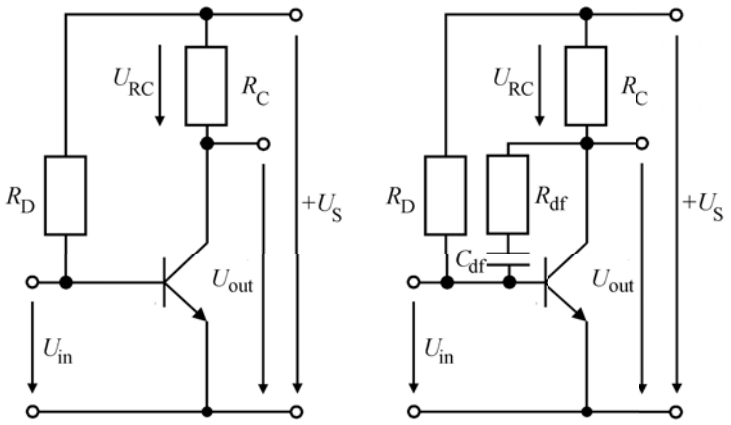

Figure 5.8: Left: The transistor gets its bias voltages from the direct voltage U_S and the potential divider consisting of R_C and R_D. Right: Degenerative voltage feedback. The output signal is partly fed back towards the input using the resistance R_{df}. The capacitance C_{df} may be used to block direct voltages.

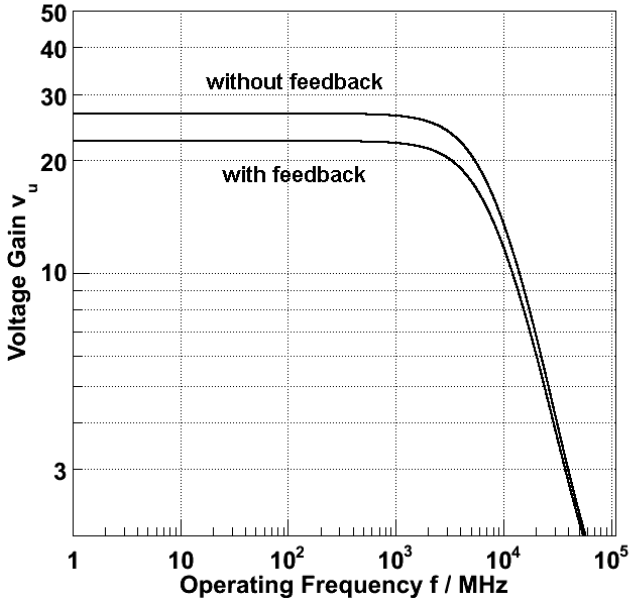

Figure 5.9: The voltage gain of the two circuits shown in figure 5.8.

discussed above. It allows to determine U_{RC} and U_{CE} for any collector current I_C. Since the collector current is dependent on the junction temperature the bias point has to be stabilized. It can be achieved by returning a part of the output signal back to the input circuit. This is done by the resistance R_{df} in figure 5.8 and is called *degenerated voltage feedback*. The returned signal is 180° phase shifted to the input signal so that stabilization is achieved on cost of the gain (cf. figure 5.9). If the temperature in the transistor raises the collector current raises as well. This leads to a decrease of the collector-emitter voltage since the voltage dropdown at

the resistance R_C increases with the collector current. The base current is partly obtained from the lines with the resistances R_D and R_{df}. It gets reduced with the decrease of the collector-emitter voltage. This again leads a reduction of the collector current and therefore the junction temperature declines. This counters the increase in temperature which was the starting point of the discussion, hence the bias point is stabilized.
With stabilizing the bias point the used region of the characteristics is reduced which leads to a smaller distortion of the output signal since the used region appears more linear. The base current and the base-emitter voltage change simultaneously therefore the voltage feedback counters manufacturing tolerances as well. To avoid degenerated direct voltage feedback the capacitance C_{df} may be used.

As already mentioned, the behavior of the transistor circuit is different for high frequencies. The junction capacities are not longer negligible. Furthermore, additional *parasitic inductances* and *capacitances* occur from the different parts of the circuit (e.g. even certain resistances show frequency dependencies above a certain frequency threshold) and from the transmission lines. The input and output resistances as well as the gain and voltage feedback D become complex values. Therefore most commonly high frequencies devices are characterized by *scattering* or *s-parameters*. They will be discussed in detail in section 5.3.

5.2 Linear and Non-Linear Amplifiers

In reality the characteristics of an amplifier are not linear. This deviation from linearity leads to distorted output signals. Any output signal U_a can be described by a series expansion of the input signal U_e:

$$U_a(t) = c_0 + c_1 \cdot U_e(t) + c_2 \cdot U_e^2(t) + c_3 \cdot U_e^3(t) + \cdots + c_n \cdot U_e^n(t)\,, \quad n \in \mathbb{N}\,. \tag{5.10}$$

c_0 up to c_n are the appropriate expansion coefficients. The addends describe the constant term, the linear term, the quadratic term, the term of third order and so on. The constant term in the output signal can be avoided by a high pass. Except from the desired linear term in case of an amplifier the other terms lead to undesired signals depending on the input signal.
If the amplifier is controlled by a single signal of the form $U_e(t) = \hat{U}_e \cos(\omega_e \cdot t)$ with amplitude $\hat{U}_e$ and frequency ω_e the terms in equation (5.10) of order ≥ 2 lead to harmonics, these are signals at integer multiples of the input frequency:

$$\begin{aligned} f_{\text{new}}^{\text{harm}} &= z \cdot f_e \\ \text{with} \quad z &= 2, 3, \cdots, n \quad \text{and} \quad f_e = \omega_e / 2\pi\,. \end{aligned} \tag{5.11}$$

A quantity for this behavior is the *total harmonic distortion*. It is defined as the sum over the power of the harmonics divided by the power of the input signal[2]:

$$THD = \frac{P_1 + P_2 + P_3 + \cdots + P_n}{P_1} = \frac{V_1^2 + V_2^2 + V_3^2 + \cdots + V_n^2}{V_1^2}\,, \tag{5.12}$$

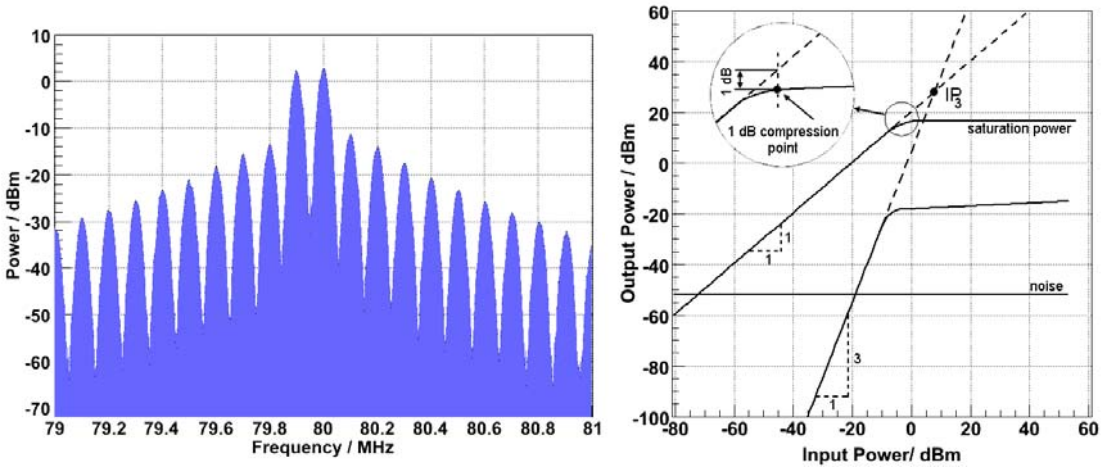

Figure 5.10: Left: The output power spectrum of a transistor with the wanted signals at 80.0 MHz and 79.9 MHz as measured with a spectrum analyzer. The other peaks are intermodulation products and distort the output signal. Right: Output power of intermodulation products of an amplifier versus its input power to illustrate the 1 dB compression point, the third order intermodulation point IP_3 and the dynamic range. The curve to the left comes from the single-tone method, the one to the right from the two-tone method (see text).

with V_i being the effective voltages of the output respective input signal. In high frequency applications another quantity is more common, this is the *1 dB compression point*[3]. It is the point in a output power versus input power diagram at which the curve is 1 dB below the extrapolated line of the linear part of the curve. It is demonstrated in figure 5.10 on the right side and can be referred to as *input* or *output 1dB compression point*.
If the amplifier is controlled by two signals of the form above they superposition to the input signal $U_e(t) = \hat{U}_{e1}\cos(\omega_{e1}\cdot t) + \hat{U}_{e2}\cos(\omega_{e2}\cdot t)$. The different frequencies mix together by the terms of order ≥ 2 in equation (5.10) to new frequencies

$$\begin{aligned} f_{\text{new}}^{\text{intermod}} &= |v\cdot f_{e1} \pm w\cdot f_{e2}| \\ \text{with} \quad v,w &= 0,1,2,3,\cdots,n \quad \text{and} \quad v+w \leq n\,. \end{aligned} \tag{5.13}$$

This is called *intermodulation* and illustrated at the left side of figure 5.10. An ideal mixer should only have a quadratical characteristic in order to mix different frequencies together, whereas an ideal amplifier should only have a linear characteristic. For *selective amplifiers*, i.e. amplifiers with a narrow bandwidth, the intermodulation products of odd orders are of special interest since they lie close to frequencies of the input signal. The amplitudes of the intermodulation products

[2]Other definitions may be used. Some authors define the total harmonic distortion as an amplitude ratio rather than a power ratio: $THD = \sqrt{V_1^2+V_2^2+V_3^2+\cdots+V_n^2}/V_1$.

[3]Since dealing with amplifiers leads to the description of very low and very high signals at the same time it is common to use the dB scale. A value P_1/P_2 is given in dB by $x = 10\log_{10}(P_1/P_2)$ dB. Powers are given in dBm, i.e. ten times the logarithm of the power compared to 1 mW: $P_{\text{dBm}} = 10\log_{10}(P_{\text{Watt}}/1\text{mW})$ dBm.

get lower with an increase of the order so that typically the third order intermodulation products are considered. In figure 5.10 the output power of an amplifier is plotted versus the input power. For the curve of the third order intermodulation products the amplifier is controlled with two signals of the same amplitude ($\hat{U}_{e1} = \hat{U}_{e2} = \hat{U}_e$). Replacing the input signal in equation (5.10) by the according two-tone signal $U_e(t) = \hat{U}_e(\cos(\omega_{e1} \cdot t) + \cos(\omega_{e2} \cdot t)$ one can show that the slope of the linear part of the curve describing intermodulation products of the order n has the slope n in a dB-diagram. Extrapolating the linear parts of the one-tone curve of the amplifier (with one signal) and the two-tone curve of the amplifier (with two signals) they cross each other in the *third order intercept point* IP_3. As for the 1 dB compression point the IP_3 is given as *input* or *output third order intercept point*. Analogously the intercept point of further orders can be determined. The intercept points can only be determined theoretically since the amplifier is already saturated at these powers.
Figure 5.10 shows also the output noise of the amplifier. Noise will be discussed in section 5.4. All together the curves allow to determine the *dynamic range* of the amplifier. It starts at the power where the wanted signal becomes higher than the noise. Otherwise one cannot distinguish between the noise and the signal. The dynamic range is limited to a power where whether the 1 dB compression point is achieved or the power of intermodulation products becomes higher than the noise. In the dynamic range the amplifier can be operated with nearly no distortion.

5.3 Transmission Line Theory

The purpose of a transmission line is to deliver the power fed into it by the internal resistance of a generator to a load resistance. The following discussion is orientated at [50]. Any transmission line consists of inductance per unit length L' and capacitance per unit length C'. Furthermore, real transmission lines also imply resistance per unit length R' and conductance per unit length G' which lead to losses of signal. A segment of length Δz of a transmission line is shown in figure 5.11. At the left side a complex voltage $U(z)$ and a complex current $I(z)$ are fed into the transmission line. At the right side voltage and current have changed to

$$\begin{aligned} U(z + \Delta z) &= U(z) - \Delta U \\ I(z + \Delta z) &= I(z) - \Delta I\,. \end{aligned} \tag{5.14}$$

Regarding figure 5.11 it can be written

$$\begin{aligned} \Delta U &= (R'\Delta z + i\omega L'\Delta z) \cdot I(z + \Delta z) \\ \Delta I &= (G'\Delta z + i\omega C'\Delta z) \cdot U(z) \end{aligned} \tag{5.15}$$

with the imaginary number i and the frequency of voltage and current $\omega = 2\pi f$. By $\Delta z \to 0$ the coupled differential equations

$$\begin{aligned} -\frac{\mathrm{d}U(z)}{\mathrm{d}z} &= (R' + i\omega L') \cdot I(z) \\ -\frac{\mathrm{d}I(z)}{\mathrm{d}z} &= (G' + i\omega C') \cdot U(z) \end{aligned} \tag{5.16}$$

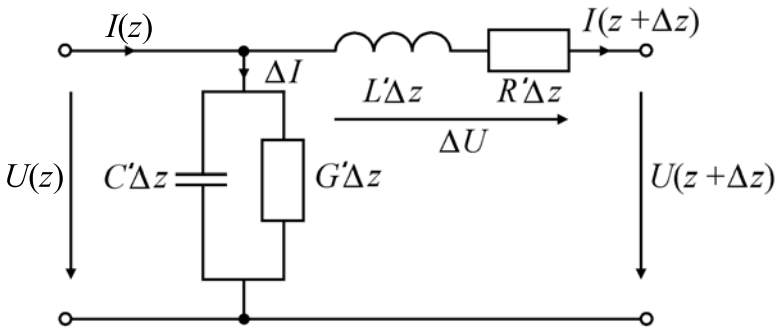

Figure 5.11: Schematic view of a transmission line of the length Δz. The primed values are values per unit length. The cross-flow and voltage drop lead to different voltages and currents at the end of the transmission line.

are obtained. A further differentiation of $\mathrm{d}U(z)/\mathrm{d}z$ with respect to z and replacing $\mathrm{d}I(z)/\mathrm{d}z$ according to equation (5.16) leads to the homogeneous differential equation

$$\frac{\mathrm{d}^2U(z)}{\mathrm{d}z^2} - (R' - i\omega L')\,(G' + i\omega C')\,U(z) = 0\,. \tag{5.17}$$

A general solution to this is

$$U(z) = U_{\mathrm{fw}}e^{-\gamma z} + U_{\mathrm{rev}}e^{+\gamma z} \quad \text{with} \quad \gamma = \sqrt{(R' + i\omega L')\,(G' + i\omega C')} \tag{5.18}$$

The solution is identified as superposition of two voltage waves propagating into opposite directions with the complex amplitudes U_{fw} and U_{rev} and the *propagation* or *transmission loss* γ. In general $\gamma = \alpha + i\beta$ is complex. α is called *attenuation constant* and β is called *phase constant*. For a lossless transmission line ($R' = 0$, $G' = 0$) α vanishes. In this case the amplitudes of the voltage stay constant, their phase rotates with $\pm\beta z$. For lossy transmission lines the amplitudes decrease exponentially according to $e^{-\alpha z}$. For lossless lines the solutions of the differential equations (5.16) are

$$\begin{aligned} U(z) &= U_{\mathrm{fw}}e^{-i\beta z} + U_{\mathrm{rev}}e^{+i\beta z} \\ I(z) &= I_{\mathrm{fw}}e^{-i\beta z} - I_{\mathrm{rev}}e^{+i\beta z}\,. \end{aligned} \tag{5.19}$$

The amplitudes of the waves of voltage superimpose rectified, the ones of the waves of current oppositely.

From equation 5.16 follows

$$I(z) = -\frac{1}{R' + i\omega L'}\frac{\mathrm{d}U}{\mathrm{d}z}\,. \tag{5.20}$$

According to equation (5.18) the local variation of the voltage is

$$\frac{\mathrm{d}U}{\mathrm{d}z} = -\gamma U_{\mathrm{fw}}e^{-\gamma z} + \gamma U_{\mathrm{rev}}e^{\gamma z} \tag{5.21}$$

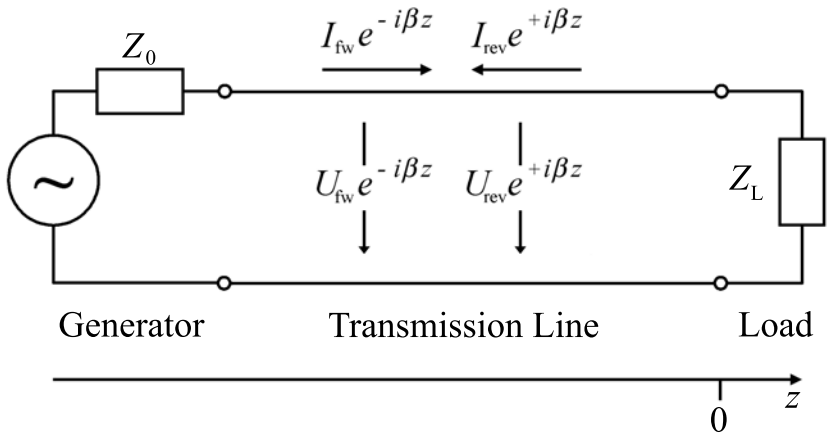

Figure 5.12: A generator feeds signals over its internal resistance Z_0 into a transmission line which is terminated by the load Z_L. Shown are the forward and reverse currents and voltages on the transmission line.

Together a relation between the voltage and the current is obtained:

$$\begin{aligned} I(z) &= \frac{\gamma}{R' + i\omega L'} \left(U_{fw} e^{-\gamma z} - U_{rev} e^{\gamma z} \right) \\ &= \frac{1}{Z_{TL}} U(z) \end{aligned} \tag{5.22}$$

The factor Z_{TL} must have the unit of a resistance and is therefore called *wave resistance*. Since

$$Z_{TL} = \frac{R' + i\omega L'}{\gamma} = \sqrt{\frac{R' + i\omega L'}{G' + i\omega C'}} \tag{5.23}$$

the wave resistance is assigned by the geometrical configuration of the transmission line. The use of the wave resistance requires a reasonable definition of voltages and currents. This is obtained by regarding them as consequences of the electric and magnetic field propagating through the transmission line. In general the wave resistance of a certain transmission line results therefore from a discussion of the field structure. For lossless transmission lines the wave resistance becomes real and is independent on the frequency:

$$Z_{TL} = \sqrt{\frac{L'}{C'}} \,. \tag{5.24}$$

A quantity to describe the relation between the incident and the reflected wave is the *reflection factor* $r(z)$. It is defined as the complex amplitude of the reflected wave divided by the complex amplitude of the incident wave:

$$r(z) = \frac{U_{rev} \cdot e^{+\gamma z}}{U_{fw} \cdot e^{-\gamma z}} \,. \tag{5.25}$$

Without loss of generality we consider the point $z = 0$ in figure 5.12. Here the reflection factor is $r_2 = U_{rev}/U_{fw}$. At the load Z_L according to Ohm's law $U_L = Z_L \cdot I_L$

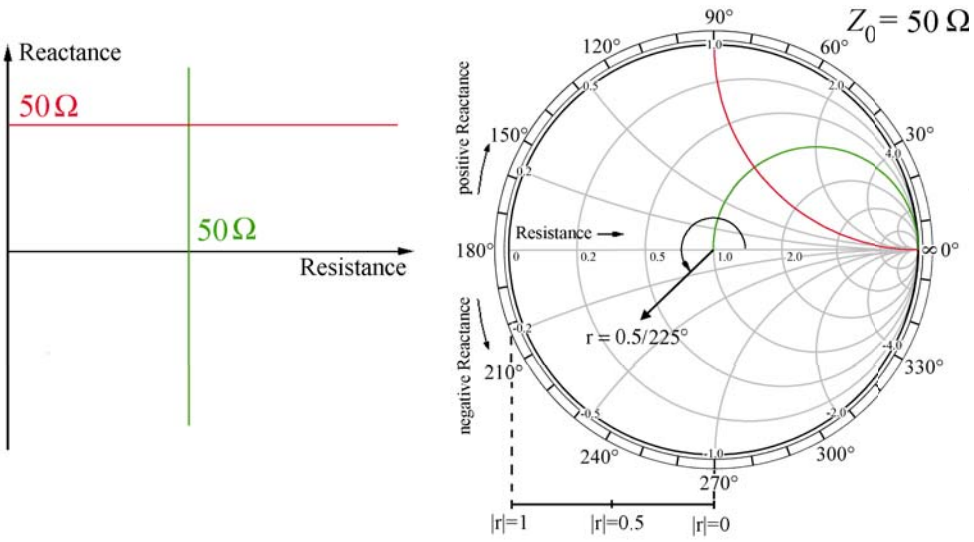

Figure 5.13: The Smith chart (right) derived from the right half of the perpendicular complex plane (left) with the conformal mapping given by equation (5.27). The axes of the complex plane are elongated to infinity where they finally meet. This is the point to the right end in the Smith chart. Generally Smith charts are normalized to the system impedance Z_0. Each circle with its center on the axis of resistance are points of constant resistance. Each line from the outer circle to infinity are points of constant reactance. A reflection coefficient r with the absolute value 0.5 and phase of 225° is plotted.

with the voltage at the load $U_\mathrm{L} = U(0) = U_\mathrm{fw} + U_\mathrm{rev}$ and the current at the load $I_\mathrm{L} = I(0) = I_\mathrm{fw} - I_\mathrm{rev}$. With the relation $U(z) = Z_\mathrm{TL} \cdot I(z)$ the load can be expressed by

$$Z_\mathrm{L} = Z_\mathrm{TL} \frac{U_\mathrm{fw} + U_\mathrm{rev}}{U_\mathrm{fw} - U_\mathrm{rev}} = Z_\mathrm{TL} \frac{1 + U_\mathrm{rev}/U_\mathrm{fw}}{1 - U_\mathrm{rev}/U_\mathrm{fw}} = Z_\mathrm{TL} \frac{1 + r_2}{1 - r_2} \,. \tag{5.26}$$

This is equivalent to

$$r_2 = \frac{Z_\mathrm{L} - Z_\mathrm{TL}}{Z_\mathrm{L} + Z_\mathrm{TL}} \,. \tag{5.27}$$

From this equation it is obvious that there will be no reflection of the incident wave if the impedance of the the load is equal to the wave resistance. In this case the transmission line and the load are *matched* or *impedance matched* and the total power which is fed into the transmission line is passed to the load. Any *mismatched* combination of transmission line and load will lead to reflections. A total mismatch is achieved by an open ($Z_\mathrm{L} = \infty$) or a shortened ($Z_\mathrm{L} = 0$) transmission line. In both cases the incident wave will be totally reflected.

A *Smith chart* is an appropriate way to plot reflection factors. Mathematically it is derived by the conformal mapping expressed by equation (5.27) of the right half of the perpendicular imaginary plane (only here resistances are positive). Imagine the real and imaginary axes of the imaginary plane elongated to ∞. In this point the axes will meet. This is illustrated in figure 5.13. A Smith chart offers a variety

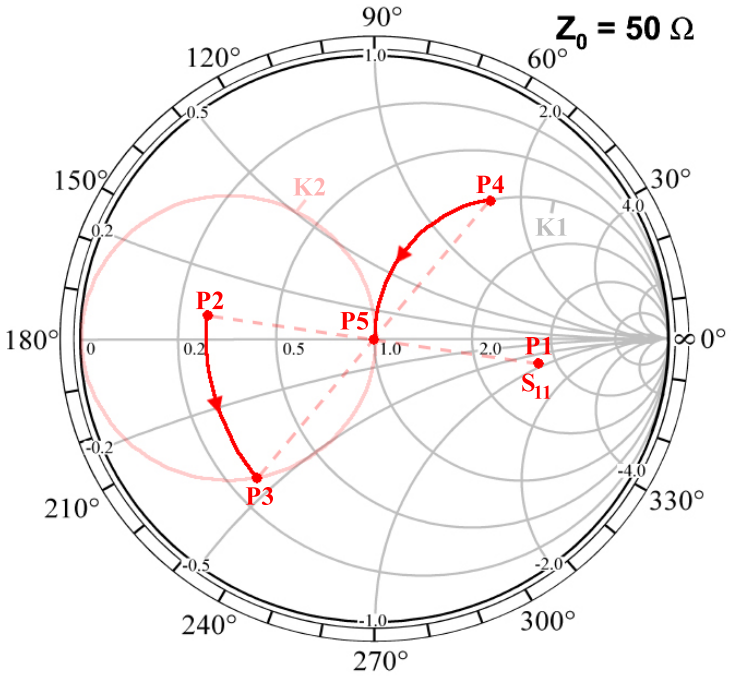

Figure 5.14: Selective impedance matching using the Smith chart. See text for details.

of advantages compared to the perpendicular imaginary plane. One advantage is that shortened transmission lines can easily be described since the Smith chart owns the point ∞. Another advantage is that a circuit designer can easily determine the parts needed to match a mismatched transmission line. This will be explained by a small example:
itive). Imagine the real and imaginary axes of the imaginary plane elongated to ∞. In this point the axes will meet. This is illustrated in figure 5.13. A Smith chart offers a variety of advantages compared to the perpendicular imaginary plane. One advantage is that shortened transmission lines can easily be described since the Smith chart owns the point ∞. Another advantage is that a circuit designer can easily determine the parts needed to match a mismatched transmission line. This will be explained by a small example:

The integrated circuit BGA420 shall be impedance matched at its input to 50 Ω for a frequency of $f = \omega/(2\pi) = 100$ MHz. From its datasheet (which can be found in the appendix A) the reflection factor at this frequency is taken[4]. Its absolute value is about 0.57 and its phase is -8.5°. This reflection factor is plotted into the Smith chart shown in figure 5.14 as point P1. It shows also the input impedance of the BGA420 at this certain frequency. The goal is to design a circuit which transforms the input impedance in a way that it will end up in the middle of the Smith chart

[4]In the datasheet the reflection factor is called S_{11}. The explanation for this is given in the next paragraph on scattering parameters.

where the reflection becomes zero.
Regarding equation (5.27) we can write

$$r(z) = \frac{z-1}{z+1} \qquad \text{with } z = \frac{Z_{\mathrm{L}}}{Z_{\mathrm{TL}}}\,. \tag{5.28}$$

Therefore

$$r(1/z) = r(y) = \frac{1/z-1}{1/z+1} = \frac{1-z}{1+z} = -r(z)\,. \tag{5.29}$$

This means that the corresponding admittance[5] y to a certain impedance z is achieved in the Smith chart by shifting the phase of r by 180°.
Since the first part we want to put in front of the BGA420's input terminal is a shunt inductance L we change from the impedance view to the admittance view of P1 by mirroring P1 at the center. By this the point P2 is achieved. The shunt inductance shall transform P2 to a point on the circle K2. From the Smith chart it can be seen that the distance from P2 to P3 is $i \cdot s_y = -i \cdot 0.515$. Since

$$-i\, s_y = \frac{50\,\Omega}{i\,\omega\, L} \tag{5.30}$$

the inductance should be $L = 154.6$ nH. Mirroring P3 at the center leads to P4. From P4 a series capacitance C transforms the impedance along the circle K1 to the center. The distance from P4 to the center is $i \cdot s_z = -i \cdot 1.62$. With

$$-i\, s_z = \frac{1}{i\,\omega\, C\, 50\,\Omega} \tag{5.31}$$

the capacitance is determined to $C = 19.6$ pF. With this impedance matching network consisting of the shunt inductance L and the series capacitance C (regarding from the chips input towards a generator) no reflection of signals coming from a 50 Ω waveguide system will occur at the BGA420's input at 100 MHz.

Scattering-Parameters

The discussion of matched and unmatched transmission lines can be adopted to any two-port[6]. A two-port will only pass the total power fed into it forward to the next two-port if both are matched. In case of mismatch the power will be partly reflected depending on the mismatch. For a match the output impedance of the first two-port has to be equal to the input impedance of the second two-port. Again reflection factors will occur.
Considering one two-port it is also of interest how the voltages propagate inside the two-port in forward and backward direction. Be a_1 respective a_2 the complex voltage towards port 1 respective port 2 and b_1 respective b_2 the complex voltage away from port 1 respective port 2 (cf. figure 5.15). These voltages are related among each other by the *scattering matrix*:

$$\begin{pmatrix} b_1 \\ b_2 \end{pmatrix} = \begin{pmatrix} S_{11} & S_{12} \\ S_{21} & S_{22} \end{pmatrix} \begin{pmatrix} a_1 \\ a_2 \end{pmatrix}\,. \tag{5.32}$$

[5] Impedance = resistance + reactance, admittance = conductance + suszeptance
[6] The transmission line can be described as two-port as well.

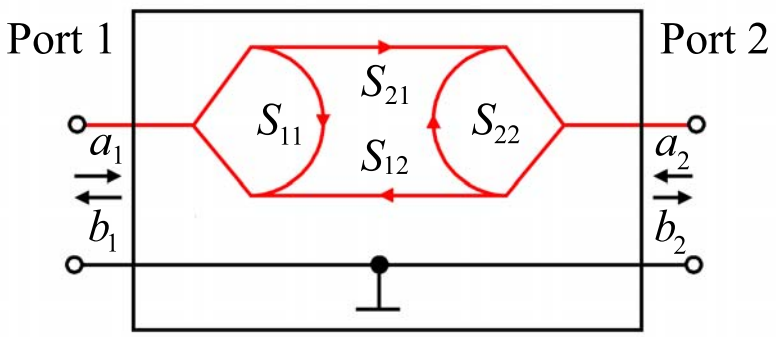

Figure 5.15: S-parameters at a two-port. a_1 and a_2 are voltages towards the two-port, b_1 and b_2 away from it. The s-parameters set these quantities into relations. They are the forward and backward transfer factors and input and output reflection factors.

The entries of this matrix are the complex, frequency dependent *scattering* or *s-parameters*

$$\begin{aligned}
S_{11} &= \left(\frac{b_1}{a_1}\right)_{a_2=0} && \text{reflection factor at port 1 or } \textit{input reflection factor}\,, \\
S_{21} &= \left(\frac{b_2}{a_1}\right)_{a_2=0} && \textit{forward transfer factor}\,, \\
S_{12} &= \left(\frac{b_1}{a_2}\right)_{a_1=0} && \textit{backward transfer factor}\,, \\
S_{22} &= \left(\frac{b_2}{a_2}\right)_{a_1=0} && \text{reflection factor at port 2 or } \textit{output reflection factor}\,.
\end{aligned} \tag{5.33}$$

They are also illustrated in figure 5.15. S-parameters can be measured by *vector network analyzers*. These devices fed a known signal into a two-port and measure amplitude and phase of the reflected signal (to determine S_{11} or S_{22}) or the transfered signal (to determine S_{21} or S_{12}). Note that the s-parameters of a two-port depend on the wave resistance of the transmission line and the source impedance of the internal signal generator of the device. In high-frequency applications cables and signal generators usually have an impedance[7] of 50 Ω so that in this case "the s-parameters are measured in a 50 Ω waveguide system". In these systems circuit designers aim for input and output impedances of their two-ports of 50 Ω to design matching circuits and devices.
As S_{11} and S_{22} are reflection factors it makes sense to display them in a Smith chart. For an amplifier S_{21} is the voltage gain.

[7]The expression *impedance* may be used as a synonym for *wave resistance*.

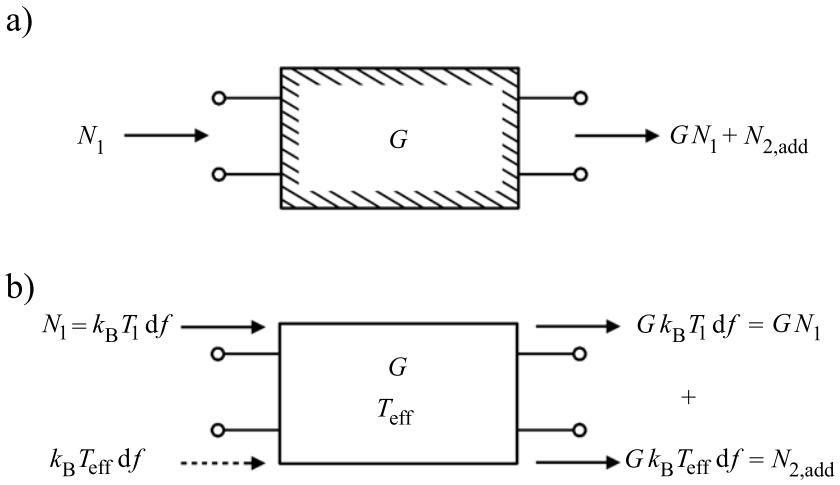

Figure 5.16: a) Noisy two-port with power gain G. b) Equivalent noiseless two-port with additional noise source at the input.

5.4 Noise

Noise denotes statistical processes or signals which processes can not be predicted and which do not contain information of use. This discussion is orientated at [49] and [50].
There are different types of noise:
Thermal noise are irregular movements of charge carriers in a conductor or semi-conductor due to its heat. The *noise power* is given by

$$P_{\mathrm{R}} = 4\, k_{\mathrm{B}}\, T\, \mathrm{d}f\,, \tag{5.34}$$

with the Boltzmann constant k_{B}, the Temperature T and the frequency bandwidth $\mathrm{d}f$. Note that the noise power is independent on the considered resistance R. If the *noise power density* $P_{\mathrm{R}}/\mathrm{d}f$ is constant in the frequency the noise is called *white noise*. The open circuit noise voltage of the resistance R is therefore

$$|\tilde{U}_{\mathrm{R}}| = \sqrt{4\, k_{\mathrm{B}}\, T\, R\, \mathrm{d}f}\,, \tag{5.35}$$

so that the available noise power which can be given to a resistance with equal value is

$$P_{\mathrm{RA}} = k_{\mathrm{B}}\, T\, \mathrm{d}f\,. \tag{5.36}$$

Shot noise occurs if a current flows over a potential barrier (like in a semi-conductor or electrons leaving a hot cathode). The quantization of charge and the statistical fluctuations of the moment a single charge carrier crosses the barrier leads to a noise current which fluctuates around the total current and is proportional to it. The noise depends on the internal resistance of the signal source R_{i}, the (junction) temperature ϑ_{j}, the frequency bandwidth $\mathrm{d}f$, the type of the transistor and its operating point.

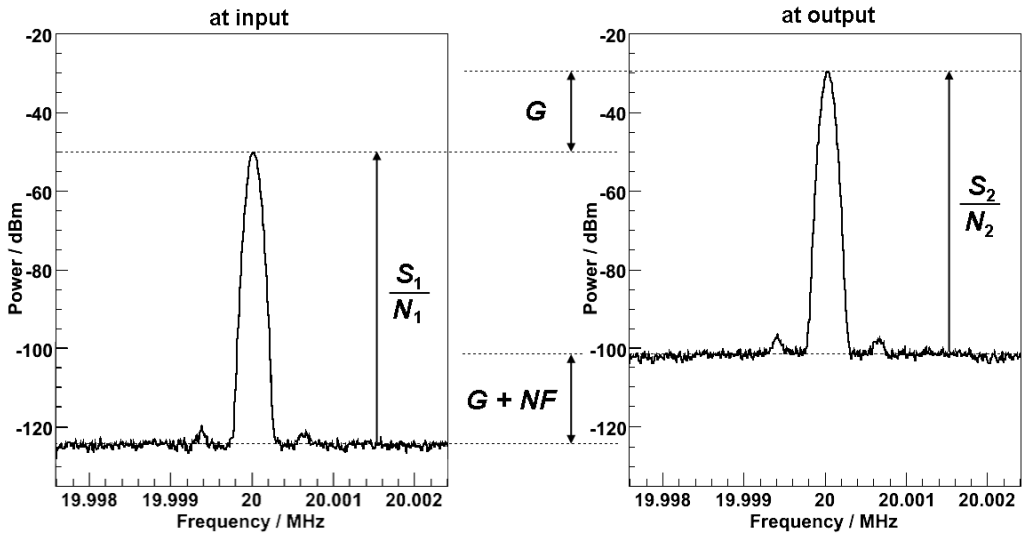

Figure 5.17: Signal-to-noise-ratio at the input and output of an amplifier as measured with a spectrum analyzer.

$1/f$*-noise* appears in tubes, semi-conductors and carbon resistances beneath frequencies of about 100 kHz. The spectral noise power density is about proportional to $1/f$. Such noises are also referred to as *pink noise*. Its cause is not yet sufficiently clear.
A further type of noise which noise power density is about proportional to $1/f$ is the *flicker noise* in vacuum tubes. It originates from statistical fluctuations of the work function on the surface of the cathode and can be observed through a microscope as flicker.

Figure 5.16 a) shows a noisy two-port with the noise power N_1 at the input and a power gain G. At the output the noise is the sum of the amplified input noise and the additional noise:

$$N_2 = G\,N_1 + N_{2,\mathrm{add}} = G\,k_\mathrm{B}\,T_1\,\mathrm{d}f + G\,k_\mathrm{B}\,T_\mathrm{eff}\,\mathrm{d}f = k_\mathrm{B}\,T_2\,\mathrm{d}f\,. \tag{5.37}$$

With this expression the two-port can be considered as noiseless with an additional noise source at the input generating the noise with the *effective noise temperature* T_eff (cf. figure 5.16 b)). T_eff is therefore a unique quantity to describe the noise characteristics of a two-port. The noise temperature at the output is

$$T_2 = G(T_1 + T_\mathrm{eff})\,. \tag{5.38}$$

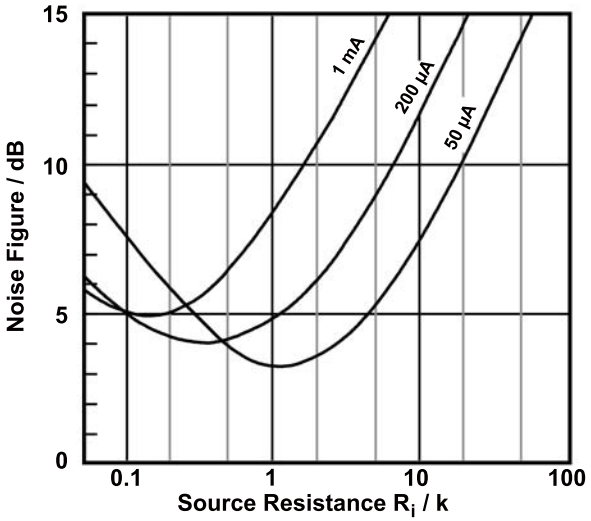

Figure 5.18: Noise figure as a function of the internal resistance of the signal source. The set of functions is for different collector currents. (Modified, original taken from [49].)

Another quantity to describe the noise characteristics of a two-port is the *noise factor* F. It is defined as the signal-to-noise-ratio (SNR) at the input divided by the SNR at the output

$$F = \frac{S_1/N_1}{S_2/N_2} \qquad \text{with}$$
$$S_1 : \text{input power of signal}$$
$$S_2 : \text{output power of signal} \tag{5.39}$$
$$N_1 : \text{input power of noise}$$
$$N_2 : \text{output power of noise}$$

and can be written as

$$F = \frac{N_2}{G\,N_1} = \frac{G\,N_1 + N_{2,\text{add}}}{G\,N_1} = 1 + \frac{N_{2,\text{add}}}{G\,N_1} = 1 + F_{\text{add}} \tag{5.40}$$

with the *additional noise factor* F_{add}. Furthermore

$$F = \frac{N_2}{G\,N_1} = \frac{G\,k_\text{B}\,T_1\,\text{d}f + G\,k_\text{B}\,T_\text{eff}\,\text{d}f}{G\,k_\text{B}\,T_1 \cdot \text{d}f} = 1 + \frac{T_\text{eff}}{T_1} \tag{5.41}$$

so that

$$F_{\text{add}} = \frac{T_\text{eff}}{T_1}\,. \tag{5.42}$$

The *noise figure* is defined as

$$NF = 10\,\log_{10}(F)\,\text{dB}\,. \tag{5.43}$$

Figure 5.17 shows a signal at the input of an amplifier with power gain G and noise figure NF and the corresponding signal at the output as measured with a spectrum

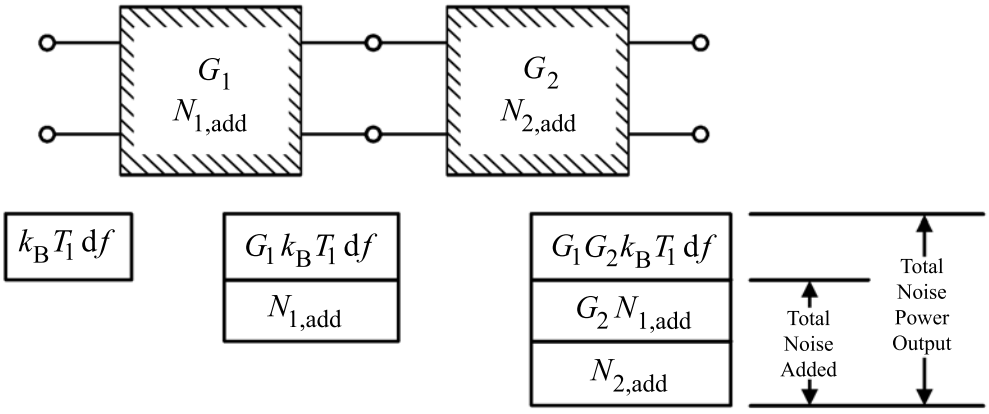

Figure 5.19: The effect of a second stage to the total noise power output. Stage 1 amplifies the input noise power by G_1 and adds $N_{1,\mathrm{add}}$. In the second stage both powers are amplified by G_2 and $N_{2,\mathrm{add}}$ is added. Since the powers are uncorrelated they may be added to the total noise power output.

analyzer.
A noise two-port might contain correlated noise sources so that the additional noise becomes a function of the internal resistance of the signal source. This is shown in figure 5.18. For any collector current it exists an internal resistance of the signal source where the noise figure has a minimum. Again for higher frequencies the impedance instead of the resistance has to be taken into account. The existence of the minimum allows the circuit designer to *noise match* his circuit. In general noise matching and impedance matching lead to different matching networks, hence a compromise between these two matching methods has to be considered.

Two cascaded amplifiers and the occurring noise in this amplifier chain are shown in figure 5.19. The input noise power $k_\mathrm{B} T_1 \mathrm{d}f$ is amplified by the gain of the first stage G_1. This stage adds the additional noise $N_{1,\mathrm{add}}$. These two powers are amplified by the gain G_2 of the second stage. Also $N_{2,\mathrm{add}}$ is added. Since the powers are uncorrelated they may be summed up to the total output power

$$N_\mathrm{out} = G_1\, G_2\, k_\mathrm{B}\, T_1\, \mathrm{d}f + G_2\, N_{1,\mathrm{add}} + N_{2,\mathrm{add}}\,. \tag{5.44}$$

With

$$N_{\mathrm{i,add}} = (F_i - 1) G_i\, k_\mathrm{B}\, T_1\, \mathrm{d}f \tag{5.45}$$

the output noise power can be written as

$$N_\mathrm{out} = G_1\, G_2\, k_\mathrm{B}\, T_1\, \mathrm{d}f \left(F_1 + \frac{F_2 - 1}{G_1} \right). \tag{5.46}$$

Thus the noise factor of the total system with total gain $G = G_1 G_2$ is

$$F_{\mathrm{sys},2} = F_1 + \frac{F_2 - 1}{G_1}\,. \tag{5.47}$$

The noise factor of a cascade with n stages can be found analogously as

$$F_{\mathrm{sys},n} = F_1 + \frac{F_2 - 1}{G_1} + \frac{F_3 - 1}{G_1 G_2} + \ldots + \frac{F_n - 1}{G_1 G_2 \ldots G_n} \,. \tag{5.48}$$

This equation is often called *cascade noise equation*. If the gain of the first stage G_1 is sufficiently high the total noise factor of the system is nearly given by the first stage.

6. Low Noise Amplifier Design

Designing a Low Noise Amplifier (LNA) typically starts by assessing functional requirements for the application. Afterwards candidate devices are selected from the vendors' specifications. An appropriate bias technique is then selected followed by the design of matching networks. Subsequently the board layout has to be planned and connectors have to be added.
In the following sections these steps will be described in detail. Furthermore a short introduction to the circuit simulation tool PSpice will be given.

6.1 Functional Requirements of the Low Noise Amplifier

In the design of a LNA for the Auger Radio Detector there are several common goals. First of all the frequency range should reach from 30 MHz to 80 MHz as discussed in section 4.3 since this is the range where radio pulses emitted from ultra-high-energy-cosmic-rays will be measured.
A reasonable gain with low dependency on the frequency in the frequency range and sufficient linearity is desirable. Concerning the cascade noise equation (5.48) a rough rule of thumb is that the power gain of the first amplifier stage should be $>$ 10 dB to provide a total system noise dominated by this first stage. But since the test setups of the Radio Detector have already been operated with LNAs of a power gain $\sim$ 20 dB this value is to be aimed at.
The used Black Spider antennas (BS) are designed with an output impedance of about 50 Ω and feed their signals into a 50 Ω waveguide system [44]. Therefore stable 50 Ω input and output impedances of the LNA should be realized.
A low noise figure (NF) of the LNA is desired. The NF of the BS in the frequency range is predominantly evoked by the galactic noise. It is given by $\mathrm{NF} = N \,/\, k_\mathrm{B}\, T_0\, \mathrm{d}f$ with the available noise power N, the Boltzmann constant k_B, the reference temperature T_0 taken as 290 K and the noise power bandwidth of the receiving system $\mathrm{d}f$ [51]. Figure 6.1 shows the NF of the BS measured at the southern site of the Pierre Auger Observatory at a single moment. The power spectral density $N/\mathrm{d}f$ has been measured with the Rohde & Schwarz FSH4 spectrum analyzer model .24. To determine upper and lower limits of the NF a long time measurement should have been performed. On the other hand the knowledge of the radio sources distribution within our galaxy, the characteristics of the BS and the information that the galactic center has been at about 246° of azimuth and 14° of elevation in local coordinates at the moment of the measurement, allow to determine these limits. But this would

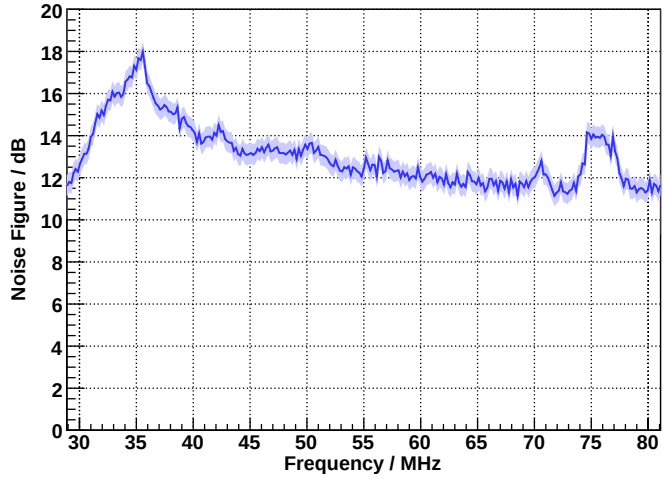

Figure 6.1: Noise Figure of the Black Spider antenna measured at the southern site of the Pierre Auger Observatory at May 1st, 2009, 16.50h. The band shows the systematic uncertainty of the measurement.

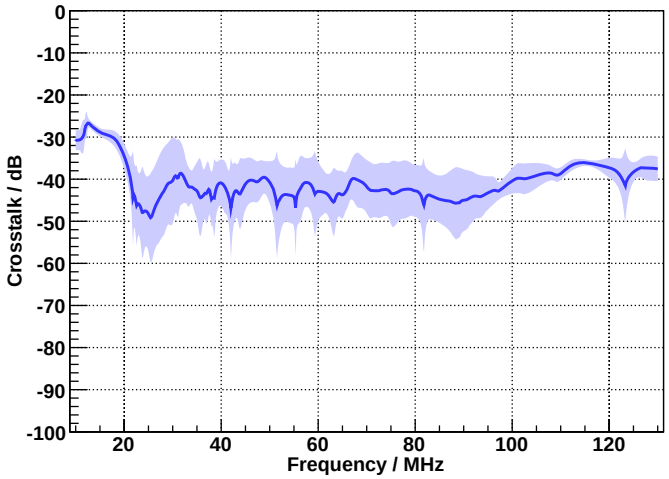

Figure 6.2: Mean crosstalk of a small production series of eight Black Spider antennas. The band shows the rms spread within the series.

exceed its use for this work since the measurement is only used to get a feeling for the noise at the input of the LNA. With a NF of the antenna between about 11.5 dB and 18 dB the matching priority should be for impedance matching instead of noise matching if the NF of the LNA is aimed at $\sim$ 2.5 dB.
The LNA should have a low power consumption since the power harvesting of the Radio Detector stations is done by solar panels.
Since the BS consists of two channels (one for the north-south and one for the east-west polarization) two LNAs will be mounted next to each other. These two LNA channels should not interfere with each other or at least the interference should be

lower than the interference of the two antenna channels. The mean crosstalk of a small production series of eight BS is shown in figure 6.2. To determine the crosstalk a known signal is fed into one channel while the power at the other channel is measured (i.e. a transmission measurement made with the spectrum analyzer FSH4; cf. section 7.1). The blue band in the plot shows the rms spread within the series. Between 30 MHz and 80 MHz the mean crosstalk is about -42 dB. The crosstalk of the two LNA channels should stay below this value.
Since the design of the overall electronics of a Radio Detector station are designed modular a bias voltage of the LNA of 5 V is desirable to operate it with the already installed DC/DC converter.
Due to ambient conditions the LNA must withstand high thermal fluctuations.
Furthermore low manufacturing costs are another design goal.

6.2 PSpice Simulation Software

Circuit designers take great advantage from simulation software allowing them to run various test routines before actually setting up the first prototype circuit for tests in the laboratory. A large amount of time and costs can be saved by taking simulations into the design process. SPICE (Simulation Program with Integrated Circuit Emphasis) is a mayor software to simulate analog, digital or mixed circuits. It was developed by the Electrical Engineering and Computer Sciences Faculty of the University of California, Berkeley. Several commercial and free software was developed on the basis of SPICE generally offering the user graphical user interfaces, plot routines for simulation results and large libraries of circuit devices. One of the most popular commercial software packages is PSpice from OrCAD, Inc.
The functionality of all SPICE programs is to numerically find approximate solutions for the differential equations which describe the considered circuit. These differential equations derive from the topology of the circuit which is given as a so called netlist to the simulator describing how the different parts are connected. Every single device in the netlist has its own model. This model might be orientated physically or also totally abstractly. In the latter case the device might be considered as a blackbox only described by equations relating its input to the output. The single components within this blackbox remain unknown. This decreases the time the simulator needs for its calculations and might result in more exact simulation results since uncertainties of the single components do not sum up.
The simulations done within this work are made with OrCAD PSpice 9.1 - Student Version. The student version offers the same possibilities as the full version. The only difference is that within the student version only 50 parts (thereof a maximum of ten transistors) may be taken into the simulation. The simulations are run at a bias voltage of 5 V and a temperature of 27° C if not otherwise specified.

6.3 Basic Circuit Layout

Large bandwidths in LNA designs are always an issue since many values of interest are depending on the frequency. The frequency range of 30 MHz to 80 MHz is relatively untypical for broadband LNAs. They become more common in the order of

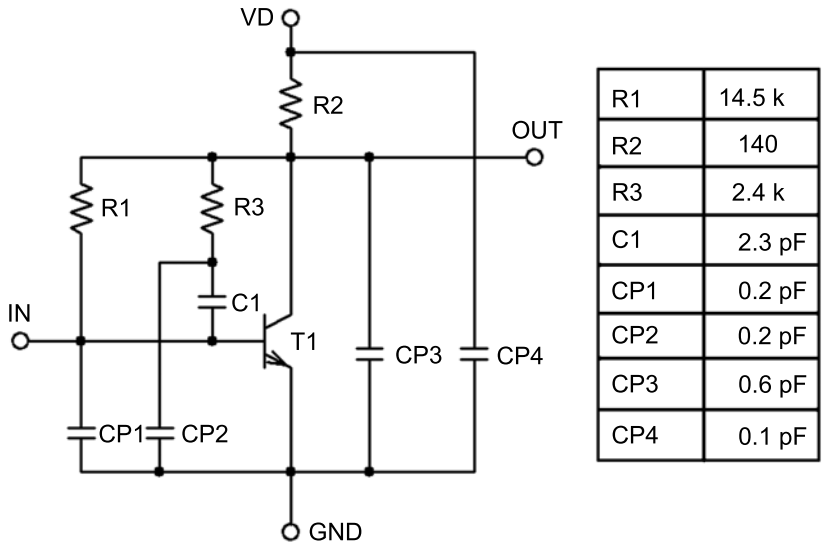

R1	14.5 k
R2	140
R3	2.4 k
C1	2.3 pF
CP1	0.2 pF
CP2	0.2 pF
CP3	0.6 pF
CP4	0.1 pF

Figure 6.3: Circuit diagram of the BGA420. The capacitances CP1, CP2, CP3 and CP4 are parasitic.

GHz. This leads to the effect that most datasheets the vendors offer for these devices start at frequencies of 0.1 GHz or even higher. The same holds for the integrated circuit (IC) BGA420 from Infineon Technologies AG which suits for application in a LNA for the Radio Detector. Its frequency range is DC to 3 GHz but unluckily the datasheet starts at 0.1 GHz. It can be found in the appendix A. The power gain is specified at this frequency as 19 dB, the NF is 1.9 dB, the intercept point of third order at the output is 9.5 dBm. All these values are denoted as typical for a bias voltage of 3 V with an ambient temperature of 25° C in a 50 Ω waveguide system. At these parameters the 1 dB compression point at the output is typ. -2.5 dBm at a frequency of 1 GHz.
The BGA420 is a silicon MMIC (Monolithic Microwave Integrated Circuit) cascadable gain block which is designed for applications in a 50 Ω waveguide system. It is packed in SOT343 with 4 pins: IN, OUT, GND (ground), VD (direct bias voltage). The circuit digram is shown in figure 6.3. With a set of SPICE model parameters for the transistor T1 given by the vendor and respecting the parasitic capacitances this circuit is a complete simulation model of the BGA420. The IC uses a transistor in emitter circuit with its operating point already adjusted and the use of voltage feedback. This design has already been discussed in section 5.1 (cf. figure 5.8).

The LNA shall obtain its bias voltage via the coaxial cable at the output. This is called *phantom powering* and done by one bias-T for each channel. The OUT pin of the BGA420 is protected against the direct voltage by a high pass whereas the VD pin is blocked for the signal by a low pass. Both pins can now by connected to provide the phantom powering.[1] This is illustrated in figure 6.4.
Since the bias voltage may contain a ripple voltage it can be smoothed by the net-

[1]Note that the bias-T uses low and high passes as well to give direct voltage only into the direction of the LNA and the signal can not pass towards the direct voltage source.

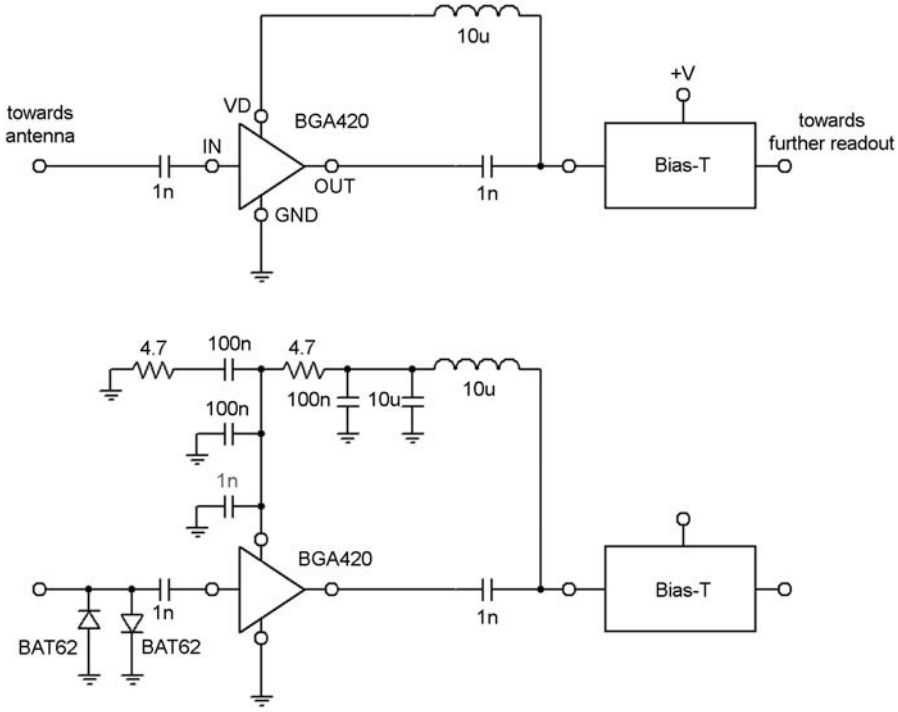

Figure 6.4: Top: The BGA420 is biased by a bias-T at the output of the amplifier. Bottom: The basic circuit of the LNA. A network to smoothen possible ripple voltage in the bias voltage and diodes to avoid overmodulation of the amplifiers input are added to the circuit above.

work added in the same figure. Alternating parts of the voltage drop down at the resistance, whereas the direct parts drop down at the capacitance[2].
To avoid the bias voltage to reach the input of the LNA a capacitance is used in front of the IN pin. It also acts as a filter for short-waves still received by the antenna. Nevertheless, the major filtering in the analog electronic chain is done behind the LNA by filters of higher order as shown in figure 4.7.
To avoid overmodulation of the LNA's input two Schottky diodes of the type BAT62 from Infineon are placed at the input towards ground. They shorten the input if the voltage gets too high. Their reverse voltage is 40 V at 25° C and their total maximum power dissipation is 100 mW for temperatures below 85° C.

Impedance Matching

The input reflection S_{11} of the basic circuit, described in the paragraph above and shown in figure 6.4, is simulated in a 50 Ω waveguide system and the results are shown left in figure 6.5. The input impedance of the LNA at 55 MHz is about (147.7 - i·53.0) Ω. This is equal to an absolute value of S_{11} of 0.54 and a phase of -13.5°. Following the steps of the example of selective impedance matching at the end of

[2]The smoothing network is designed to add a voltage regulator if desired and keep it from oscillating.

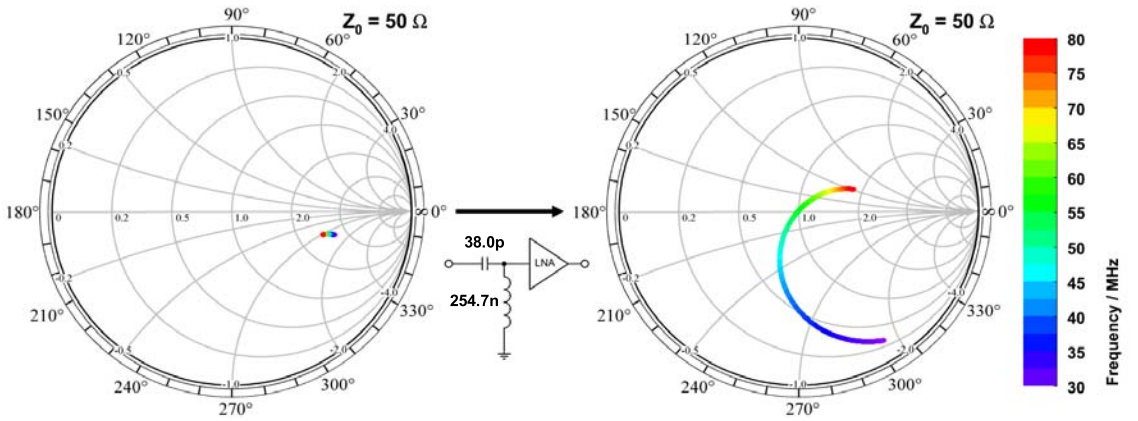

Figure 6.5: Left: Simulation of the input impedance of the basic circuit shown in figure 6.4. Right: Simulation of the input impedance of the same LNA with the matching network shown in the middle.

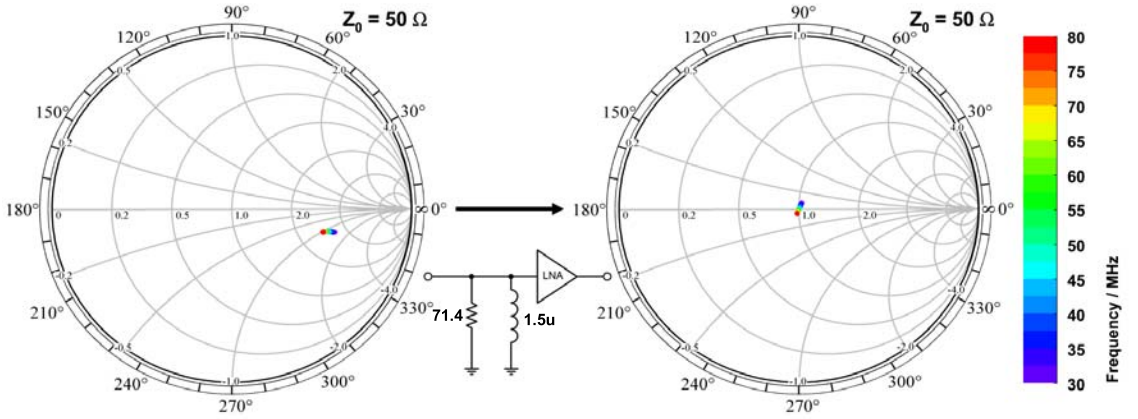

Figure 6.6: Left: Simulation of the input impedance of the basic circuit shown in figure 6.4. Right: Simulation of the input impedance of the same LNA with the matching network shown in the middle.

section 5.3, a matching network is found consisting of a shunt inductance of 254.7 nH and a series capacitance of 38.0 pF.
The matching network is added and the simulation is run again. Its results are shown right in figure 6.5. Now at 55 MHz the absolute value of S_{11} is smaller than 0.01 and the phase is -172.8°. This means the input impedance at this certain frequency is about (49.5 - i·0.1) Ω. But for most of the other frequencies the result is worse than before the matching. Therefore this kind of impedance matching is unsuitable for the broadband LNA.

Regarding the simulation results shown left in figure 6.5 it could come to mind that a shunt inductance and a shunt resistance could keep the transformed datapoints closer together than the attempt discussed above. In fact, this works out very well for L = 1.5 µH and R = 71.4 Ω as can be seen in figure 6.6. But unluckily

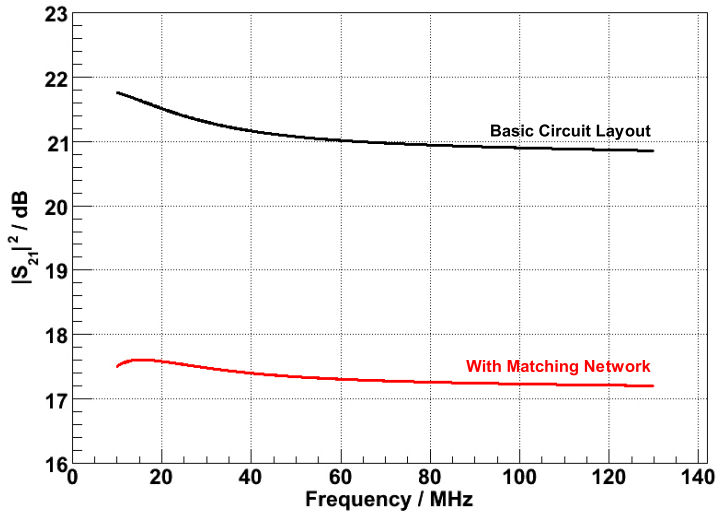

Figure 6.7: Simulation of the LNA's power gain $|S_{21}|^2$ as function of the frequency. The upper curve is for the basic circuit layout shown in figure 6.4. The lower curve is for the same circuit with the additional matching network consisting of a shunt inductance and a shunt resistance shown in figure 6.6.

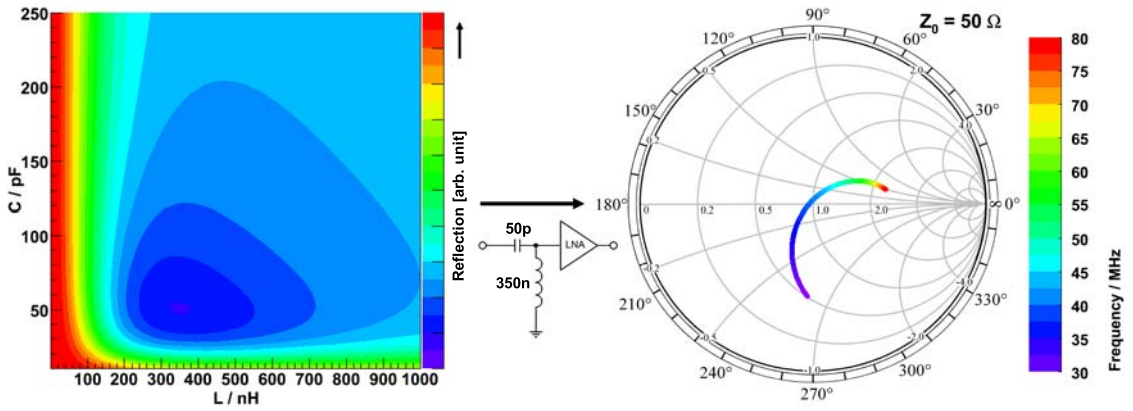

Figure 6.8: Left: Input reflection of LNA for different parameters of the shunt inductance L and the series capacitance C of the matching network. The input data derives from simulations. The reflection for different frequencies between 30 MHz and 80 MHz at identical points in the parameter space of L and C have been quadratically summed up. Right: Simulation of the input impedance of the LNA with the matching network shown in the middle found by the parameter scan.

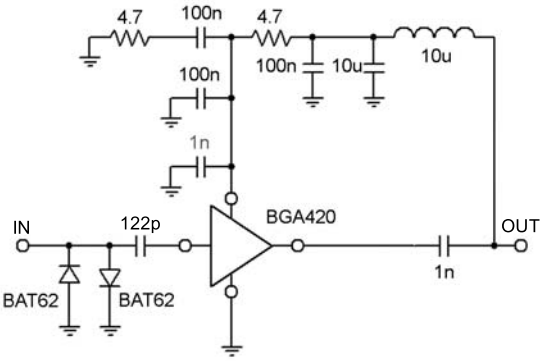

Figure 6.9: Schematic of the prototype LNA.

the shunt resistance leads to a cross flow of the input current which leads to a lower power gain $|S_{21}|^2$[3]. The power gain is shown for both circuits - the basic circuit shown in figure 6.4 and the one with the yet discussed matching network - in figure 6.7. A decrease of about 3.01 dB is a factor of 0.5. Regarding the simulation results this means that more than half of the power gain is lost using this matching network.

Using the kind of matching networks described in this work one should keep in mind that they act as filters (low pass, high pass, bad pass, band stop depending on the topology). Hence, not only the input impedance is transformed but also the overall transmission behavior of the LNA for different frequencies.

Regarding a matching network consisting of a shunt inductance L and a series capacitance C a parameter scan over frequencies from 30 MHz to 80 MHz with a stepsize of 50 kHz has been performed numerically to find the values of L and C where the overall reflection becomes a minimum. The reflection factors at each point in the parameter space for identical frequencies have been quadratically summed up to find an overall view for all considered frequencies. The result is shown left in figure 6.8. The right side of this figure shows the simulated reflection factor depending on the frequency in the Smith chart with $L = 350$ nH and $C = 50$ pF. Again the reflection for certain frequencies becomes better compared to the basic circuit layout. But on the other hand the spread of the absolute value of the reflection becomes larger. With this larger spread the power gain becomes more dependent on the frequency.

The conclusion of these impedance matching attempts is that the input reflection can not be made better without a decrease of the broadband LNAs performance for matching networks which can be described as filters of low order.

Using the simulations the input and output capacitances C_{in} and C_{out} are varied to make a fine-tuning of the LNA's power gain. With $C_{\text{in}} = 120$ pF and $C_{\text{out}} = 1$ nF the power gain was found to the most constant regarding the frequency. The

[3]The power gain is the squared voltage gain since input and output of the circuit are terminated with the same impedance.

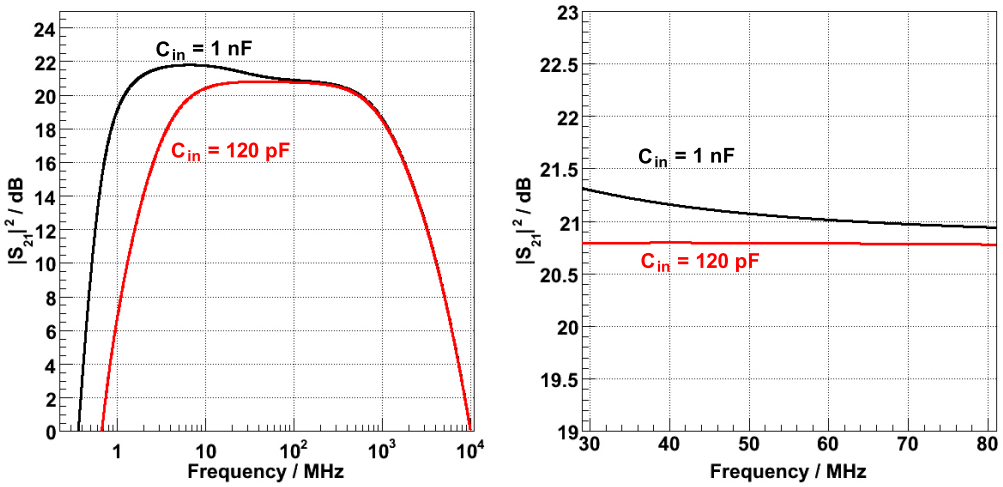

Figure 6.10: Left: Simulation of the power gain $|S_{21}|^2$ of the LNA as a function of the frequency for $C_{\text{in}} = 1$ nF (top) and 120 pF (bottom). Right: Same as left but with linear frequency axis and zoom into the frequency range of the LNA.

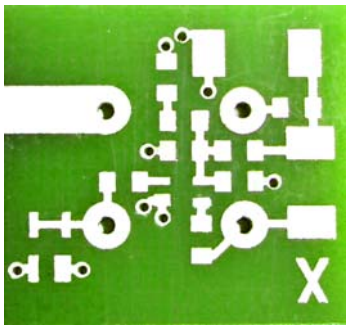

Figure 6.11: Photography of the FR4 board of the LNA. Shown are solder points for one channel. Dimensions: 20 mm x 20 mm. Colors are not natural.

simulation results are shown in figure 6.10. The power gain decreases a bit with the change of the capacitance. But this decrease is justified by the better characteristic of the gain. In a final step C_{in} is slightly changed to 122 pF which is a value that can be realized regarding capacitances offered by vendors. Figure 6.9 shows the final circuit of the LNA prototype.

Board Layout

Regarding the board layout the transmission line for the signal should be straight avoiding parasitic capacitances and inductances in the signal path. For the same reason the used parts should be kept as close together as it is allowed by the manufacturing process. The prototype board layout is shown in figure 6.11. It is of type FR4 with a 35 µm Cu-layer. If possible the grounds of the two LNA channels should be separated as far as possible to avoid ground loops and decrease the crosstalk of the two channels.
The parts chosen to be soldered to the board are surface mounted devices (SMD).

6.4 Housing and Mounting

Regarding the housing and the mounting of the LNA two different types are set up. The first is a single board with one channel on the upper side and one channel on the lower side with seperated grounds. This type will be called Type A. Its connectors are hole-trough pins which can be plugged directly into the board at the footpoint of the BS antenna. The footpoint is the point where the antenna is read out. For the BS the footpoint is situated above the highest dipole wire. In this case the BS needs a special board. It seems clear that any preamplifier should be mounted as close to the footpoint of an antenna as possible as the signal-to-noise ratio (SNR) gets lower with any lossy transmission line. In the worst case the signal would have dropped into the noise floor before it reaches the amplifier. To distinguish between signal and noise would become impossible. Figure 6.12 shows a mechanical drawing of the cross-section through the footpoint of the BS with a LNA plugged into it. Furthermore it shows a prototype of this type of LNA. It needs no additional housing since it is shielded by the boom of the antenna.
But the mounting of the amplifier at the footpoint of the antenna leads to a issue. Many LNAs which have been operating in the Radio Detector stations have been destroyed. Thunderstorms respective the high voltage they produce at the input of the LNA are believed to be a candidate for the destruction. Therefore a multi-level-design of a protection against lightning has been considered. The idea is to use different stages which shorten the input of the LNA for different ranges of voltages, with the voltage range of one stage overlapping with the voltage range of the next stage. The coarse protection is done by spark gaps inside the antenna itself. These sparks gaps are located on each board inside the antenna boom where the dipoles are connected with the antenna's central waveguide (see figure 6.13). They have a width of 0.07 mm and shorten for voltages down to about 800 V. The spark gap in the photography has a larger width since it is an early prototype. The medium protection is done by neon bulbs shortening the input for voltages down to 60 V. The fine protection is again a pair of Schottky diodes as described above. But the reverse voltage of 40 V of the type BAT62 is too low. Here the BAR14-1 from Infineon seems to be a good choice having a reverse voltage of 100 V and a total power dissipation of 250 mW for temperatures below 65° C.

Of course this cannot protect against lightnings which strike directly into an antenna but against lightnings which strike into objects away from the considered antenna. Unluckily the protection against lightning could not be tested sufficiently within this work. This led to another design of the LNA's housing:
The footpoint of the antenna is six up to ten meters above ground level depending on the height of the pole the antenna is mounted on. This makes an exchange of broken LNAs not very easy. Therefore it is decided to mount the LNAs directly beneath the antenna until the protection against lightning will be proved as totally reliable. This makes the maintenance much more handy and is believed to result in a higher duty cycle of a Radio Detector station. For this purpose each LNA channel becomes its own housing with N-connectors (male towards antenna, female at the output). A prototype is shown in figure 6.14. It can be directly attached to the

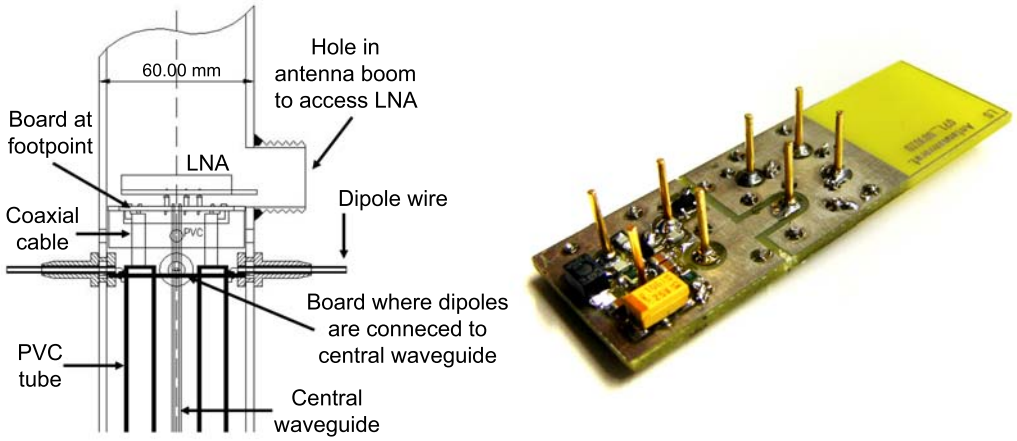

Figure 6.12: Left: Mechanical drawing of the cross-section through the footpoint of the Black Spider antenna with the LNA plugged into the board at the footpoint. Right: Prototype LNA (Type A) for the mounting option shown left. The other channel is on the other side of the board. - Type D uses the same mechanical layout.

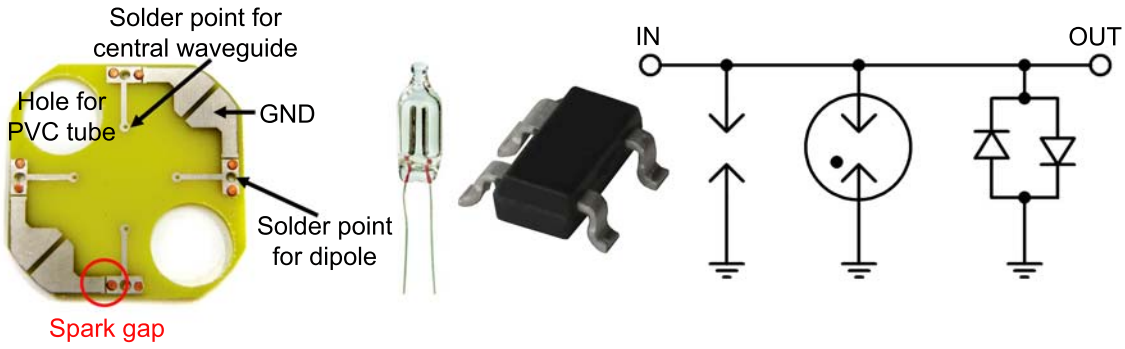

Figure 6.13: Multi-level-protection against lightning in front of the input of the LNA: From left to right: Coarse protection - Spark gaps on the board on which the dipoles of the antenna are connected to the central waveguide (cf. figure 6.12). Medium protection - Neon bulb. Fine protection - Schottky diodes. Schematic of the multi-level design.

antenna as shown in the CAD model in the same figure. This type will be referred to as Type B.
Except the different housings and connectors the two discussed mounting options have the difference of about four up to six meters of coaxial cable RG 58 C/U between the footpoint and the LNA for the second option or no cable for the first option. This leads to a attenuation of the signal up to 0.6 dB depending slightly on the frequency and the ambient temperature.

Unluckily at this point no LNA of Type B has been in a final state for tests in the laboratory since the decision to go for an LNA which is mounted outside of the

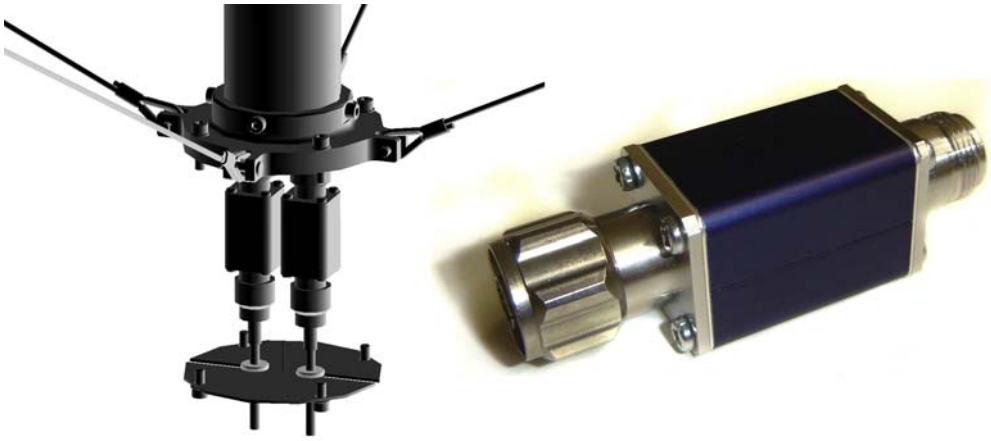

Figure 6.14: Left: CAD model of the Black Spider antenna showing its lower end with two LNAs at the bottom. Right: Housing of LNA Type B for the mounting option shown left.

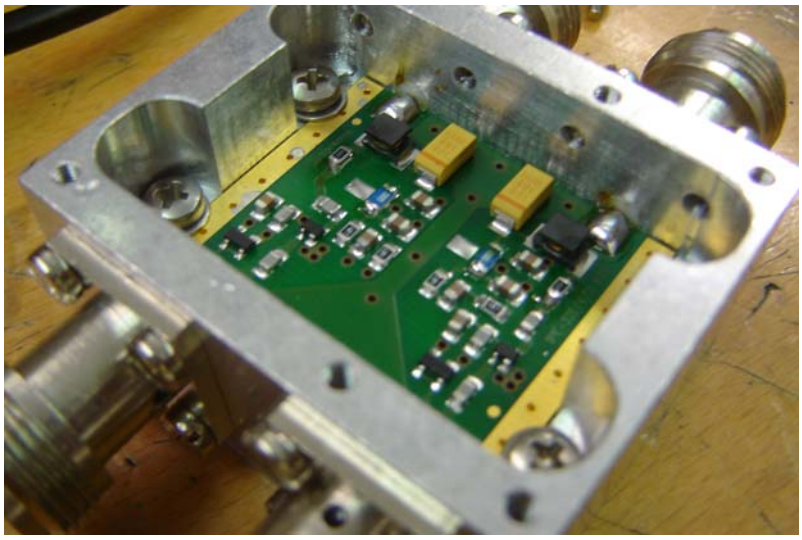

Figure 6.15: LNA Type C. The two channels using the basic circuit layout are housed side-by-side in an aluminum box with N-connectors. The upper side of the box has been removed to allow a look onto the board. Original design by [52].

antenna is relatively young. To investigate the properties of a solid housing, another type of LNA has been taken into the testing routines. It is the preamplifier shown in figure 6.15 developed by H. Gemmeke and O. Krömer [52] which was operating in the Radio Detector test setup. It uses the basic circuit layout shown in figure 6.4. The two channels are housed side-by-side in an aluminum box with N-connectors using the same ground. This LNA will be referred to as Type C. To examine whether the housing and connectors have influence on the characteristics of the amplifier, another LNA has been set up using the basic circuit layout as well but with the housing and mounting design of Type A. This LNA will be called Type D.

7. Testing the Design

In this chapter the tests of the LNAs of type A, C and D will be given and discussed. If not otherwise specified test routines were made with the spectrum analyzer Rohde & Schwarz FSH4 model .24. It contains a tracking generator which allows to operate it in a network analyzer mode measuring for example the s-parameters of a device under test (DUT). Its input and output impedances are 50 Ω. Specifications can be found at www.rohde-schwarz.com. The LNAs are biased by the bias-T MKU 270 from Kuhne electronic GmbH with a direct voltage of (5.000 ± 0.005) V if not otherwise specified. To connect the different parts of the test setups RG 58 C/U coaxial cables with an impedance of 50 Ω are used.

7.1 S-Parameters and Stability

To determine the s-parameters of the DUT the tracking generator of the network analyzer mode is used. To measure the forward transfer factor[1] the input of the DUT is connected to the tracking generator and its output is connected to the input of the spectrum analyzer. With the input impedance of the measuring device the output of the DUT is terminated with 50 Ω. This type of measurement is called *transmission measurement*. To measure the backward transfer factor (i.e. reverse isolation) the DUT is turned around regarding to the yet described setup so that the signal of the tracking generator is fed to the DUT's output. The input respective output reflection factor is determined by connecting the generator to the considered port and terminating the other port with 50 Ω. This is called *reflection measurement*.
Since the LNAs are biased by a bias-T at the output of the amplifier the DUT consists of the amplifier, 20 cm of coaxial cable and the bias-T. The bias-T is impedance matched to 50 Ω at its input and output with an absolute value of the reflection factor of 0.035 ± 0.007 (stat.) ± 0.058 (sys.) in the frequency range of the LNA. The attenuation caused by the 20 cm of cables has a maximum of 0.03 dB. These values are low enough to make a negligible difference between results for the DUT and the LNA. All other used cables do not contribute to the measurement results since their effect is corrected by calibrations. To calibrate the spectrum analyzer for a transmission measurement in a first step the DUT is replaced by a trough connection. In a second step the output of the tracking generator is terminated by 50 Ω. The device is now able to correct for the transmission characteristics of the measurement setup and the frequency dependence of the tracking generator. For

[1] i.e. in the case of an amplifier the voltage gain = $\sqrt{\text{power gain}}$, since input and output terminations are equal

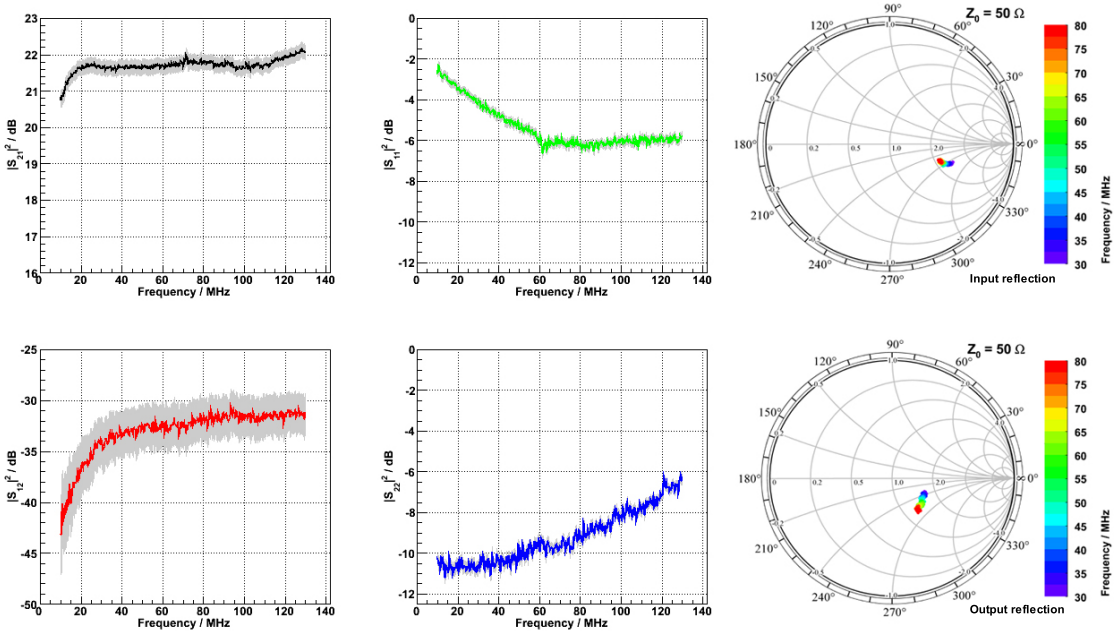

Figure 7.1: S-parameters of LNA Type A. Upper left: Power gain. Lower left: Reverse isolation. Upper right: Input reflection (absolute value and Smith Chart). Lower right: Output reflection (absolute value and Smith chart). The gray bands show the systematic uncertainty of the measurement. $+V = 5$ V, $Z_0 = 50\ \Omega$, $T = 21°$ C. Note that the frequency in the Smith Charts only ranges from 30 MHz to 80 MHz.

reflection measurement calibrations the port of interest of the DUT is replaced step-by-step by a short connection, an open connection and a 50 Ω termination. From this calibration routine the spectrum analyzer gains corrections for the following tests of the DUT.

Figures 7.1, 7.2 and 7.3 show the results of the s-parameter measurements. The gray bands indicate its systematic uncertainties. They are taken from the datasheet of the measurement device. The ambient temperature during the measurement has been $(21 \pm 1)°$ C.

The power gain between 30 MHz and 80 MHz is nearly constant for all types of LNAs. Type A shows an average value of 21.7 dB with maximum fluctuations of 0.3 dB. For Type C it is 23.0 dB with fluctuations up to 0.2 dB. The average value for Type D is 21.9 dB with a maximum fluctuation of 0.3 dB.

The input reflection of Type A stays below -4.0 dB in the frequency range of the LNA. Its output reflection remains smaller than -8.9 dB. The reverse isolation is lower than -31.2 dB. For Type C is found $|S_{11}|^2 <$ -5.3 dB, $|S_{22}|^2 <$ -9.4 dB, $|S_{12}|^2 <$ -31.8 dB and for Type D $|S_{11}|^2 <$ -4.6 dB, $|S_{22}|^2 <$ -7.3 dB, $|S_{12}|^2 <$ -30.2 dB.

The s-parameters are measured in a broader range than 30 MHz to 80 MHz since the actual setup of the Radio Detector has no filter between the antenna and the preamplifier. Signals are only filtered by the bandwidth of the antenna itself and the high pass consisting of the capacitance at the input of the amplifier IC. Therefore also signal beyond the 30 to 80 MHz band can reach the input of the LNA. An

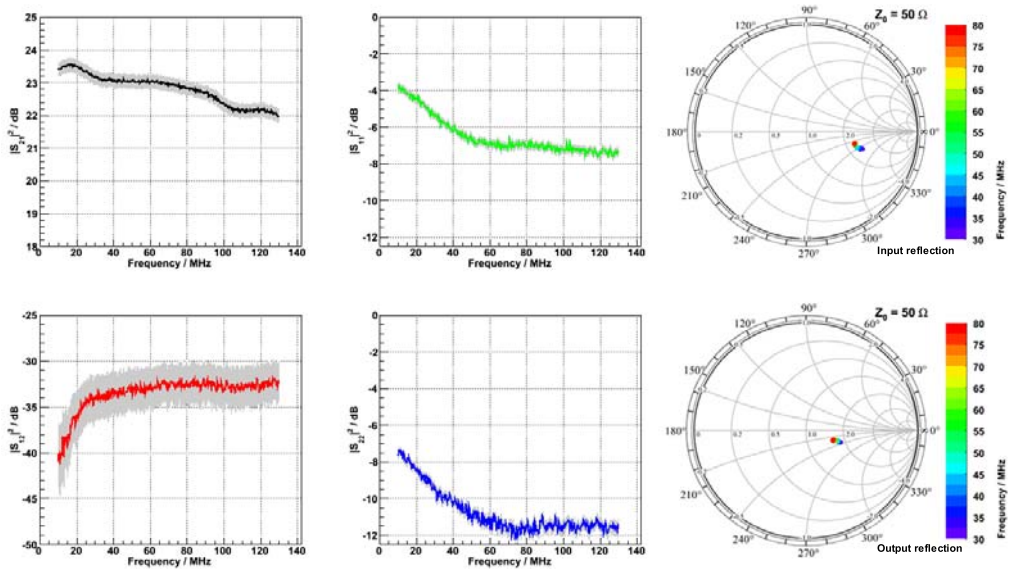

Figure 7.2: S-parameters of LNA Type C. Upper left: Power gain. Lower left: Reverse isolation. Upper right: Input reflection (absolute value and Smith Chart). Lower right: Output reflection (absolute value and Smith chart). The gray bands show the systematic uncertainty of the measurement. $+V = 5$ V, $Z_0 = 50\ \Omega$, $T = 21°$ C. Note that the frequency in the Smith Charts only ranges from 30 MHz to 80 MHz.

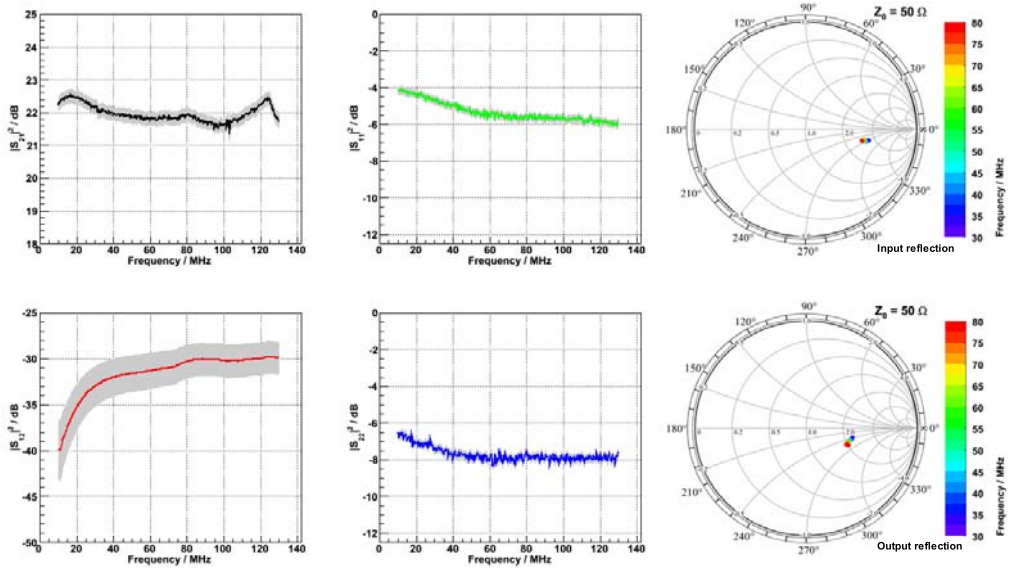

Figure 7.3: S-parameters of LNA Type D. Upper left: Power gain. Lower left: Reverse isolation. Upper right: Input reflection (absolute value and Smith Chart). Lower right: Output reflection (absolute value and Smith chart). The gray bands show the systematic uncertainty of the measurement. $+V = 5$ V, $Z_0 = 50\ \Omega$, $T = 21°$ C. Note that the frequency in the Smith Charts only ranges from 30 MHz to 80 MHz.

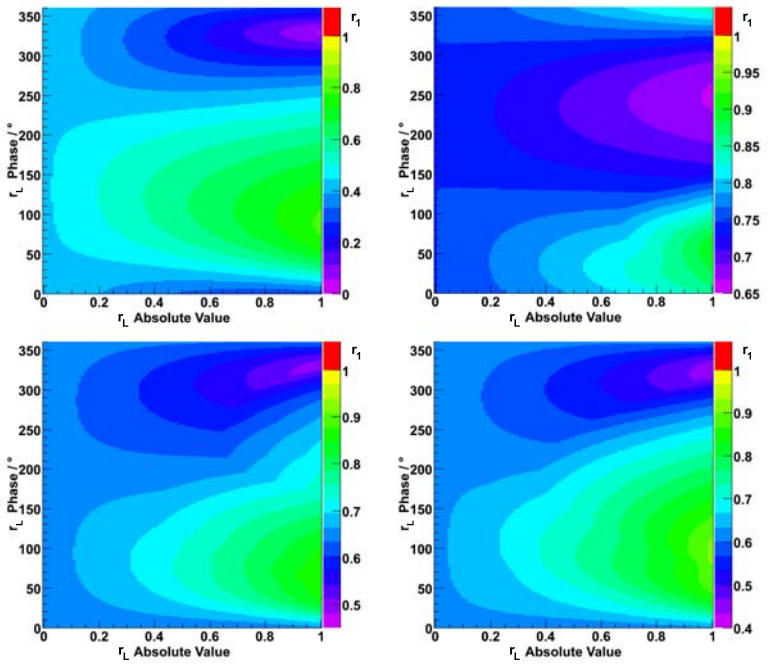

Figure 7.4: Reflection r_1 as function of the mismatch of the load r_L (absolute value and phase). The LNA is unconditionally stable for reflections < 1. Upper left: Type A at a frequency of 75.52 MHz. Upper right: Maximum of Type A for 10 to 130 MHz. Lower left: Maximum of Type C for 10 to 130 MHz. Lower right: Maximum of Type D for 10 to 130 MHz. Note that the ranges of the color axes vary in order to avoid only one color in a plot.

amplifier is *unconditionally stable* if it does not oscillate for any mismatch of the generator r_G or the load r_L. If the amplifier only oscillates for certain mismatches it is called *conditionally stable*. Regarding [53] the requirement for stability is given by the following inequations for the ratio of forward and reverse waves at the input side of the amplifier r_1 and its output side r_2.

$$|r_1| = \left| S_{11} + \frac{S_{12}\,S_{21}\,r_\mathrm{L}}{1 - S_{22}\,r_\mathrm{L}} \right| < 1$$
$$|r_2| = \left| S_{22} + \frac{S_{21}\,S_{12}\,r_\mathrm{G}}{1 - S_{11}\,r_\mathrm{G}} \right| < 1 \tag{7.1}$$

Since on the one hand the antenna in front of and on the other hand the filter chain behind the LNA lead inevitably to total mismatches, r_1 and r_2 are determined from the s-parameters for any possible absolute value and phase of r_G and r_L. This is shown in figures 7.4 and 7.5. The upper left plot shows r_1 respective r_2 for the LNA Type A at an arbitrary frequency of 75.52 MHz. The other plots are for all frequencies from 10 MHz to 130 MHz where the maximum of r_1 respective r_2 is hold. The frequency resolution is 190.5 kHz.
All LNAs are unconditionally stable and meet the functional requirements regarding the s-parameters.

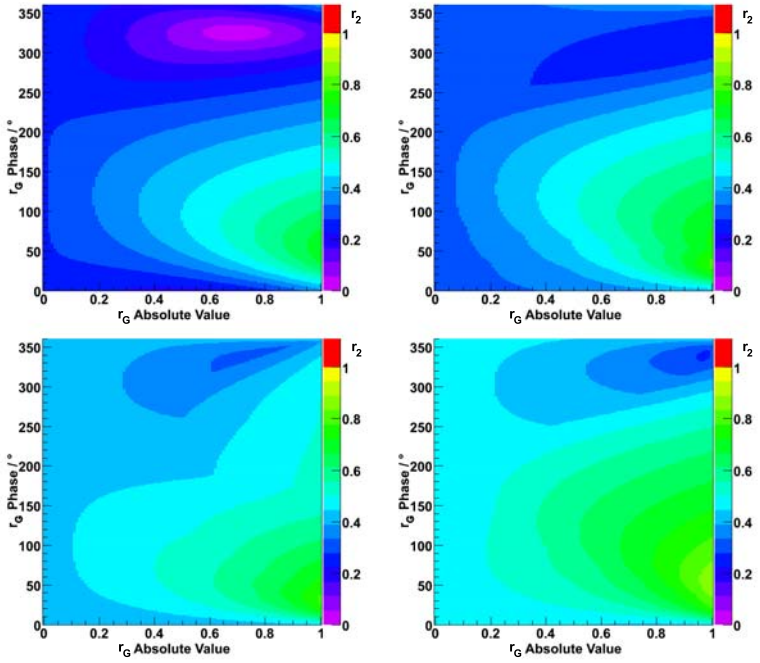

Figure 7.5: Reflection r_2 as function of the mismatch of the generator r_G (absolute value and phase). The LNA is unconditionally stable for reflections < 1. Upper left: Type A at a frequency of 75.52 MHz. Upper right: Maximum of Type A for 10 to 130 MHz. Lower left: Maximum of Type C for 10 to 130 MHz. Lower right: Maximum of Type D for 10 to 130 MHz.

7.2 Noise

Several attempts are made to measure the intrinsic noise of the LNAs with the spectrum analyzer FSH4.
One attempt is to measure the signal-to-noise ratio (SNR) at the input and the output of a LNA as illustrated in figure 5.17.
Another attempt uses a noise generator at the LNA's input. In the first state the generator is switched off and thus feeds a power $1 \cdot k_\mathrm{B}\, T_0\, \mathrm{d}f$ with the Boltzmann constant k_B, the ambient temperature T_0 and the noise bandwidth $\mathrm{d}f$ into the LNA. At the output of the amplifier the power P is measured. In the second state the noise generator is switched on and its noise power is adjusted to $m \cdot k_\mathrm{B}\, T_0\, \mathrm{d}f\,,\ m \in \mathbb{R}^+$ so that at the output of the LNA the power $2{\cdot}P$ is measured. The measurement setup is schematically shown in figure 7.6. The powers measured at the output are given by

$$\begin{aligned} P &= G\, k_\mathrm{B}\, T_0\, \mathrm{d}f + G\, k_\mathrm{B}\, T_0\, F_\mathrm{add}\, \mathrm{d}f \\ 2\,P &= G\, k_\mathrm{B}\, m\, T_0\, \mathrm{d}f + G\, k_\mathrm{B}\, T_0\, F_\mathrm{add}\, \mathrm{d}f \end{aligned} \tag{7.2}$$

with the power gain of the LNA G and its additional noise factor F_add. Dividing the first equation by the second one, it is found that

$$\begin{aligned} \frac{1}{2} &= \frac{1 + F_\mathrm{add}}{m + F_\mathrm{add}} \\ \Rightarrow F_\mathrm{add} &= m - 2\,. \end{aligned} \tag{7.3}$$

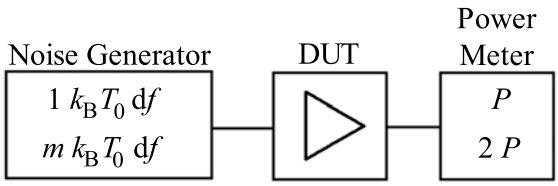

Figure 7.6: Setup for noise measurement. In the first state the noise generator is switched off. The input of the DUT receives the noise power $k_\mathrm{B}\,T_0\,\mathrm{d}f$. At its output the power P is measured. In the second state the noise generator is adjusted to a noise power so that at the output of the DUT $2 \cdot P$ is measured.

Since the additional noise of the amplifier is dependent on the frequency f this measurement has been performed for certain single frequencies but also in single measurements over all frequencies in the 30 to 80 MHz band by substituting the power measured at the output in the second state by $s \cdot P$, $s \in \mathbb{R}^+$. In this case $F_\mathrm{add}(f) = (m - s(f))/s(f) - 1$.
All attempts lead to unphysical results showing additional noise factors below zero. It is believed that the measurement device internally changes its settings with receiving signals of too different powers at its front end which results in a change of the intrinsic noise of the device. Without exact knowledge of this intrinsic noise the additional noise factor cannot be determined correctly.
In a further attempt the output power of the LNA was measured while its input was shortened. But the additional noise of the amplifier seems to be too low compared to the intrinsic noise of the measurement device to result in a reasonable noise figure.

To make a reliable measurement of the noise figure of the LNAs the signal analyzer Rohde & Schwarz FSQ40 is used. The determination of noise figures is one of its measurement routines[2]. It is done by the *Y-factor method* [54], [55]:
The method uses the noise linearity for linear two-port devices as it was discussed in different terms in section 5.4 and is illustrated in figure 7.7. It shows the power output as a linear function of the temperature of a noise source at the input of a DUT. Its slope is

$$k_\mathrm{B}\,G\,\mathrm{d}f = \frac{N_2 - N_1}{T_\mathrm{h} - T_\mathrm{c}}\,. \tag{7.4}$$

For noise source temperatures of zero Kelvin the power output is solely the additional noise power N_add of the DUT. For higher temperatures also the noise of the noise source amplified by G occurs. Modern noise figure analyzers use noise sources with two states - *hot* and *cold* - which they can switch from one to the other internally. The level of noise in these two states has to be known exactly. It is given by the excess noise ratio

$$ENR = \frac{T_\mathrm{h} - T_\mathrm{c}}{T_0} \tag{7.5}$$

with the hot noise temperature T_h, the cold noise temperature T_c and $T_0 = 290$ K. Typically T_c is set to T_0 to change the two states from hot and cold to *on* and

[2]Hence, the expression *noise analyzer* may be used for this device.

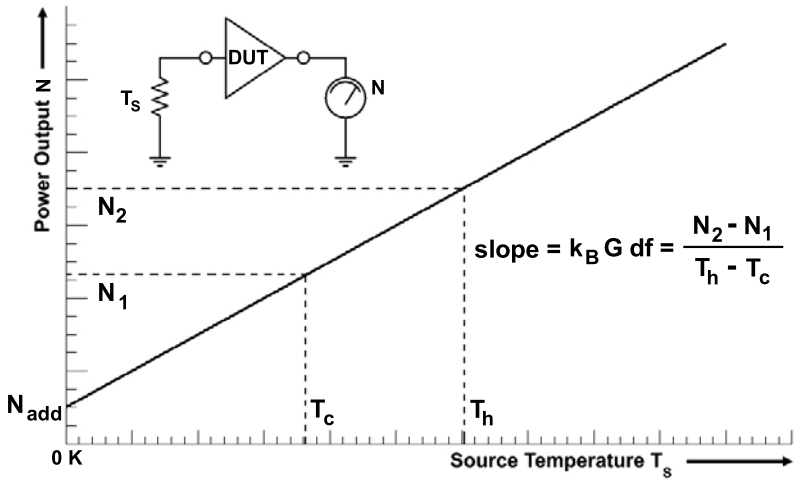

Figure 7.7: The power output of a linear two-port is a linear function of the source temperature. If the temperature of the source is zero Kelvin the power output of the DUT is solely its additional noise power N_{add}.

off. The analyzer uses temperature sensors to correct for ambient temperatures differing from T_0. The noise source is calibrated by the manufacturer and the ENR is characterized versus the frequency and stored inside the noise analyzer.
The Y-factor is defined as the ratio of the power output in the two states

$$Y = \frac{N_2}{N_1} \qquad \Rightarrow Y - 1 = \frac{N_2 - N_1}{N_1}. \tag{7.6}$$

These two powers are given by

$$\begin{aligned} N_2 &= k_{\mathrm{B}}\, G\, \mathrm{d}f\, T_{\mathrm{h}}\, F \\ N_1 &= k_{\mathrm{B}}\, G\, \mathrm{d}f\, T_0\, F \end{aligned} \tag{7.7}$$

with the noise factor F. Therefore

$$F = \frac{N_1}{k_{\mathrm{B}}\, G\, \mathrm{d}f\, T_0} = \frac{N_1}{T_0}\,\frac{T_{\mathrm{h}} - T_0}{N_2 - N_1} = \frac{T_{\mathrm{h}} - T_0}{T_0}\,\frac{N_1}{N_2 - N_1} = \frac{ENR}{Y - 1}\,. \tag{7.8}$$

With $F = 1 + F_{\mathrm{add}}$ the additional noise factor is $F_{\mathrm{add}} = ENR/(Y-1) - 1$ and the additional noise power is

$$N_{\mathrm{add}} = k_{\mathrm{B}}\, G\; T_0\, \mathrm{d}f \left(\frac{ENR}{Y - 1} - 1\right). \tag{7.9}$$

In section 5.4 the noise figure has already been defined as $\mathrm{NF} = 10\,\log_{10} F$.

Since a mismatch between the noise source and the input of the DUT leads to multiple reflections, a matched 10 dB attenuator is set between the two devices. With this attenuator re-reflections are attenuated by 20 dB. The FSQ40 is set to

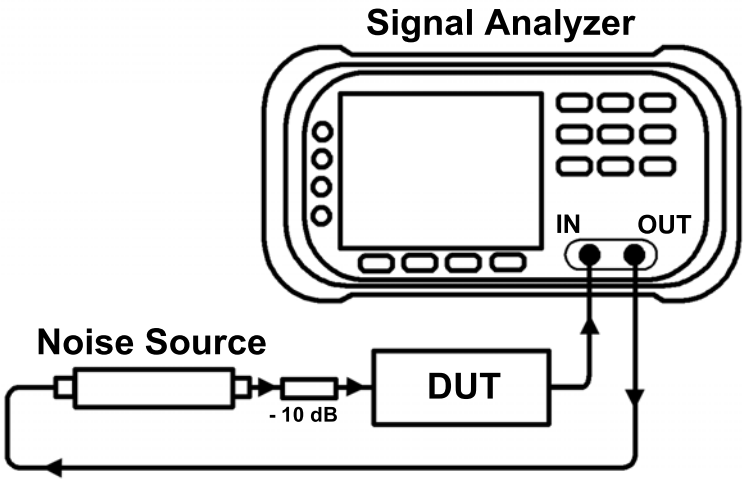

Figure 7.8: Schematic view of the NF measurement setup using a signal analyzer and its noise source.

correct for the attenuator. Since the measurement device also contains amplifiers the option of second-stage correction is turned on. It corrects for further additional noise factors, which do not come from the DUT, using the cascade noise equation (5.48). The gain of the DUT is needed for the determination of the NF and measured simultaneously during one frequency sweep. A schematical view of the measurement setup is given by figure 7.8.

During the measurement LNA Type A and D have been shielded with an metallic cylinder since interference with other devices in the laboratory might influence the measurement due to the very low levels of the noise powers. The results of the measurement are shown in figure 7.9. The ambient temperature has been $(23 \pm 1)^\circ$ C. The NF of LNA Type A and D with values up to about 18.5 dB respective 25.5 dB are unexpectedly high, whereas Type C shows a NF of 1.9 dB over the whole frequency range in agreement with the amplifier ICs datasheet. The circuit layouts of the different LNAs are too equal to evoke this difference in the NF. Also the board layout is not believed to be the critical point [56]. What remains is the mechanical layout of the types A and D. In fact, hole-through pin connectors do not seem to be the best choice for radio frequency applications. Nevertheless, the differences may also occur from bad soldering points on the board into which the types A and D are plugged into for this measurement. Further test with a different board should be performed but unluckily the FSQ40 has only been accessible once during this work.

7.3 Linearity of the LNA

The examine the linearity of the LNAs the one-tone-method is performed to determine the 1 dB compression point and the two-tone method to determine the interception points of third and fifth order. In the one-tone method a signal of known power is given to the input of the DUT. Its output power is characterized

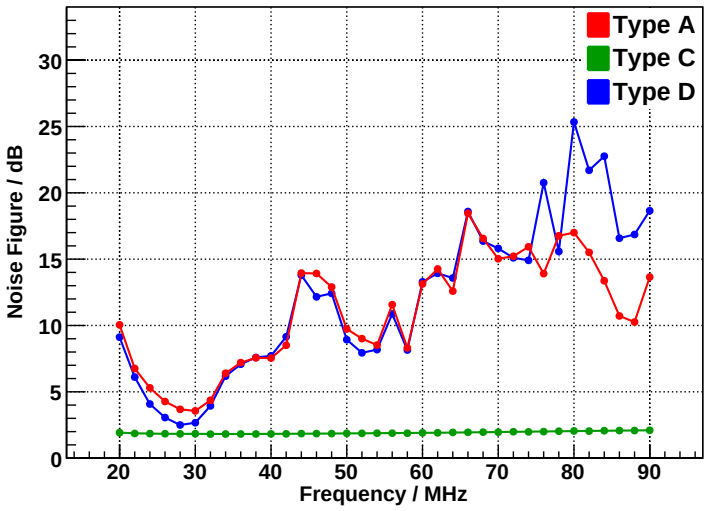

Figure 7.9: The noise figure as function of the frequency for the three different types of LNAs. Measured with a R&S FSQ40 signal analyzer. $+V = 5$ V, $Z_0 = 50\ \Omega$, $T = 23°$ C.

as a function of the input power. The same goes for the two-tone method with the difference that the input signal is a superposition of two signals with the same level but different frequencies.
Signals are generated with Agilent 33250A function generators. The power output of the DUT is measured with the FSH4 spectrum analyzer. The results are shown for LNA Type A at a frequency of 55.0 MHz with the second generator producing a signal at 55.1 MHz in figure 7.10. Further test frequencies are 30.0 MHz (respective 30.1 MHz) and 80.0 MHz (respective 79.9 MHz). The corresponding plots can be found in the appendix A. The ambient temperature has been (19 ± 1)°C. The measurements can not be performed for lower levels of the input signals since for the one tone method the minimum output power of the function generator defines a limit. For the two-tone method even lower output powers of the DUT drop into the intrinsic noise level of the spectrum analyzer. The figure shows also constant noise levels at 55 MHz. The lower level is determined from the measurement of the antenna noise done at the southern site of the Pierre Auger Observatory (cf. figure 6.1). A NF of 2 dB has been added since LNA Type C shows a NF close to this value. The upper noise level is the antenna noise plus a NF of 9.5 dB. This is the NF of LNA Type A as shown in figure 7.9.
The uncertainties of the input and output power of the LNA are derived by the scale reading precision using the FSH4. To determine the 1 dB compression point IP_{-1dB} and the intermodulation points $IP_{3,5}$ fits of linear function are performed to the linear part of the measured curves. The fitting results are given in table 7.1. Regarding the reduced χ^2 the uncertainties of the determined powers (0.2 dB - 1.0 dB depending on the level of power) seem generally to be underestimated. The infinity values of the reduced χ^2 result from the fact that in these cases no degrees of freedom are left. Hence the errors of the slopes seem underestimated as well. It

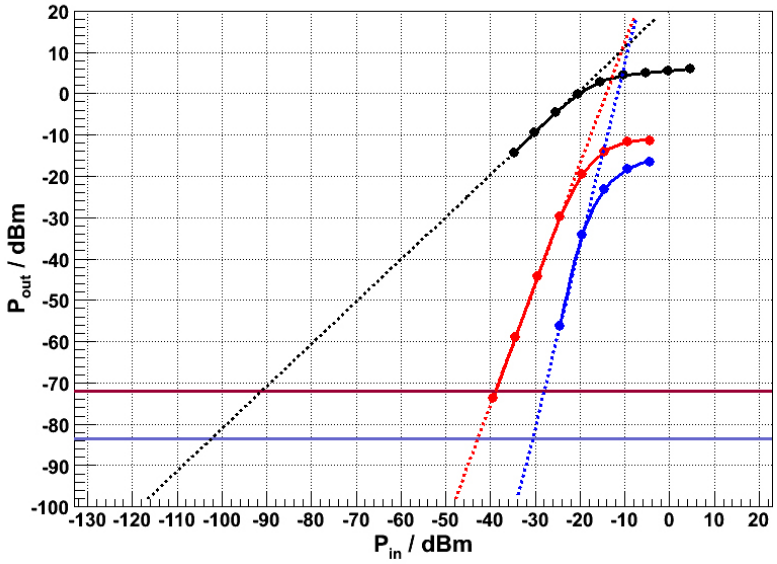

Figure 7.10: Measurement of the 1 dB compression point and the intermodulation points of third and fifth order of LNA Type A at a frequency of 55 MHz. The constant output powers are noise levels. $+V = 5$ V, $Z_0 = 50\ \Omega$, $T = 19°$ C. See text for further information.

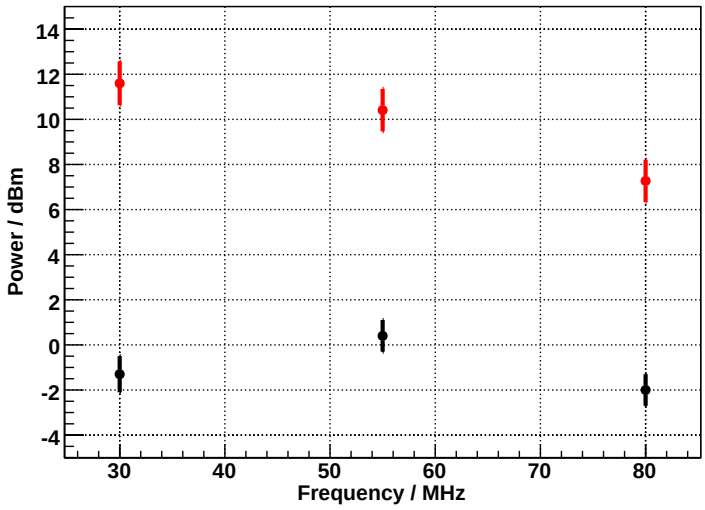

Figure 7.11: $P_{-1dBout}$ (black) and IP_{3out} (red) of LNA Type A as functions of the frequency. $+V = 5$ V, $Z_0 = 50\ \Omega$, $T = 19°$ C.

		30 MHz	55 MHz	80 MHz	Unit
1^{st} order	slope	1.072 ± 0.008	1.024 ± 0.003	1.015 ± 0.004	-
	y-intercept	23.27 ± 0.25	21.31 ± 0.09	18.97 ± 0.10	dBm
	red. χ^2	∞	32	76	-
3^{rd} order	slope	3.030 ± 0.071	2.914 ± 0.045	2.940 ± 0.044	-
	y-intercept	44.48 ± 2.42	41.40 ± 1.45	41.12 ± 1.44	dBm
	red. χ^2	0.3	0.05	0.1	-
5^{th} order	slope	4.724 ± 0.141	4.400 ± 0.141	4.092 ± 0.143	-
	y-intercept	59.75 ± 3.76	51.39 ± 3.12	43.84 ± 3.14	dBm
	red. χ^2	∞	∞	∞	-

Table 7.1: Fitting results for the one-tone and two-tone measurement.

is expected to find a slope of the exact value of the considered order(, i.e. a slope of 1 for the first order, of 3 for the third order and of 5 for the fifth order). Only one third of the parameters agrees with the theory within three standard deviations. The rest agrees only within about four to nine standard deviations.
The intercept points are determined numerically. The uncertainties of the fit parameters are propagated to the ones of the intercept points by using a Monte Carlo method assuming that the uncertainties are Gaussian. In fact, even though the dB scale is logarithmic in the power, the FSH4 spectrum analyzer shows Gaussian fluctuations of power measurements in the dB scale at any measurement. The 1 dB compression point has been taken directly from the plots. Its uncertainty follows from the scale reading precision. The final measurement results are displayed in table 7.2. The output intercept points are plotted versus the frequency in figure 7.11. Little can be said about the dependency of the intercept points due to the low statistics. More datapoints are definitely needed.
Also it is of little use talking about the the values of the dynamic range of the amplifier. First of all the noise level is not exactly known since the results of the NF measurement are not sufficiently understood. To get a first impression the different noise levels have been plotted in figure 7.10. Secondly for a broadband amplifier the upper limit of the dynamic range is not limited to the power at which the intermodulation products of third order get higher than the noise, but those of second order.[3] The measurement of intermodulation products of even orders can not be performed reliably with the existing measurement setup. During measurement the (frequency)

[3]This holds only for P_{-1dBin} being of higher value than the input power at the intercept of the noise level and the second order intermodulation products, which is realized in the considered case.

	30 MHz	55 MHz	80 MHz	Unit
P_{-1dBin}	-22.0 ± 1.0	-19.5 ± 1.0	-19.6 ± 1.0	dBm
$P_{-1dBout}$	-1.3 ± 0.8	0.4 ± 0.7	-2.0 ± 0.7	dBm
IP_{3in}	-10.9 ± 1.3	-10.6 ± 0.8	-11.5 ± 0.8	dBm
IP_{3out}	11.6 ± 1.0	10.4 ± 1.0	7.3 ± 1.0	dBm
IP_{5in}	-10.0 ± 1.1	-8.9 ± 1.0	-8.1 ± 1.1	dBm
IP_{5out}	12.5 ± 1.0	12.1 ± 1.0	10.7 ± 1.0	dBm

Table 7.2: Results of the one-tone and two-tone measurement.

span of the spectrum analyzer has to be kept small otherwise the intrinsic noise of the device rises. This again leads to even few degrees of freedom for the fits which have to be performed in order to extrapolate the intercept points. All frequencies of interest (i.e. the two input signals and at least one intermodulation product of second order) have to lie within the span to guarantee a control over the measurement. This could not be realized since at least one signal lies too far far away from the others. It is tried to switch the span during the measurement but the result is data which has to be dismissed. The experimental setup is not perfect for this kind of measurement. Again an adequate signal analyzer might lead to better results and much higher statistics, since it is designed to measure the intermodulation products with good internal control and might perform frequency sweeps at the same time. Nevertheless, the third order intercept point is of special interest since it is a value given for most amplifiers. It allows a broader comparison to other types than the IP_2. Due to the little informative value of this measurement it is decided to wait for tests of LNA Type C and D until a more solid measurement setup is accessible. Independently from this work O. Krömer has determined the $P_{-1dBout}$ to -1 dBm and the IP_{3dBout} to 14 dBm for the LNA Type C[4] [52].

7.4 Two-Channel Crosstalk

To measure the two-channel crosstalk of a LNA one channel receives a known reference signal at its input while the output of other channel is read out. The output of the first channel and the input of the second channel have to be terminated with the impedance of the waveguide system. This setup is shown schematically in figure 7.12. Using the terminology of this figure the crosstalk is the measured output power of channel 2 referred to the output power of channel 1. The measurement is performed using the network analyzer mode of the FSH4 ($Z_0 = 50\ \Omega$). Since

[4]Unluckily no frequency is given.

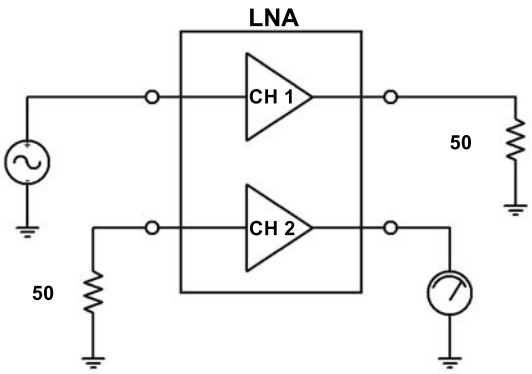

Figure 7.12: Schematic view of the measurement of the two-channel crosstalk. A know signal is transmitted to the input of one channel of the LNA. The output power of the other channel is detected. The ports not connected to the generator or the measurement device are terminated with 50 Ω.

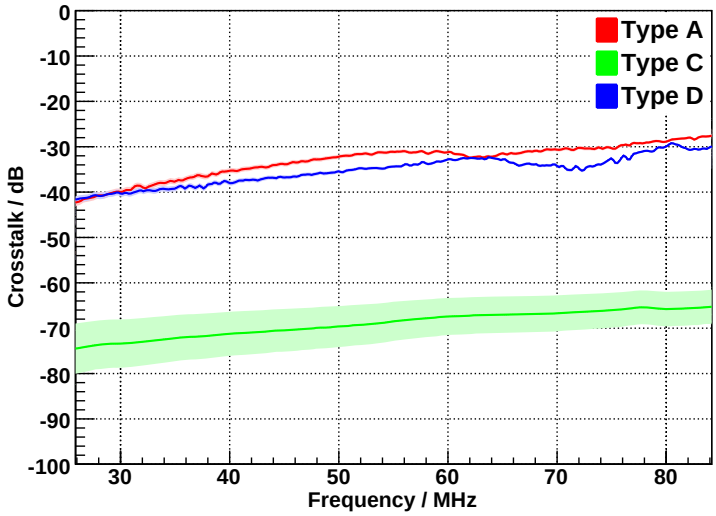

Figure 7.13: The two-channel crosstalk of LNA Type A (red), C (green) and D (blue). The colored bands shows the systematic uncertainties of the measurement. $+V = 5$ V, $Z_0 = 50\ \Omega$, $T = 18°$ C.

the spectrum analyzer displays the output power of channel 2 referred to the input power of channel 1 the power gain of channel 1 has to be subtracted from the raw data. Therefore the power gain is measured as well as described in section 7.1.
Figure 7.13 shows the results of the measurement which is made at an ambient temperature of $(18 \pm 1)°$ C. The colored bands indicate the systematic uncertainties. In the 30 to 80 MHz band the crosstalk of the LNA Type C stays below -65 dB. Types A and D show values between about -40 dB and -28 dB. A functional requirement of the LNA has been a crosstalk below the crosstalk of the Black Spider antenna. In section 6.1 an average value of -42 dB has been given for the crosstalk of the antenna. Therefore the LNA types A and D do not fulfill this functional requirement. The

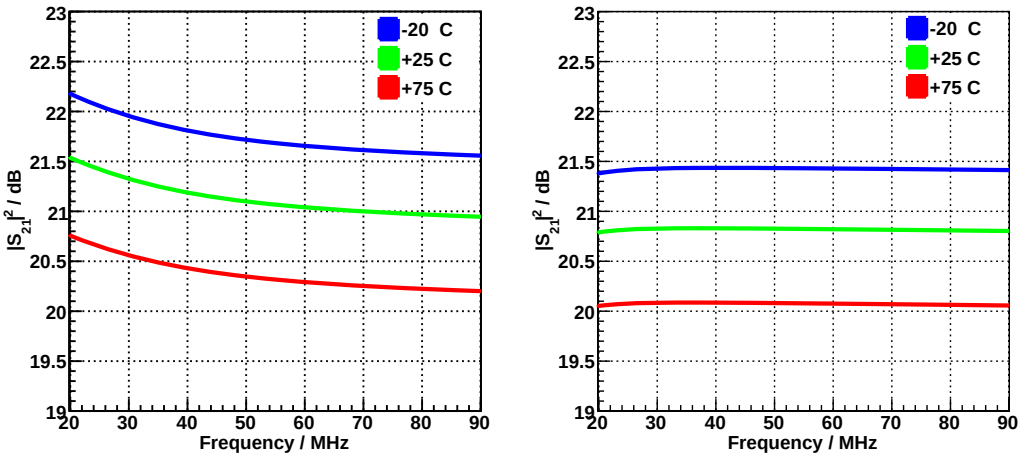

Figure 7.14: Simulation of the power gain as function of the frequency with ambient temperature as parameter (from top to bottom: -20° C, +25°C, +75° C). Left: Simulated circuit of LNA Type C and D. Right: Simulated circuit of LNA Type A and B. $+V = 5$ V, $Z_0 = 50\ \Omega$.

crosstalk of Type C satisfies the demand.
The large difference between the different types of LNAs is due to their housings and connectors. The hole-through pin connectors of types A and D are not shielded allowing more transmission from signals of one channel to the other. Since LNA Type B houses solely one channel per box and uses N-connectors as well as Type C, its crosstalk is expected to be even lower than the one of Type C. But to confirm this statement tests of Type B are essential.

Temperature Dependency

The dependency of the characteristics of the LNAs on the ambient temperature has not been tested within this work. Figure 7.14 shows a simulation of the two circuits used for the LNAs under test. The power gain is simulated for different ambient temperatures: -20° C, +25° C and +75° C. It is the most interesting value to be tested in this context since it might be used in future data analysis for corrections. The test in the laboratory is essential since on the one hand it can show the real dependency of the LNA's characteristics on the temperature and on the other hand if the LNA can cope with these temperatures. Also of interest is a long term measurement with the DUT passing several cycles of being heated and cooled down for relatively long terms. This can proof whether the LNAs can also withstand the high thermal fluctuations which occur at the southern site of the Pierre Auger Observatory.

Further Ratings

All types of LNAs under test show a power consumption of (62 ± 1) mW at $+V = (5.000 \pm 0.005)$ V and $T = (23 \pm 1)°$ C per channel. This satisfies the functional requirement for a low power consumption.

From simulations a maximum of $+V = 7.5$ V is determined. This value is higher than the given maximum rating of the BGA420's device voltage VD = 6 V. Since simulation models do not respect any maximum ratings, the latter value should be taken serious. Regarding the maximum RF input power of the amplifier IC (given in its datasheet), the maximum RF input power of the LNAs found by simulations is $P_{\mathrm{RFin}} = 1.4$ dBm. Nevertheless, LNA Type A could cope during tests with input powers of 5 dBm for several minutes, without showing any damage in further tests. These tests have been performed to look for the damaged caused by overmodulation. Maximum respective minimum ratings for the ambient temperature are T = -55° C ... 150° C. Since no measurements regarding the temperature have been performed this rating is taken from the datasheets of the devices used for the LNA.
The costs for LNA Type B are expected to be about 30 €.

Conclusion

Although all types of LNAs show satisfying s-parameters and are unconditionally stable only Type C meets all the functional requirements. The NF and the two-channel crosstalk are unacceptably high for both, Type A and Type D. The dynamic range can not be given since the intermodulation products of second order is of high interest for a broadband amplifier and could not be determined. Intermodulation might become an issue for the broadband receiving system of the Radio Detector.
The hole-through pin connectors of Type A and D are not the right choice for radio frequency applications. They are believed to cause the high value of the crosstalk and might have led to the enormous values of the NF. Since Type B uses N-connectors and only one channel per housing box, it is expected that it will meet all the functional requirements. Moreover, the crosstalk is expected to be even better than for the LNAs under test and the power gain should be as constant as for Type A. Nevertheless, tests of Type B have to follow.

8. Summary and Outlook

The radio detection technique is a vivid field of research in cosmic ray physics. With AERA (Auger Engineering Radio Array) a huge effort to develop a cost-effective extension of the established Surface Detector and Fluorescence Detector at the Pierre Auger Observatory is made. This large scale radio detector is designed to measure radio pulses emitted by ultra-high-energy cosmic rays and their secondary shower particles within the 30 to 80 MHz band. Each detector station consists of a logarithmic-periodic-dipole antenna and a receiver. The first device in the signal chain of the receiver system is a low-noise-preamplifier (LNA) which plays a key role for the success of the experimental setup. Without it further electronics might not distinguish between the signal of physical interest and the background noise. Furthermore, with sufficiently high gain the noise of all amplifiers used in the signal chain is predominately given by the noise of the LNA. Within this thesis the layout of the LNA designed for the radio detector AERA has been introduced and tested.

The basic circuit layout of the LNA consists of the BGA420 amplifier integrated circuit with the surrounding network for phantom powering and to avoid overmodulation of its input. Special attention has been paid regarding the impedance match of the LNA. Furthermore, the amplifier has been fine-tuned for a nearly constant power gain.

Four different prototypes of LNAs have been introduced using similar circuit layouts. Two of them are designed to be mounted directly inside, the other two outside of the used antennas. Three of these prototypes have been built and tested extensively. The test routines include measurements of the s-parameters, stability, noise characteristics, 1 dB compression point, intermodulation behavior, two-channel crosstalk and power consumption.

One prototype fulfills all functional requirements for the application within AERA. The other two - designed to be mounted inside the antenna - show satisfying gain characteristics as well but produce too much noise and have an unsatisfying two-channel crosstalk due to their mechanical layout. Regarding the measurement results the fourth LNA, which was not yet tested, is expected to meet all functional requirements as well and will even show better characteristics of the gain and the crosstalk than the ones tested. Nevertheless, upcoming tests of this prototype are essential.

A protection against lightning for the amplifiers has been introduced which will be tested for full reliability in future studies. Furthermore, the temperature de-

pendency of the LNAs will be examined. This can also answer the question if the amplifiers might get destroyed due to the high thermal fluctuations at the AERA site which occur which the day and night cycle.
Since intermodulation might become an issue to the receiving system, filters are currently designed to be mounted between the antenna and the LNA since most intermodulating frequencies at the Pierre Auger Observatory are expected from outside the 30 to 80 MHz band.

Regarding the circuit layout of the amplifier the use of a low-drop voltage regulator will be tested. It will protect the amplifier from peaks in the bias voltage. The power consumption of the LNA will be increased by the regulator by 5% to 10%.
Moreover, the possibility of an improved impedance match by using LC-ladder matching networks of higher order will be examined.

With a reliable low-noise-preamplifier a further important step is made to turn AERA into the forerunner of the third fully established detector-type for ultra-high-energy cosmic rays at the Pierre Auger Observatory.

A. Appendix

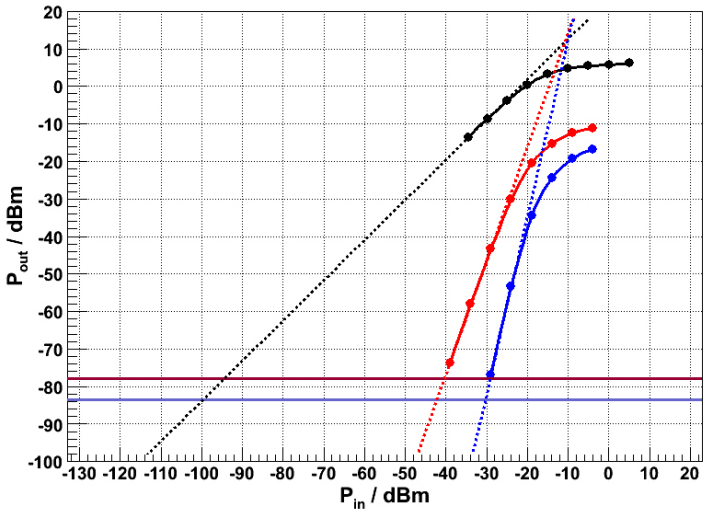

Figure A.1: Same as figure 7.10 but for 30 MHz.

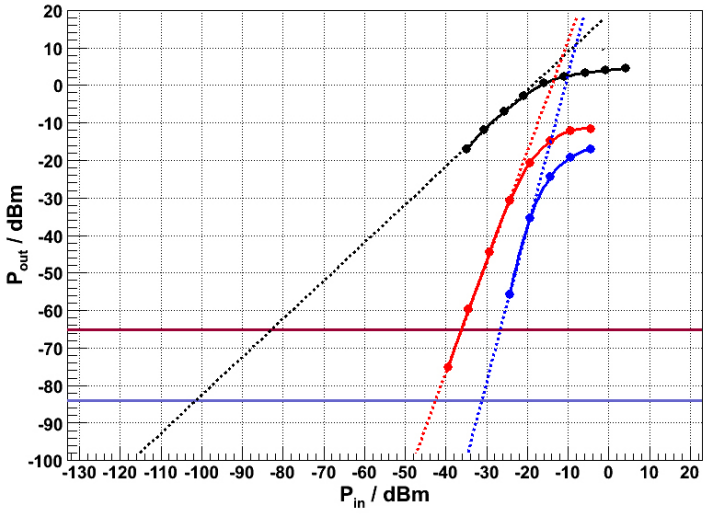

Figure A.2: Same as figure 7.10 but for 80 MHz.

Si-MMIC-Amplifier in SIEGET 25-Technologie

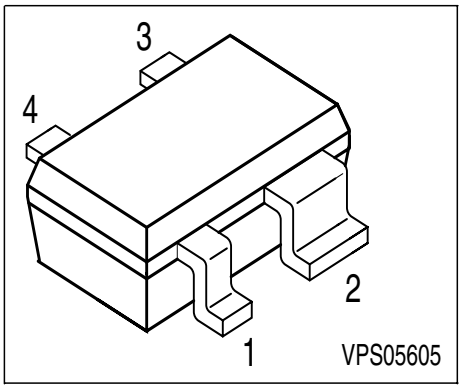

- Cascadable 50 Ω-gain block
- Unconditionally stable
- Gain $|S_{21}|^2$ = 13 dB at 1.8 GHz
  IP_{3out} = +13 dBm at 1.8 GHz
  (V_D = 3 V, I_D = typ. 6.7 mA)
- Noise figure *NF* = 2.3 dB at 1.8 GHz
- Reverse isolation > 28 dB and
  return loss *IN* / *OUT* > 12 dB at 1.8 GHz

Circuit Diagram

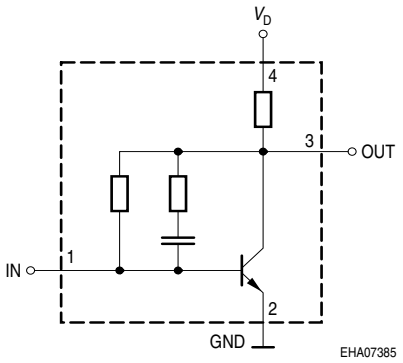

ESD: **E**lectro**s**tatic **d**ischarge sensitive device, observe handling precaution!

Type	Marking	Pin Configuration				Package
BGA420	BLs	1, IN	2, GND	3, OUT	4, VD	SOT343

Maximum Ratings

Parameter	Symbol	Value	Unit
Device current	I_D	15	mA
Device voltage	V_D	6	V
Total power dissipation T_S = 110 °C	P_{tot}	90	mW
RF input power	P_{RFin}	0	dBm
Junction temperature	T_j	150	°C
Ambient temperature	T_A	-65 ... 150	
Storage temperature	T_{stg}	-65 ... 150	

Thermal Resistance

Junction - soldering point[1)]	R_{thJS}	≤ 410	K/W

[1]For calculation of R_{thJA} please refer to Application Note Thermal Resistance

Electrical Characteristics at T_A = 25 °C, unless otherwise specified.

Parameter	Symbol	Values			Unit
		min.	typ.	max.	
AC characteristics V_D = 3 V, Z_o = 50 Ω					
Device current	I_D	5.4	6.7	8	mA
Insertion power gain	$\|S_{21}\|^2$				dB
f = 0.1 GHz		17	19	-	
f = 1 GHz		15	17	-	
f = 1.8 GHz		11	13	-	
Reverse isolation f = 1.8 GHz	S12	25	28	-	
Noise figure	NF				
f = 0.1 GHz		-	1.9	2.3	
f = 1 GHz		-	2.2	2.6	
f = 1.8 GHz		-	2.3	2.7	
Intercept point at the output f = 1 GHz	IP_{3out}	10	13	-	dBm
1dB compression point f = 1 GHz	P_{-1dB}	-6	-2.5	-	
Return loss input f = 1.8 GHz	RL_{in}	8	11	-	dB
Return loss output f = 1.8 GHz	RL_{out}	12	16	-	

Typical biasing configuration

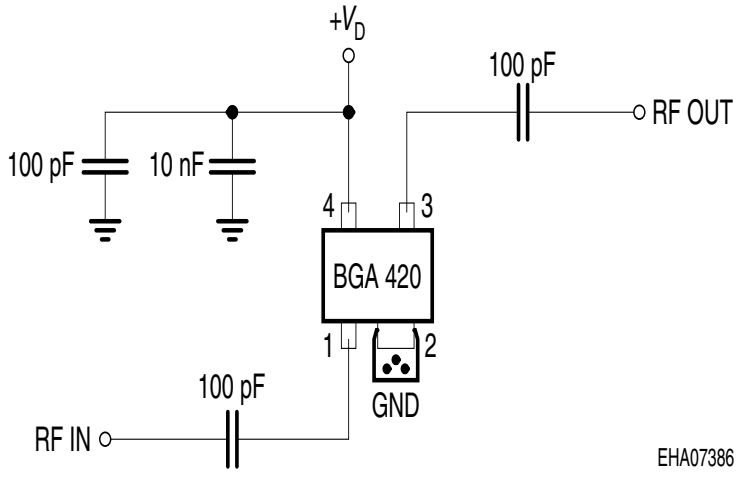

Note: 1) Large-value capacitors should be connected from pin 4 to ground right at the device to provide a low impedance path.

2) The use of plated through holes right at pin 2 is essential for pc-board-applications. Thin boards are recommended to minimize the parasitic inductance to ground.

Typical S-Parameters at T_A = 25 °C

f	S_{11}		S_{21}		S_{12}		S_{22}	
GHz	MAG	ANG	MAG	ANG	MAG	ANG	MAG	ANG
V_D = 3 V, Z_o = 50 Ω								
0.1	0.5686	-8.5	9.314	170.6	0.0268	12.7	0.2808	-8.6
0.5	0.5066	-19.2	8.393	149.4	0.0248	11.7	0.2613	-3.8
0.8	0.4404	-28.7	7.352	135.2	0.0236	25.6	0.2361	-6.7
1	0.3904	-34.6	6.69	126.8	0.024	35.9	0.2144	-9
1.5	0.2841	-50.5	5.244	111.1	0.0314	57.2	0.1398	-15
1.8	0.2343	-60.6	4.567	104	0.0378	63.5	0.0979	-18.2
1.9	0.2136	-64.1	4.355	102	0.0406	66.1	0.0838	-21.5
2	0.2062	-68.4	4.165	99.7	0.0426	67.2	0.0689	-22.2
2.4	0.1688	-89.7	3.417	91.7	0.0549	71.4	0.0224	-48
3	0.1558	-104.9	2.861	85.3	0.0682	73.1	0.0284	-147.5

Spice-model BGA 420

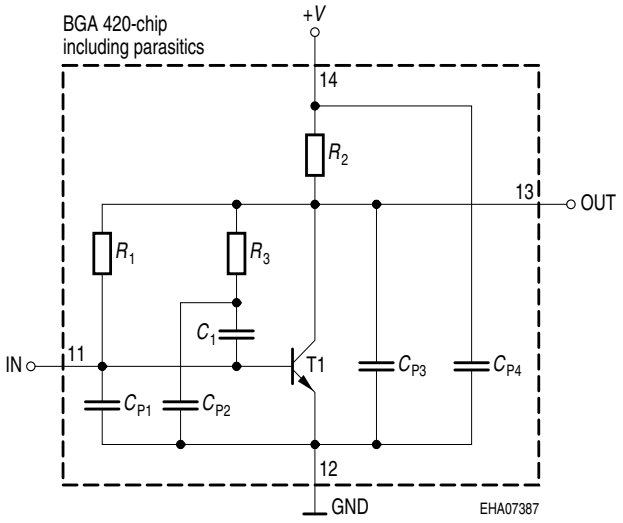

T1	T501
R_1	14.5kΩ
R_2	140Ω
R_3	2.4kΩ
C_1	2.3pF
C_{P1}	0.2pF
C_{P2}	0.2pF
C_{P3}	0.6pF
C_{P4}	0.1pF

Transistor Chip Data T1 (Berkley-SPICE 2G.6 Syntax) :

IS =	0.21024	fA	BF =	83.23	-	NF =	1.0405	-
VAF =	39.251	V	IKF =	0.16493	A	ISE =	15.761	fA
NE =	1.7763	-	BR =	10.526	-	NR =	0.96647	-
VAR =	34.368	V	IKR =	0.25052	A	ISC =	0.037223	fA
NC =	1.3152	-	RB =	15	Ω	IRB =	0.21215	A
RBM =	1.3491	Ω	RE =	1.9289		RC =	0.12691	Ω
CJE =	3.7265	fF	VJE =	0.70367	V	MJE =	0.37747	-
TF =	4.5899	ps	XTF =	0.3641	-	VTF =	0.19762	V
ITF =	1.3364	mA	PTF =	0	deg	CJC =	96.941	fF
VJC =	0.99532	V	MJC =	0.48652	-	XCJC =	0.08161	-
TR =	1.4935	ns	CJS =	0	fF	VJS =	0.75	V
MJS =	0	-	XTB =	0	-	EG =	1.11	eV
XTI =	3	-	FC =	0.99469	-	TNOM	300	K

C'-E'-Diode Data (Berkley-SPICE 2G.6 Syntax) :

IS =	2	fA	N =	1.02	-	RS =	20	Ω

All parameters are ready to use, no scaling is necessary

Package Equivalent Circuit:

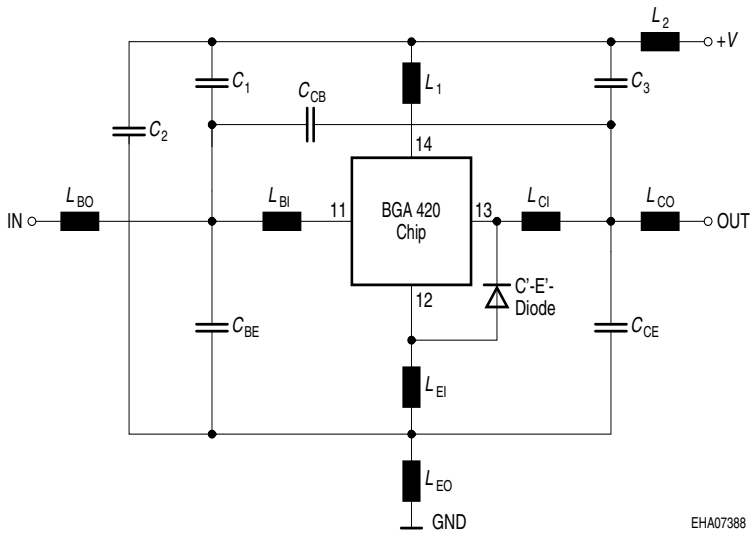

L_{BI} =	0.36	nH
L_{BO} =	0.4	nH
L_{EI} =	0.3	nH
L_{EO} =	0.15	nH
L_{CI} =	0.36	nH
L_{CO} =	0.4	nH
C_{BE} =	95	fF
C_{CB} =	6	fF
C_{CE} =	132	fF
C_1 =	28	fF
C_2 =	88	fF
C_3 =	8	fF
L_1 =	0.6	nH
L_2 =	0.4	nH

Valid up to 3GHz

Extracted on behalf of Infineon Technologies AG by:
Institut für Mobil-und Satellitentechnik (IMST)

For examples and ready to use parameters please contact your local Infineon Technologies distributor or sales office to obtain a Infineon Technologies CD-ROM or see Internet:
http://www.infineon.com/silicondiscretes

Insertion power gain $|S_{21}|^2 = f(f)$

V_D, I_D = parameter

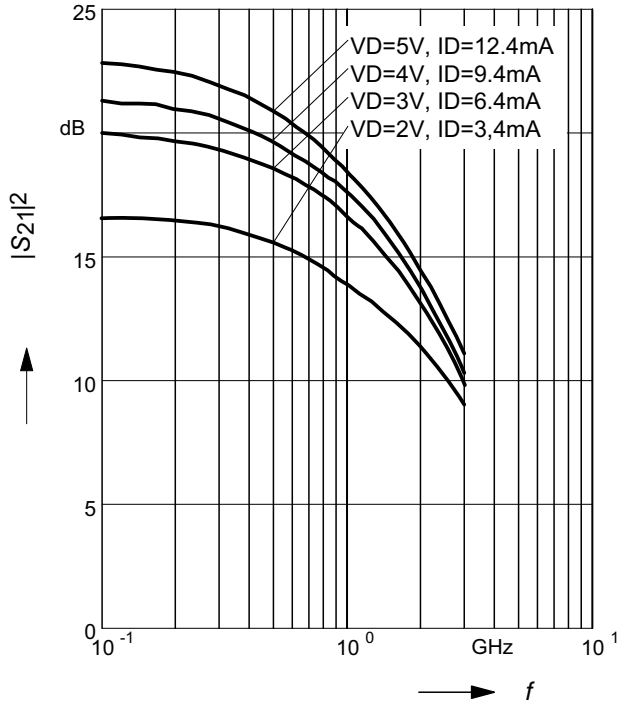

Insertion power gain $|S_{21}|^2 = f(f)$

V_D = 3 V

T_A = parameter

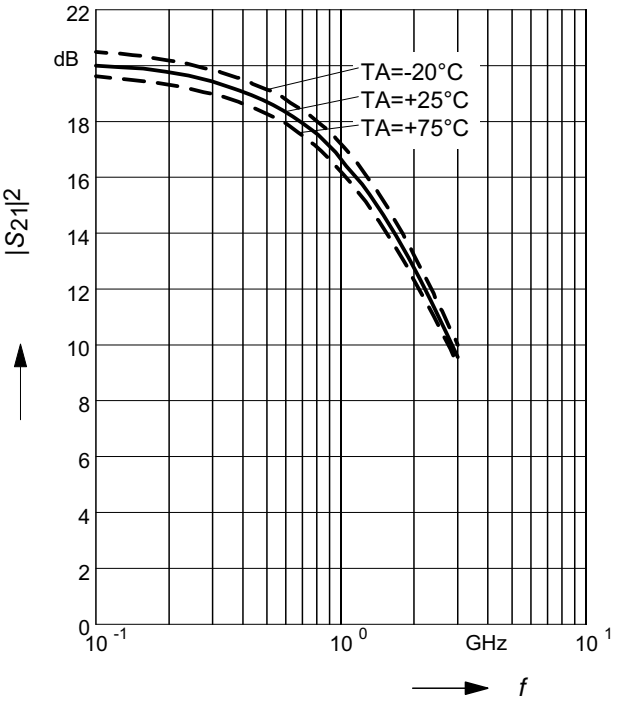

Noise figure $NF = f(f)$

V_D,I_D = parameter

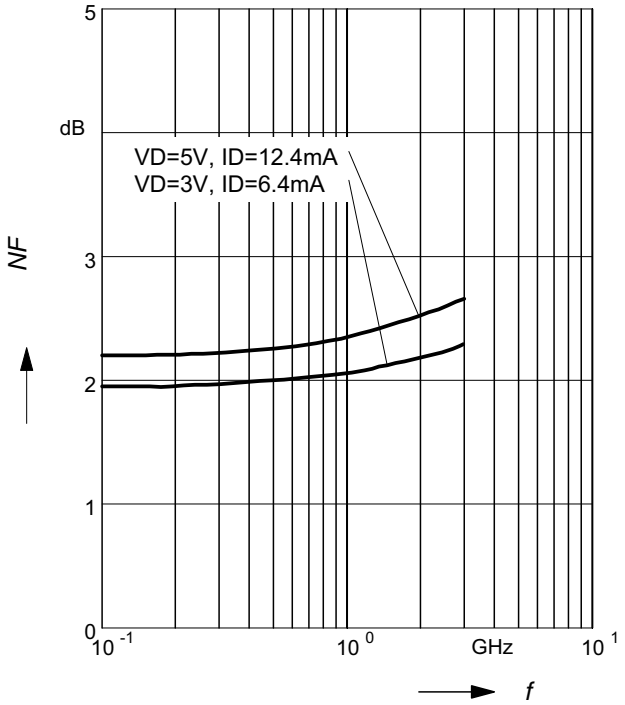

Noise figure $NF = f(f)$

V_D = 3V

T_A = parameter

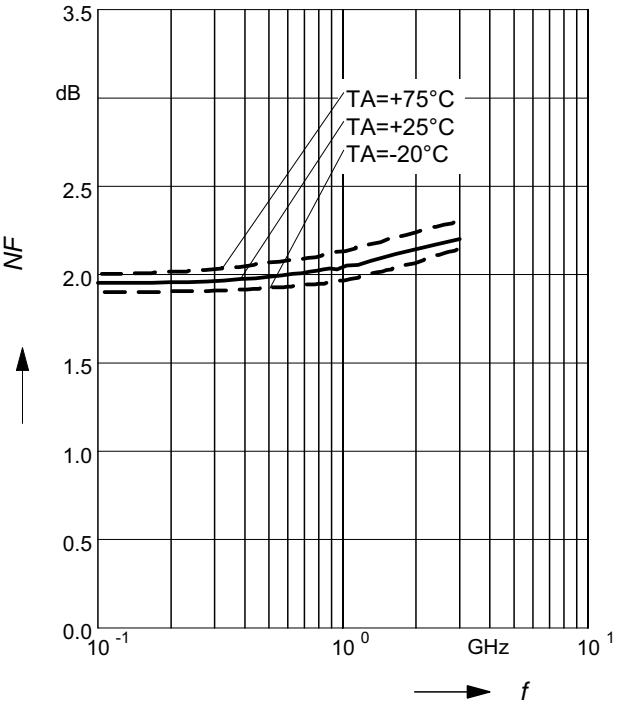

Intercept point at the output

$IP_{3out} = f(f)$

V_D, I_D = parameter

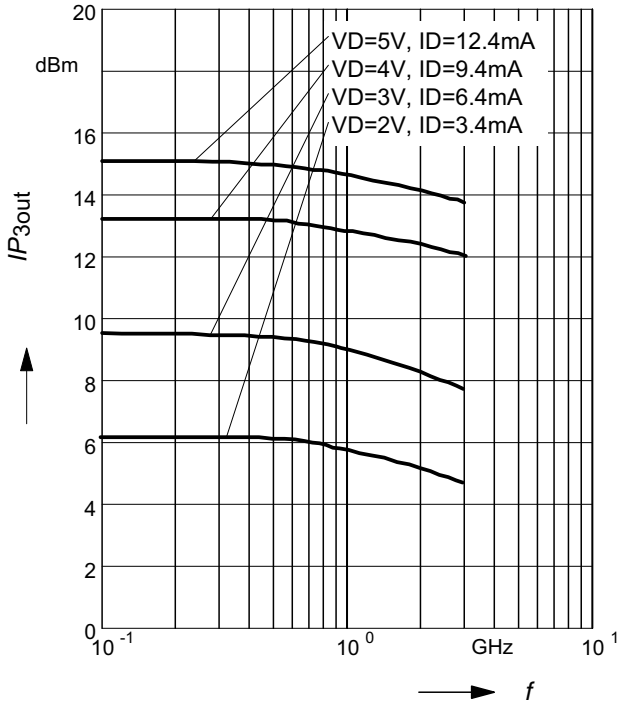

Intercept point at the output

$IP_{3out} = f(f)$, V_D = 3V

T_A = parameter

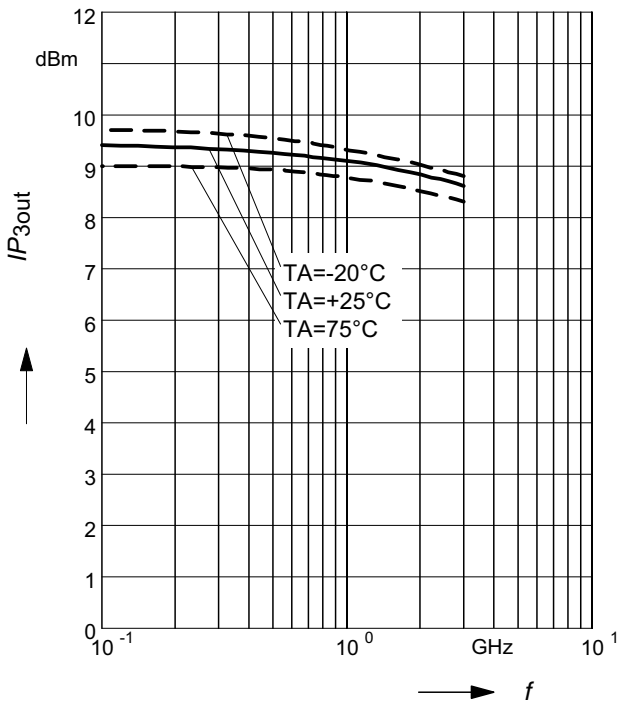

Danksagung - Acknowledgements

An dieser Stelle ist es mir eine große Freude mich bei den Menschen zu bedanken, ohne die die vorliegende Arbeit nicht bzw. so nicht möglich gewese wäre.

An erster Stelle danke ich meinem Betreuer Prof. Dr. Thomas Hebbeker, der mir diese spannende und vielseitige Arbeit überhaupt erst ermöglicht hat. Er hat meine Forschung und meinen Werdegang stets mit Interesse und wertvollen Beiträgen begleitet.
Darüberhinaus gilt Prof. Dr. Martin Erdmann großer Dank, der sich als Zweitgutachter bereitgestellt hat. Beide haben mir die Möglichkeit gegeben, wertvolle Einblicke in die Welt der Forschung zu erlangen, mir früh verantwortungsvolle Aufgaben anvertraut und somit meine Kompetenzen wesentlich geschult. Für die Gelegenheit, das Collaboration Meeting besuchen zu dürfen und in Argentinien Messungen durchführen zu können, möchte ich mich ganz besonders bedanken.

Außerordentlicher Dank gebührt auch dem Rest der Aachener Auger Gruppe: Hans Dembinski, Stefan Fliescher, Marius Grigat, Lars Mohrmann, Anna Nelles, Nils Scharf, Peter Schiffer, Sarah Schmetkamp, Stefan Schulte, Klaus Weidenhaupt und Tobias Winchen. Alle hatten stets ein offenes Ohr für meine Fragen und haben mich mit nützlichem Wissen und wertvollen Ideen versorgt. Besonders viele dieser Fragen mussten wohl Hans und Nils in der Zeit ertragen, als wir uns ein Büro teilten. Dank ihrer Engelsgeduld mit mir ist das ein oder andere Problem sehr viel schneller gelöst worden. Stefan und Tobias danke ich für das Korrekturlesen dieser Arbeit, Sarah und Marius für stilistische und andere Eingebungen. Allen danke ich für die produktive und entspannte Arbeitsatmosphäre innerhalb der Gruppe.

Die Mitarbeiter unserer elektronischen Werkstatt haben sich stets für meine technischen Probleme und Fragen interessiert und sich mit diesen auseinandergesetzt. In diesem Sinne gilt Günter Hilgers, Franz Adamczyk, Achim Paulus und Michael Brunzel großer Dank. Ganz besonders möchte ich mich bei Günter Hilgers bedanken. Sein Engagement für meine Arbeit war beispiellos. Durch seinen Ideenreichtum und seinen unsäglichen Erfahrungsschatz war er eine besondere Bereicherung für meine Forschung. Ohne seine Mithilfe wäre meine Arbeit in dieser Form undenkbar gewesen. Er hat das Layout der Verstärker entscheidend beeinflusst.

Insbesondere möchte ich mich auch bei Matthias Leuthold bedanken. Sein Enthusiasmus hat maßgeblich zur Wahl meines Diplomarbeitsthemas beigetragen.
Holger Erkens und Markus Robens danke ich für die Möglichkeit der Messung des Verstärkerrauschens und die Mithilfe bei dieser. Hans Reithler gilt Dank für die Bereitstellung der Daten bezüglich der Funkenstrecke, Barthel Phillips für die tech-

nischen Zeichnungen, die ich für meine Präsentationen nutzen durfte. Er hat auch das in der vorliegenden Arbeit gezeigte CAD Design der Black Spider Antenne entworfen.
Tobias Rademacher und Laurens Busch gegenüber möchte ich meinen speziellen Dank zum Ausdruck bringen für die langen und ausführlichen Gespräche und Diskussionen, obwohl die beiden schon Feierabend hatten.

Auf das Herzlichste bedanke ich mich nochmals bei Klaus Weidenhaupt. Ohne ihn wäre ich wohl nie an dem Punkt angekommen, an dem ich mich heute befinde. Dieser Dank gebührt für die unzähligen fruchtbaren Diskussionen in den Jahren vor wie während dieser Arbeit, sowie für die Hilfe bei der Durchführung diverser Messungen. Auch - und nicht zuletzt - bedanke ich mich für die langjährige und besondere Freundschaft. Die gemeinsamen Messreihen in der argentinischen Pampa gehören wohl zu den unvergesslichsten Ereignissen meines Studiums. Dieses selbst und die Welt um das Studium herum sind durch Klaus in einer unersätzlichen Form für mich bereichert worden.

Ganz besonders von Herzen danke ich auch meinen Elern, ohne die ich nicht auf diese Art und Weise hätte studieren können, sowie meiner Oma, meinem Herrn Großvater und meinem Bruder. Meine Familie hat mir weit über diese Arbeit hinaus immer einen sicheren Rückhalt geboten, indem sie vor allem jederzeit an mich geglaubt hat.

Meiner Freundin Anja gilt derartig großer Dank, dass er sich nicht von mir in Worten fassen lässt. Unter anderem hielt sie mir den Rücken frei, als private Umstände die rechtzeitige Abgabe dieser Arbeit gefährdeten, und war die Quelle meiner Ruhe und Kraft, wenn ich sie brauchte. Auch brachte sie stets Verständnis auf, wenn es ”mal wieder etwas später” wurde, oder ich es nicht sein lassen konnte von meinen Ideen und Messergebnissen zu reden.

Danken möchte ich auch Yvonne, Leo, Tobias und Georgios, die keine meiner Bitten abgelehnt haben, um das Schreiben dieser Arbeit zeitlich zu ermöglichen, und mit angepackt haben, als es nötig wurde.

References

[1] V. F. Hess. Über Beobachtungen der durchdringenden Strahlung bei sieben Freiballonfahrten. *Phys. Zeit.*, 13(1084), 1912.

[2] T. Huege. Radio Emission from Cosmic Ray Air Showers. *PhD dissertation accepted by the Mathematisch-Naturwissenschaftliche Fakultät der Rheinischen Friedrich-Wilhelms-Universität Bonn.* 2004.

[3] J. W. Cronin, T. K. Gaisser and S. P. Swordy. Cosmic rays at the energy frontier. *Scientific American*, 276:44–49, 1997.

[4] J. Blümer, R. Engel and J. R. Hörandel. Cosmic Rays from the Knee to the Highest Energies. *arXiv:0904.0725v1 [astro-ph.HE]*, 2009.

[5] A. Haungs. Energy Spectrum and Mass Composition around the Knee by EAS Measurements. *J. Phys.*, G29:809–820, 2003. arXiv:astro-ph/0212481v1.

[6] K.-H. Kampert *et al.* Cosmic Ray Energy Spectra and Mass Composition at the Knee - Recent Results from KASCADE -. *arXiv:astro-ph/0410559v1*, 2004.

[7] E. Fermi. On the Origin of the Cosmic Radiation. *Phys. Rev.*, 75(8):1179–1174, 1949.

[8] A. M. Hillas. The origin of ultra-high-energy cosmic rays. *Ann. Rev. Astron. Astrophys.*, 22(1):425–444, 1984.

[9] J. W. Cronin. The highest-energy cosmic rays. *Nuclear Physics B*, 138:465–491, 2005.

[10] A. A. Penzias and R. W. Wilson. A measurement of excess antenna temperature at 4080 mc/s. *Astrophysical Journal*, 142:419–421, 1965.

[11] K. Greisen. End to the Cosmic-Ray Spectrum? *Phys. Rev. Lett.*, 16(17):748–750, 1966.

[12] G. T. Zatsepin and V. A. Kuzmin. Upper Limit of the Spectrum of Cosmic Rays. *JETP Lett.*, 4:78–80, 1966.

[13] M. Nagano and A. A. Watson. Observations and implications of the ultrahigh-energy cosmic rays. *Rev. Mod. Phys.*, 72(3):689–732, 2000.

[14] T. Yamamoto for the Pierre Auger Collaboration. The UHECR spectrum measured at the Pierre Auger Observatory and its astrophysical implications. In *Proc. of 30th Int. Cosmic Ray Conf.*, Mérida, México, 2007. arXiv:0707.2638v1 [astroph].

[15] K. Dolag, D. Grasso, V. Springel and I. Tkachev. Constrained Simulations of the Magnetic Field in the Local Universe and the Propagation of UHECRs. *arXiv:astro-ph/0410419v2*, 2005.

[16] The Pierre Auger Collaboration. Correlation of the Highest-Energy Cosmic Rays with Nearby Extragalactic Objects. *Science*, 318:938–943, 2007. arXiv:0712.2843v2 [astro-ph].

[17] P. Auger, P. Ehrenfest, R. Maze, J. Daudin and Robley A. Fréon. Extensive cosmic-ray showers. *Rev. Mod. Phys.*, 11(3-4):288–291, 1939.

[18] P. Billoir. Phenomenology of Ultra-High-Energy Atmospheric Showers. In M. Lemoine and G. Sigl (Ed.) *Physics and Astrophysics of Ultra-High-Energy-Cosmic Rays*, (Berlin-Heidelberg-New York: Springer), 27-44, 2001.

[19] F. Schmidt. CORSIKA Shower Images. *http://www.ast.leeds.ac.uk/~fs/showerimages.html*.

[20] D. Heck, J. Knapp, J. N. Capdevielle, G. Schatz and T. Thouw. CORSIKA: A Monte Carlo Code to Simulate Extensive Air Showers. *Wissenschaftliche Berichte, Forschungszentrum Karlsruhe*, FZKA 6090, 1998.

[21] J. Matthews. A Heitler model of extensive air showers. *Astropart. Phys.*, 22(5-6):387–397, 2005.

[22] T. K. Gaisser and A. M. Hillas. Reliability of the method of constant intensity cuts for reconstructing the average development of vertical showers. In *Proc. of 15th International Cosmic Ray Conference*, Plovdiv, Bulgaria, 1977.

[23] The LOPES Collaboration. Progress in air shower radio measurements: Detection of distant events. *Astropart. Phys.*, 26:332–340, 2006.

[24] J. V. Jelley, J. H. Fruin, N. A. Porter, T. C. Weekes, F. G. Smith, and R. A. Porter. Radio pulses from extensive cosmic-ray air showers. *Nature*, 205:327, 1965.

[25] G. A. Askaryan. Excess negative charge of an electron-photon shower and its coherent radio emission. *Soviet Phys. JETP Lett.*, 14(441), 1962.

[26] F. D. Kahn and I. Lerche. Radiation from cosmic ray air showers. In *Proceedings of the Royal Society of London*, 289:206-213, 1966.

[27] H. Falcke and P. Gorham. Detecting radio emission from cosmic ray air showers and neutrinos with a digital radio telescope. *Astropart. Phys.*, 19(477), 2003.

[28] H. R. Allan. In J. G. Wilson and S. A. Wouthuysen (Ed.) *Progress in Elementary Particle and Cosmic Ray Physics* (North Holland Pub. Co.), Vol. 10, 171, 1971.

[29] H. R. Allan, R. W. Clay and J. K. Jones. Radio pulses from extensive air showers. *Nature*, 227(5263):1116–1118, 1970.

[30] J. D. Jackson. *Classical Electrodynamics* (John Wiley & Sons Inc.), Vol. 2., 1975.

[31] T. Huege, R. Ulrich and R. Engel. Monte carlo simulations of geosynchrotron radio emission from corsika-simulated air showers. *Astropart. Phys.*, (27):392–405, 2007.

[32] T. Huege and H. Falcke. Radio emission from cosmic ray air showers: simulation results and parametrization. *Astropart. Phys.*, 24:116–136, 2005.

[33] O. Scholten, K. Werner and F. Rusydi. A macroscopic description of coherent geo-magnetic radiation from cosmic ray air showers. *Astropart. Phys.*, 29:94–103, 2008. arXiv:0709.2872v1 [astro-ph].

[34] A. v.d. Berg *et al.*. AERA proposal for the construction of the 20 km^2 Auger Engineering Radio Array at the Southern Auger Observatory, 2009.

[35] T. Huege, R. Ulrich and R. Engel. Dependence of geosynchrotron radio emission on the energy and depth of maximum of cosmic ray showers. *Astropart. Phys.*, 30:96–104, 2008.

[36] The CODALEMA Collaboration. Geomagnetic origin of the radio emission from cosmic ray induced air showers observed by codalema. *Astropart. Phys.*, 31(3):192–200, 2009.

[37] B. Revenu for the CODALEMA and Auger Collaborations. Geomagnetic features of the events observed by the self triggered, fully autonomous radiodetector system installed at the clf. *GAP note*, 2009–5, 2009.

[38] Image gallery at http://www.auger.org.

[39] The Auger Collaboration. *Technical Design Report*, 2004.

[40] D. Allard *et al.* for the Pierre Auger Collaboration. The trigger system of the Pierre Auger Surface Detector: operation, efficiency and stability. In *Proc. of 29th Int. Cosmic Ray Conf.*, Pune, India, 2005. arXiv:astro-ph/0510320v1.

[41] M. Grigat. *Private communication*, 2009.

[42] J. R. Hörandel. Configurations for a Radio Antenna Array at the Pierre Auger Observatory. *GAP-note*, 2009–034, 2009.

[43] Image gallery at http://www.augerradio.org.

[44] K. Weidenhaupt. LPDA-Antennas for Large Scale Radio Detection of Cosmic Rays at the Pierre Auger Observatory. *Diplomathesis accepted by the the Fakultät für Mathematik, Informatik und Naturwissenschaften der Rheinisch Westfälischen Technischen Hochschule Aachen.* 2009.

[45] S. Fliescher. Radio Detection and Detector Simulation for Extensive Air Showers at the Pierre Auger Observatory. *Diplomathesis accepted by the Fakultät für Mathematik, Informatik und Naturwissenschaften der Rheinisch Westfälischen Technischen Hochschule Aachen*. 2008.

[46] S. Fliescher for the Pierre Auger Collaboration. Radio Detector Array Simulation - A Full Simulation Chain for an Array of Antenna Detectors. In *Proc. of 3rd Int. Workshop on Acoustic and Radio EeV Neutrino detection Activities: ARENA 2008*, Rome, Italy, 2008. arXiv:0811.1893v1 [astro-ph].

[47] H. O. Klages for the Pierre Auger Collaboration. HEAT – Enhancement Telescopes for the Pierre Auger Southern Observatory. In *Proc. of 30th Int. Cosmic Ray Conf.*, Mérida, México, 2007.

[48] A. Etchegoyen for the Pierre Auger Collaboration. AMIGA, Auger Muons and Infill for the Ground Array. In *Proc. of 30th Int. Cosmic Ray Conf.*, Mérida, México, 2007.

[49] E. Hering, K. Bressler and J. Gutekunst. Elektronik für Ingenieure und Naturwissenschaftler (5^{th} Ed.), (Berlin-Heidelberg-New York: Springer), 2005.

[50] J. Detlefsen and U. Siart. Grundlagen der Hochfrequenztechnik (2^{nd} Ed.), (München-Wien: Oldenbourg), 2006.

[51] International Telecommunication Union - Radio Sector. *Recommendation ITU-R P.372-9. Radio Noise*, 2007.

[52] O. Krömer. Empfangssystem zur Radioobservation hochenergetischer kosmischer Schauer und sein Verhalten bei Selbsttriggerung. *PhD dissertation accepted by the Fakultät für Elektrotechnik und Informationstechnik der Universität Karlsruhe*. 2008.

[53] K. Lange, K.-H. Löcherer, *Meinke · Gundlach Taschenbuch der Hochfrequenztechnik*, 5. überarb. Auflage, Springer-Verlag Berlin u.a., ISBN 3-540-54714-2 (1992) as cited in [52].

[54] H. Erkens and M. Robens. *Private Communication.* 2009.

[55] Agilent Technologies, Inc. *Fundamentals of RF and Microwave Noise Figure Measurements.* Application Note 57-1. 2006.

[56] G. Hilgers. *Private Communication.* 2009.

Erklärung

Hiermit versichere ich, dass ich diese Arbeit einschließlich evtl. beigefügter Zeichnungen, Kartenskizzen u.ä.m selbstständig angefertigt und keine anderen als die angegebenen Hilfsmittel und Quellen benutzt habe. Alle Stellen, die dem Wortlaut oder dem Sinn nach anderen Werken entnommen sind, habe ich in jedem einzelnen Fall unter genauer Angabe der Quelle deutlich als Entlehnung kenntlich gemacht.

Aachen, den 27. April 2010

_____

Eugène Antoine Maurice Stephan